Chapter 2

Mussel Inspired Polydopamine Nanocomposite as Bioactive Antioxidant for the Management of Oxidative Stress and Neurogenesis in Traumatic Brain Injury

2.1 ABSTRACT

In the intricate landscape of Traumatic Brain Injury (TBI), the management of TBI remains a challenging task due to the highly complex pathophysiological conditions, excessive release of reactive oxygen species (ROS) at the injury site and the limited regenerative capacities of the central nervous system (CNS). Existing pharmaceutical interventions are limited in their ability to efficiently cross the blood-brain barrier (BBB) and expeditiously target areas of brain inflammation. In response to these challenges herein, we designed novel mussel-inspired polydopamine (PDA)-coated mesoporous silica nanoparticles (PDA-AMSNs) with excellent antioxidative ability to deliver a new potential therapeutic GSK-3β inhibitor lead small molecule abbreviated as Neuro Chemical Modulator (NCM) at the TBI site using a neuroprotective peptide hydrogel (PANAP). PDA-AMSNs loaded with NCM (i.e., PDA-AMSN-D) into the matrix of PANAP were injected into the damaged area in an in vivo cryogenic brain injury model (CBI). This approach is built explicitly while keeping the logic AND gate circuit as the primary focus. NCM and PDA-AMSNs act as two input signals, and neurological functional recovery is a single output. Therapeutically, PDA-AMSN-D significantly decreased infarct volume, enhanced neurogenesis, rejuvenated BBB senescence, and accelerated neurological function recovery in a CBI.

2.2 INTRODUCTION

Treatment of Traumatic brain injury (TBI) is a challenging task due to its multifaceted, complex condition that causes significant global mortality annually.[1] It is worth mentioning that TBI itself counts for the highest incidences among all common neurological disorders.[2] Every year, an astonishing almost 50 million individuals suffer the deleterious consequences of TBI.[2] The substantial costs associated with the clinical treatment of TBI and the resulting socio-economic challenges have imposed a humongous burden on the healthcare system, family and at large to the society. The complex pathophysiology of TBI can be categorized into two distinct features: primary injury and secondary injury; primary damage is followed by extended secondary damage, which encompasses several factors, namely the disruption of the blood-brain barrier (BBB), glutamate excitotoxicity, oxidative stress, overproduction of reactive oxygen species (ROS), reactive nitrogen species (RNS), reactive gliosis and the activation of neuroinflammation.[3] This, in turn, triggers subsequent processes that ultimately result in a persistent neurological disorder, including activation of microglia and astrocytes at the lesion site[4], hindering the integration and generation

of new neurons, preventing tissue and axonal development.[5] In this sequence of events, primary injury can only be avoided; however, secondary injury presents a potential avenue for therapeutic intervention to preserve brain tissue. Unfortunately, despite an extensive array of clinical trials, no available therapeutic have shown efficacy in improving the pathophysiology of TBI.[6] Hence, there is an urgent need for the development of potential therapeutics which can target secondary injury-related pathophysiology in TBI.

However, in recent years, transplantation of induced pluripotent stem cells (PSCs)[7], mesenchymal stem cells (MSCs)[8,9], and neural stem cells (NSCs)[10] have emerged as potent and promising therapeutic approaches in the domain of regenerative medicine. However, challenges such as low cell viability, immunological rejection, and the inability to precisely quantify cell viability could impact the accurate evaluation of the usefulness of cell transplantation in accomplishing long-term healing and restoring neurological function. Gene therapy and drug delivery, on the other hand, also provide promising alternatives to stem cell transplantation.[11] However, they quickly degrade in the blood or by cells and have restricted cellular uptake. More importantly, BBB serves as a formidable barricade, impeding the access of most drugs from the bloodstream to the brain. Moreover, retention and functional preservation of any therapeutic lead (growth factors, drugs) in the lesion site are far from satisfactory and hamper the brain's functional recovery.[12] As a result, intensive and advance investigation for the development of a novel drug delivery platform that can both load drug and potential therapeutic leads into cells and cross the BBB is of utmost current need.

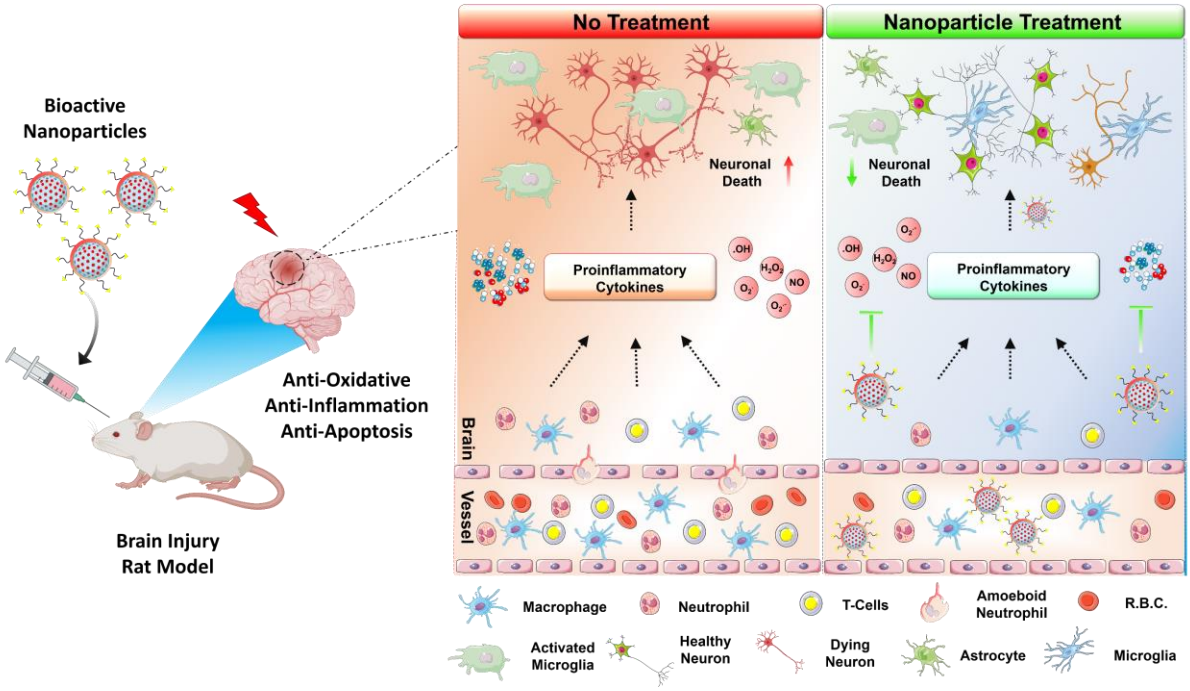


Figure 2.1 Schematic illustration of the PDA-AMSN-D in brain injury

Towards this venture nanomedicine-based approach has recently received a wider interest as a potential solution for this challenging task. One of the platform based on mesoporous silica nanoparticles (MSNs) have been attempted as a drug delivery agent

because of their ultrahigh specific surface area, tunable pore size, adjustable size, easiness for surface modification and excellent biocompatibility.[13] In addition to the passive targeting mechanism facilitated by the enhanced permeability and retention effect, MSNs can be strategically designed to provide selective delivery of diverse therapeutic agents to neuronal cells.[14,15] This can be achieved by including active targeting ligands, like peptides, small molecules, antibodies, or aptamers.

In this chapter, we have demonstrated the development of an advanced Mussels (Mytilus edulis) mimetic bio-engineered materials for the management of neurogenesis in TBI condition (**Figure 2.1**). The rationale behind our design and choosing Mussels is due to its ability to adhere to a wide range of inorganic and organic surfaces. The amino acid composition of their adhesive foot protein Mefp-5 may provide clues to the incredible adhesive flexibility of mussels[16]. These proteins (Mefp-5) are rich with 3,4-dihydroxy-l-phenylalanine (DOPA) and lysine amino acids and can bind with surfaces of many materials, including noble metals, metal oxides, semiconductors, ceramics, and synthetic polymers.[17] Polydopamine (PDA) is a synthetic material that mimics the properties of melanin. It is formed through the polymerization of 3,4-dihydroxyphenylalanine (DOPA), the primary component of adhesive foot protein Mefp-5 , responsible for a wide range of adhesiveness. However, it is important to mention that the PDA coating exhibits remarkable biocompatibility, antioxidant nature and minimal cytotoxicity, rendering it a versatile substrate for the development of many advance biomaterials.[18] Furthermore, previous studies have documented that incorporating enzymes and drugs into PDA-silica hybrid materials has been shown to improve both the stability and loading capacity.[19]

Taking together, we showcased here the development of a large pore size MSNs (L-MSN) loaded with a potential therapeutic payload (NCM) and surface coated with PDA to mimic the natural double layer structure of mussel (Calcium Shell layer/ DOPA layer) by self-polymerization of Dopamine under alkaline conditions. The designed PDA-AMSN has an exceptionally well drug loading capacity of 71%. Our imidazole-based therapeutic payload (NCM) acts as a GSK-3β inhibitor28 and has been chosen to act as a therapeutic target for the differentiation of stem cells to neurons at the injury site. At the same time, PDA coating on the MSNs could provide an antioxidative nature to the NPs against highly oxidative ROS and RNS in the oxidative microenvironment. When it comes to developing a therapeutic for TBI, it is well-known that creating a proper neural scaffold would be a crucial technique in favour of the local administration of any therapeutic to the target lesion site. The ideal biomaterials to be used as a scaffold for the transplantation should be strong enough to protect brain tissue but also stretchable and elastic enough to conform to variations in intracranial pressure. In view of the above-mentioned points, we have developed an excellent neuroprotective hydrogel (PANAP) to act as a scaffold for delivering bioactive antioxidant neuroprotective PDA-AMSNs for functional recovery in TBI. The designed hydrogel is derived from an activity-dependent neuroprotective peptide (ADNP) called as NAP, which is composed of an eight amino acid long chain of sequence NAPVSIPQ[20]. The rationale behind choosing this snippet from ADNP is because of its widely known function, ranging from stabilizing microtubules to providing neuroprotection in severe neurodegenerative diseases. Moreover, since the

amphiphilic nature of any molecule is well known to cause self-assembly, hence we have incorporated the peptide hydrogel with a long hydrophobic chain of palmitic acid (PA) at the N-terminal of the octa peptide, followed by an octa-peptide designated as NAP, and a triple hydrophilic amino acid (Lys/K) to increase the self-assembly hence the gelation of the hydrogel. Overall, the above-mentioned combination resulted in a hydrogel which is palmitic acid (PA)-attached to an octapeptide with triple lysine, NAPVSIPQKKK. Hence, this hydrogel is abbreviated as PANAP. Owing to its amphiphilic nature, this hydrogel spontaneously self-assembles into a β-sheet structure, which leads to the formation of a complex network structure composed of interconnected fibres, which effectively traps a significant amount of water molecules and results in the creation of a clearly defined hydrogel. The dense fibrillary network of this hydrogel mimics the extracellular matrix of the cells and acts as an ideal scaffold for the delivery of any bioactive agent[21,22].

The cellulo-toxic assay showed excellent biocompatibility of PDA-AMSNs with neuroblastoma cell line (SH-SY5Y) and elegant cell lines like umbilical cord-derived human mesenchymal stem cells (hMSCs). Further, a cryogenic injury model (CBI) was used to induce a moderate TBI, that exhibited physical vascular disruption and tissue deformation. We, therefore, applied the Gel (PANAP) / PDA-AMSN-D system to the injury site immediately after CBI. It was observed that in our postoperative CBI models Gel / PDA-AMSN-D system could reduce neuroinflammation, bestow BBB protection, confer neuroprotective effect, and promote neuron regeneration and functional recovery (Scheme 2). The unique amalgation of Gel / PDA-AMSN-D system acts as an AND logic gate where both NCM and PDA-AMSNs mitigate injury outcomes and contribute to the neurological functional recovery (Scheme 3, Table 1).

Neurogenesis (NCM)	Neuroprotection (PDA)	Functional Recovery
0	**0**	**0**
0	**1**	**0**
1	**0**	**0**
1	**1**	**1**

Table 2.1: Tabular representation of AND logic gate responses for total functional recovery

The "AND Gate Circuit" in synthetic biology is an approach that involves two input signals and activates the output signal only when both input signals are activated simultaneously [23,24]. This concept shows promise as a tool for precisely controlling physiological and pathological processes in several species. This unique formulation of nanocomposite was designed according to the logic "AND gate circuit" strategy with NCM and PDA-AMSN as two input signals and functional recovery as an output signal. First, a novel our own lab-designed glycogen synthase kinase-3 (GSK-3β) inhibitor small molecule abbreviated as NCM and PDA-AMSNs was synthesized for the input signals. The NCM acts as a transdifferentiation inducer at the injury site, enhancing neurogenesis, and PDA-AMSN acts as a dual agent, Trojan horse for the

NCM and also as an antioxidant neuroprotective nanocomposite inhibiting the excessive ROS, neuroinflammation and ROS-mediated apoptosis of neurons, hence leading to a total functional recover.

Overall, our work, for the first time, demonstrated the use of bioactive PDA-coated mesoporous silicon for the delivery of therapeutic payload at the traumatic brain injury site, providing a promising therapeutic option for TBI therapy. These findings demonstrated that this innovative medication delivery system significantly reduced inflammation, enhanced neurogenesis and improved cognitive function in the TBI model, indicating its potential for further clinical applications and various other oxidative stress-related CNS injuries. Further studies are needed to optimize the dosage and evaluate the long-term efficacy and safety of this system coin treating TBI in clinical trials.

2.3 MATERIALS AND METHODS

2.3.1 Materials and Reagents: The 1H NMR and 13C NMR spectra were obtained using a Bruker Advance 500 MHz spectrometer at a temperature of 300 K, with tetramethylsilane (TMS) used as the internal standard. The mass spectra were obtained using an Agilent Technologies electrospray ionisation (ESI) Q-TOF mass spectrometer equipment (G6530C). The analysis using high-performance liquid chromatography (HPLC) involved the use of a Shimadzu C18 column with dimensions of 150 mm × 4.6 mm × 5 µm. Rink amide AM resin and Fmoc-protected amino acids were purchased from Novabiochem (Germany). ABTS, DPPH were purchased from Sigma, H_2O_2, DCFH-DA were purchased from Merck 3-(4,5-dimethylthiazol-2-yl)-2,5-diphenyl tetrazolium bromide (MTT) (M2128, Sigma), Fetal Bovine Serum (Invitrogen 2023-01-30), Antimycotic antibiotic solution (Himedia A002), Penicillin Streptomycin solution (Invitrogen 15140-122), Trypsin EDTA Solution (Sigma T4174), Bovin Serum Albumin (BSA) (83803, SRL), PVDF Membrane (Millipore), Immobilon Western HRP Substrate (Millipore WBLU F0500), Anti-Rabbit IgG HRP linked, (CST-7074, Dilution 1: 10k), HRP conjugated secondary Antibody (Anti-Mouse IgG HRP linked, CST 7076, Dilution 1: 5k), Mouse mAb IL-6 (Abcam, ab9324, Dilution 1: 1k), Rabbit mAb Anti-BCl-xl (Abcam, 32370, Dilution 1: 2k) Rabbit Anti-Bax (CST, 2772, Dilution 1: 1k), Rabbit mAb to Anti-Bad (Abcam, 32445) Rabbit mAb to GAPDH (CST, 2118), Goat Anti-Rabbit IgG HandL (Cy3.5 ®) preadsorbed (Abcam, ab6941), Goat anti-mouse IgG H and L Alexa Fluor® 488, (Thermo, A11029, Dilution 1:400), Hoecsht 33258 (ab228550, Abcam).

2.3.2 Synthesis of MSN: The small and large mesoporous silica nanoparticles (S-MSN and L-MSN) were meticulously synthesized using the well-established sol-gel technique, incorporating minor modifications as described previously.[25] To commence the procedure, 0.25g of CTAB (cetyltrimethylammonium bromide) was dissolved in 120 mL of distilled water, ensuring meticulous homogenization. Subsequently, a quantity of 0.875 mL of 2M NaOH was added into the solution, which was then subjected to vigorous agitation at a temperature of 95 °C for a duration of 1h. In this experimental phase, a volume of 1.5~2 mL of TEOS (tetraethyl orthosilicate)

was incrementally added drop by drop at a rate of 1 drop / minute. Subsequently, the resulting mixture was left undisturbed for an additional 1 h. After the reaction reached its peak, the solution was allowed to cool, and the resulting nanoparticles were collected by centrifugation at a speed of 12,000 rpm for a duration of 10 minutes. In order to eliminate any residual unreacted particles, obtained NPs were washed with ample amount of distilled water and ethanol. In order to eliminate the CTAB template, the as synthesized silica product (1 g) was subjected to a substantial amount of methanol in concentrated hydrochloric acid (HCl) and allowed to stir overnight. Subsequently, the nanoparticles were thoroughly rinsed using methanol and distilled water. The synthesis of NPs with larger pore sizes was conducted in accordance with a previously established protocol.[25] The procedure involved the addition of 600 µL of decane into the CTAB: NaOH mixture, while keeping the subsequent steps consistent with the initial protocol. The NPs obtained were appropriately labelled as L-MSN (containing decane) and S-MSN (without decane), respectively.

2.3.3 Drug Loading and Synthesis of Amine Modified MSN: Drug loading was performed accordingly to the previously reported protocol.[26] Typically, 50 mg of both S-MSN and L-MSN were added to the 5 mg of NCM and the mixture was stirred overnight at RT. Subsequently, the mixture was centrifuged at 10,000 rpm and the supernatant was collected and subjected to a UV-Vis spectrophotometer to quantify the amount of drug loaded into the NPs. Drug entrapment efficiency and drug loading efficiency was calculated as follows:

$$DL\ (\%) = \left\{\frac{Wt\ of\ drug\ in\ MSN}{Wt\ of\ Drug\ loaded\ MSN}\right\} X\ 100$$

$$DEE\ (\%) = \left\{\frac{Wt\ of\ drug\ in\ MSN}{Initial\ Wt\ of\ Drug\ taken}\right\} X\ 100$$

Amine functionalized MSNs were prepared as reported previously.[25] In a nutshell, a mixture of 100 mg of L-MSN and 100 mL of ethanol was prepared, followed by a refluxing mixture for a 4 h. Following the reflux process, 200 µL of APTES (3-aminopropyltriethoxysilane) was added to the mixture. Subsequently, the resulting solution underwent multiple thorough washes using water and ethanol. The amine-modified mesoporous silica nanoparticles (L-MSN) acquired through the described procedure were designated as AMSN.

As part of the process for preparing FITC-conjugated mesoporous silica nanoparticles (FMSN), an initial step was undertaken to synthesize FITC-conjugated APTES. The procedure involved amalgamation of 4 mg of FITC with 44 µL of APTES in 1 mL of ethanol. Subsequently, the mixture was subjected to an incubation for 12 h in dark, while being continuously stirred. Following this, the FITC-APTES solution was incorporated into the synthesis procedure immediately before the introduction of TEOS. The subsequent steps in the synthesis protocol of FMSN were consistent with the conventional procedure for synthesizing MSN as reported earlier.

2.3.4 Synthesis of PDA-Coated MSNs: PDA-coated MSN were synthesized via oxidative self-polymerization process under mildly alkaline conditions, specifically in a pH 8.5

solution containing 10 mM Tris-HCl buffer.[27] In this experiment, a quantity of 40 mg of AMSN-D and AMSN, was mixed with a 20 mL solution of dopamine at a concentration of 1 mg / mL. The resulting mixture was subjected to continuous stirring for overnight in the dark. Following this, the resulting product was washed using an ample amount of distilled water and was subsequently subjected to lyophilization. This procedure resulted in the production of the designated nanoparticles, which are referred to as PDA-AMSN-D and PDA-AMSN, respectively. This controlled synthesis process facilitated the formation of PDA coating on the surface of the MSN, providing an engineered and functionalized nanostructure with potential applications in neuroscience.

2.3.5 Characterization of MSNs: The examination of the morphology and shape of the various nanoparticles was conducted utilizing field emission scanning electron microscopy (FESEM). The determination of the specific surface areas and pore sizes of L-MSN and S-MSN was conducted using the Brunauer-Emmett-Teller (BET) method. This involved analyzing adsorption data within the relative pressure range of 0.05 to 0.2. In addition, the determination of pore size distribution was accomplished through the utilization of suitable nonlocal density functional theory (NLDFT) methodologies derived from the adsorption branch of isotherms. In order to examine the nanoparticle formation and changes in chemical bonding groups resulting from amine and PDA coating, Fourier-transform infrared spectroscopy (FT-IR) analysis was performed. The efficacy of amine functionalization and PDA coating on the MSN was also confirmed through thermogravimetric analysis (TGA) conducted over a temperature range of 200-800 °C with a heating rate of 10 °C/min.

2.3.6 Determination of Cytotoxicity: *In vitro* cytotoxicity of the Nanoparticles with both hMSCs and SH-SY5Y were evaluated using MTT assay, as described previously[28]. hMSCs and SH-SY5Y cells were cultured in 96 well plate at a density of 2 x 10^4 cells and 4 x 10^4 per well, respectively, for 24h. Further cells were treated with different concentrations of nanoparticles (7.8 µg / mL to 1 mg / mL) and different wt % of peptide hydrogel allowed to grow for an additional 24 hrs. After that MTT was added and the absorbance of the formazon salt was recorded at 570 nm in a thermo variolux scan microplate reader.

2.3.7 *In Vitro* Drug Release: For *in vitro* drug release studies, a slightly modified protocol was used.[29] First, 10 mg of PDA-AMSN-D was dissolved into 10 ml of PBS solution, and the mixture was kept at 37 °C allowed to stir at 100 rpm. At the predetermined time intervals, 1 mL of the solution was withdrawn from the reaction mixture and subjected to a UV-visible spectrophotometer. To keep the reaction volume constant equal volume of PBS was added each the sample were withdrawn. The amount of drug released into the solution was calculated by plotting a standard curve of drug concentration and absorbance.

2.3.8 DPPH Scavenging Test: DPPH is a well-known free radical cation to evaluate the antioxidative properties of any antioxidant material.[30] Briefly, 80 µg/mL concentration of DPPH reagent was made, to determine the scavenging ability of nanoparticles, 100 µL of the DPPH was incubated with a similar volume of sample (PDA-AMSN and AMSN) at different concentrations ranging from 5µg/mL to 200

μg/mL for 30 min in the dark. Ascorbic acid was used as a positive control. Then, the absorbance of the mixture was observed at 516 nm and the free radical scavenging rate was calculated as follows:

$$Radical\ Scavenging\ (\%) = \{(A)control - (A)sample\ /\ (A)control\}\ x\ 100$$

2.3.9 ABTS Free Radical Scavenging Test: The ABTS assay was performed with several modifications.[30] Briefly, 5 mL of 7 mM of ABTS reagent was prepared by mixing it with 88 μL of 140 mM potassium persulfate and then allowing it to generate free radicals for 12 hrs in the dark. The solution was diluted 1:40 (v/v) times before use. To determine the scavenging ability of nanoparticles 100 μL of ABTS reagent was mixed with 100 μL of the sample of different concentrations ranging from 5 μg/mL to 200 μg/mL for 30 min in the dark. Then, the absorbance was noted at 734 nm, and the free radical scavenging rate was calculated as follows:

$$Radical\ Scavenging\ (\%) = \{(A)control - (A)sample\ /\ (A)control\}\ x\ 100$$

***2.3.10 In Vitro* CCA Assay:** To evaluate the redox silencing activity of our nanoparticles CCA assay was performed according to our previously reported protocol.[31] Briefly, it includes incubation of non-fluorescent compound coumarin-3-carboxylic acid (CCA, 150 μM), Cu^{2+} (10 μM), and PDA-AMSN or ascorbic acid (10 μM) separately in PBS (0.1 mM, pH = 7.4) at 37 °C, further the fluorescent excitation and emission intensity was measured (λ_{ex} = 385 nm, λ_{em} = 452 nm) in the thermo varioluxscan microplate reader.

2.3.11 Assay of Catalase-like Activity: The CAT-like activity of PDA-AMSN-D was calculated by determining the inhibition of generation of a highly fluorescent compound 2-hydroxyterephthalic acid from its non-fluorescent form terepthalic acid (TA). In brief, TA would be oxidized in the presence of H_2O_2 and produce a highly fluorescent compound with an excitation of 320 nm and emission of 425 nm. The mixture containing PDA-AMS-D, TA (0.5 mM) and H_2O_2 (10 mM) was incubated at RT for 6 hrs. After completion of 6 h the fluorescent spectra of the mixture were measured.

2.3.12 Calcein-AM/PI Live Dead Assay for SHSY-5Y Cells: To determine the oxidative rescuing ability of PDA-AMSN, Calcein-AM and Propidium Iodide (PI) assay was used, Calcein-AM is a cell-permeable non-fluorescent compound, upon crossing the cell membrane it rapidly hydrolyzed by cellular esterase in live cells converting Calcein-AM to a strongly fluorescent green compound whereas Propidium Iodide (PI) is a red fluorescent nuclear and chromosome counterstain non-permeant to live cells. Briefly, first SH-SY5Y cells were cultured into 35 mm culture dish at a density of 3 x 10^5 cells/mL. Then, cells were treated with 500 μM of hydrogen peroxide (H_2O_2) for approx. 4h for ROS generation under serum free condition as ROS enriched condition. Further cells were treated with PDA-AMSN and AMSN. After treatment, cells were co-stained with calcein-AM (3 μM) and PI (3 μM) in phenol red-free colourless DMEM media for 15 minutes at 37 °C in the dark inside the CO_2 incubator. After that, media were removed and cells were washed with filtered PBS. The fluorescence images were captured immediately under a fluorescence microscope (OLYMPUS IX83), where red

fluorescence illustrates dead cells and green fluorescence signifies live cells. Further, the images were quantified by using Image J software.[32]

2.3.13 Calcein-AM/PI Live Dead Assay of hMSCs with PDA-AMSN: Briefly first hMSCs cells were cultured into 35 mm culture dish at a density of 2 x 10^5 cells/mL. and allowed to grow for 24 h. Further cells were treated with different concentrations of PDA-AMSN. After treatment, cells were co-stained with calcein-AM (3 μM) and PI (3 μM) in phenol red-free colourless DMEM media for 10 minutes at 37 °C in the dark inside the CO_2 incubator. After that, media were removed and cells were washed with filtered PBS. The fluorescence images were captured immediately under a fluorescence microscope (OLYMPUS IX83), where red fluorescence illustrates dead cells and green fluorescence signifies live cells. Further, the images were quantified by using Image J software.[32]

2.3.14 Hoechst Staining for Apoptosis: To measure the rescue effect of PDA-AMSN on apoptosis, we have cultured the pre-treated SH-SY5Y cells with PDA-AMSN and PANAP hydrogel. After 24h the cells were fixed and stained with Hoechst to check the nuclei morphology, images were captured at 60x in Olympus IX83 microscope.

2.3.15 Determination of Intracellular Basal ROS Level: Basal level of cellular ROS was determined by using a DCFH-DA probe.[33] The nonfluorescent probe DCFH-DA is used to monitor the amount of ROS found inside of cells. This probe is able to pass through the cell membrane into the cytoplasm, where it is then converted into DCFH by the intracellular esterase. Further, DCFH interacted with the free radicals found inside the cell to form the fluorescent product DCF, which had an excitation wavelength of 488 nm and an emission wavelength of 520 nm, respectively. SH-SY5Y were first cultured on a 35 mm ibidi culture dish at a density of 3 x 10^5 cells/mL and allowed to grow for 24 h. Following that cells were treated with 500 μM of H_2O_2 in serum-free condition for 4 h to produce ROS. After completion of 4 h the cells were treated with AMSN and PDA-AMSN for 24 h. Subsequently, cells were stained with 10 μM of DCFH-DA in phenol red-free media for 30 min. To determine concentration dependent effect of PDA-AMSN on overall cellular ROS production an additional group of cells without H_2O_2 enriched environment were also stained for DCFHDA. Images were acquired in the Olympus IX 83 microscope. To quantify the ROS level, cells were washed with PBS, lysed in alkaline solution (Triton X-100) and centrifuged at 2500g for 10 min. Further, the supernatant was transferred to a 96 well plate, and fluorescence was measured at 485 nm excitation and 525 nm emission using a thermo varioluxscan microplate reader. The fluorescence intensity values obtained from the various experimental wells were expressed as a percentage relative to the fluorescence intensity measured in the control wells.

2.3.16 Measurement of Cellular Oxidative Stress in Live Cells: To evaluate the ROS scavenging ability of nanoparticles in live cells, we used CellROX deep red reagent, which is a non-florescent in its reduced state and becomes fluorescent upon oxidation by ROS [34] and has an emission maximum at around 650 nm, we use H_2O_2 as a sourced for ROS generation. SH-SY5Y were first treated with 500 μM of H_2O_2 for 4 h under serum-free conditions were used as a ROS-enriched condition, cells cultured without H_2O_2 were used as a control. The cells with and without H_2O_2 treatment were further

grown in culture media with different nanoparticles (PDA-AMSN and AMSN). After 24 h the cells were washed with PBS and stained with 5 μM of Cell ROX deep red at 37 °C for 30 min in colourless DMEM media, after 30 min, cells were washed with PBS and image under a fluorescent microscope (IX83)[35]. For quantitative analysis, the images were analyzed for mean fluorescent intensity with the help of NIH Image J software.[32]

2.3.17 Assessment of CAT Mimetic Activity: Cells were treated with H_2O_2 and H_2O_2 + PDA-AMSN, following the completion of the treatment period cells were washed with chilled PBS and lysed with RIPA buffer, the cell lysate were collected and centrifuged at 12,000 rpm for 4 °C, following the completion of centrifugation the supernatant was collected for the CAT activity with the help of Cayman Chemical kit for CAT (Item No 707002) according to the manufacturer's instructions.

2.3.18 Measurement of Mitochondrial Superoxide ROS: Fluorescent detection of mitochondrial superoxide was measured using the mitochondria-specific fluorescent probe MitoSOX Red, Mito Tracker Green, which was used to confirm mitochondria location further DAPI stain was used to confirm the localization of the nucleus.[36] When oxidized by the superoxide anions, the mitosox red dye emits red fluorescent. First, cells were grown in H_2O_2 for the production of ROS and then treated with PDA-AMSN and AMSN for the ROS scavenging for an additional 24 h. Then, cells were so-stained with 5 μM of MitoSOX red and 200 nM mitotracker green for 15 min in dark in colourless DMEM at 37 °C. After incubation cells were counter-stained with DAPI and were visualized under Olympus IX83 fluorescent microscope. Image J software was used to quantify the MitoSOX intensity in each panel.

2.3.19 Measurement of Mitochondria Membrane Potential ($\Delta\Psi_M$): For the measurement of $\Delta\Psi_M$, double fluorescent staining of mitochondria by JC-1 dye was used.[37] First cells were cultured into 35 mm culture dish as described earlier. Briefly, cells were treated with 500 μM of H_2O_2 for approx. 2h for ROS generation under serum-free conditions. Cells were then allowed to grow in different culture conditions (PDA-AMSN, H_2O_2 + AMSN) for further 24 h after that cell were washed with PBS and stained with 5 μM of JC-1 dye for 30 min at 37 °C. After the staining period cells were washed and imaged under a fluorescent microscope. Mitochondria depolarization in each group was calculated by the ratio of red to green fluorescent intensity per cell in different groups using NIH Image J analysis software.

2.3.20 Western Blotting (WB): SH-SY5Y cells, after treatment with PDA-AMSN, were used to isolate the total protein for WB analysis. The cell pellet was suspended in lysis buffer along with protease and phosphatase inhibitor cocktail. Total protein was isolated after centrifuging the cell pellet at 20,000 g for 30 min after incubating for 30 min on ice. The total protein was quantified using Bradford's assay and equal amount of protein (20 μg) was electrophoretically resolved on gel electrophoresis and transferred to PVDF membrane for 70 min in a wet condition (Bio-rad). Membrane were blocked in 5% BSA prepared in TBST at RT for 2 hrs followed by overnight incubation with primary antibody against GAPDH (Rabbit mAb, 14C10, 1:1000), Bcl-xL (Rabbit mAb, 2762, 1:1000), Bax (Rabbit mAb, 2772, 1:1000) Cleaved Caspase 3 (Rabbit mAb, 9661, 1:1000), IL-6 (Mouse mAb, Abcam ab9324, 1:1000) and Bad (Rabbit

mAb, 9292, 1:1000) at 4°C. Further membrane was incubated with respective horseradish peroxidase (HRP) conjugated secondary antibody (Anti-Rabbit, IgG HRP linked, 7074) for 2 h at RT, and the blot was developed using Bio-rad gel doc system.

2.3.21 In Vitro Release of FITC-AMSN from PANAP Hydrogel: 1 mL FITC-AMSN loaded hydrogel was prepared in a glass vial for the in vitro release assay by adding FITC-AMSN within gel. An equal volume of PBS was added on top of hydrogel and sequentially withdrawn at a predetermined time interval to measure the fluorescence spectra (JASCO FP-8300 ST SPECTROFLUOROMETER) of the released drug. Each time the sample was taken out, the vial was refilled with an equal amount of fresh PBS.

2.3.22 Cell Culture and Immunocytochemistry of hMSCs: Umbilical cord-derived Human mesenchymal stem cells (hMSCs) obtained from Himedia were routinely grown in mesenchymal stem cell expansion media supplemented with 10% foetal bovine serum (FBS), 1% antibiotic-antimycotic solution, and 100 U penicillin, 100 mg/mL streptomycin in a humidified CO_2 incubator at 37 °C and 5% CO_2. Once the cells reached 70-80% confluence, they were extracted by trypsin-EDTA dissociation at 0.05%, neutralized with an expansion medium, and centrifugated at 2000 rpm for 4 minutes. The cells were further plated according to the assay. All *in vitro* tests were performed on cells that were between passages 5 and 10.

Transdifferentiation of hMSCs into neurons was performed in a single step. At 70% confluence, the cells were collected and plated at a density of 3×10^4 cells / cm^2 and allowed to grow for 24 hrs after that the cells were treated with 57 µg/mL of PDA-AMSN-D and maintained in low serum (1% FBS) neurobasal medium for up to 7 days. After 7 days of observation, cells were put through immunocytochemistry (ICC). Retinoic acid (R.A.), a well-known retinol acid derivative, was employed as a positive control at a concentration of 5 µM.

For double ICC after completion of 7 days' cells were fixed in 4% formaldehyde at 37 °C for 1 h, washed with filtered PBS, and permeabilized with 0.1% Triton X-100 for 30 min containing 1% BSA for blocking. After two additional washes with filtered PBS, the cells were incubated with primary antibodies (Tuj1 CST 2146, GFAP Abcam ab7260) overnight at 4 °C. Following the primary antibody incubation, the cells were washed twice with PBS again and then incubated with Goat Anti-Rabbit IgG (H + L) FITC conjugate (Millipore 12-507) secondary antibodies. To visualize the cell nuclei, nuclear staining was performed using DAPI for a duration of 30 minutes

2.3.23 Electrophysiology of hMSCs-derived Neurons: For the electrophysiological recordings cells were grown on gel-coated 18mm coverslips as discussed in the earlier sections.[38] Before recording the pipette solution was made as follows 130 mM K-gluconate, 4 mM Mg-ATP, 11 mM EGTA, 10 mM HEPES, and 1 mM CaCl2 (pH 7.2; osmolarity 290–295 mOsm). After completion of the differentiation process the cells were placed on the recording surface in aCSF (artificial cerebrospinal fluid). Further, cells were patched using an Olympus IX83 fluorescent microscope. For patch clamp recording the holding potential of cells was kept at -60 mV, sweep was set at 10 ms, and episodic impulse was given after every 50 ms, recording was done using a molecular devices multi clamp 700B axon amplifier.

2.3.24 Primary Mixed Culture of Rat Hippocampal Neuron: E14-E16 female pregnant rats were used for the culture of primary cortical neurons as described in our previously reported protocol.[39] Briefly, cortical neurons were cultured in poly-*D*-lysine coated culture dish at a density of 1 x 10^5 cells/ mL in neurobasal media supplemented with 2% B27, 200mM GlutaMax, 1% pen-strap, and 1% FBS. Further, the cortical neurons were treated with PDA-AMSN-D for 24 hrs. Cells and neurospheres were used for ICC.

2.3.25 Animals and Experimental Design for Cryogenic Brain Injury: All the animal experiments were carried out in this study received ethical approval from the Institute Animal Ethical Review Committee at IIT Jodhpur, India. 8-10 weeks old 50 adult female Wistar rats, weighing between 210-250 g, were obtained from JNVU Jodhpur, India. Rats were given free access to a diet containing 18% protein and drink water. The animals were accommodated in a controlled environment, maintaining a temperature of 23 ± 2 °C and a 12-hour light/dark cycle, replicating a typical day and night cycle. Before behaviour assessment, the rats underwent a 7-day acclimatisation period.

The animal experiments were conducted in accordance with the prevailing laboratory animal guidelines. CBI was performed according to our previously reported protocol.[5] Briefly, a healthy female Wistar rat was anesthesize first with Intraperitoneally administered 2% xylazine hydrochloride and 10% ketamine hydrochloride at a dose of 20 mg/kg and 80 mg/kg, respectively. Fur was removed from the head and an oblique midline incision was made to cut open the skull. Further, injury site was located with the help of bregma and lambda and the skull of the animal was drilled open and an opening of 5 mm was created so as to create an injury. To inflict the injury, a copper rod predipped into liquid nitrogen was placed into the exposed brain section for a period of 2 min after that the scalp wound was sutured carefully, when CBI model was established, animals were randomly divided into four groups (Sham, Injury, Gel, Gel / PDA-AMSN-D system) (n=6). The PDA-AMSN-D group received the drug-loaded nanoparticles along with the PANAP hydrogel, whereas in the gel group 100 µL of the PANAP was injected into the injury cavity immediately post-injury. The sham group did not receive any treatment only the right parietal craniotomy was performed. Animals were kept warm on a heating blanket until recovery and critically observed for 24 h after the CBI to avoid any accidental death due to CBI.

2.3.26 Measurement of Brain Edema: The measurement of cerebral edema was calculated according to the previously reported protocol with several modifications.[40] The cerebral edema was calculated by measuring the dry and wet brain 3 days after the CBI. All the treatment group brain and control brain wet weight was calculated immediately after fixation and then it was dried in a hot air oven at 95℃ for 3 days and the dry weight was calculated. Water content in the brain was calculated as follows:

$$Brain\ Water\ Content\ (\%) = [Wet\ weight - Dry\ weight]\ /\ Wet\ weight\ x\ 100$$

2.3.27 Determination of Blood Brain Barrier (BBB) Integrity: The BBB permeability was assessed by measuring the extravasation of Evan's Blue (EB) dye.[40] Three days after the CBI, rats were anaesthetized and EB (2%, 2 mL/Kg) dye was injected into the tail vein and allowed to circulate into the blood stream for 4 h. After 4 h the animal was sacrificed, and the brain was isolated after performing transcranial perfusion. The brain was weighed and homogenized in 50% of trichloroacetic acid. The mixture was then centrifuged for 20 min at 10,000 g, and supernatant was collected. The fluorescent intensity of the sample was calculated 620/680 nm. The amount of extravasation of the dye was calculated by converting absorbance values into ng using EB standard absorbance curve.

2.3.28 Tissue Processing and Histochemistry: After perfusion fixation, the tissue samples were collected, following fixation, the tissue samples were cleaned and processed for H and E and cresyl violet staining according to our previously reported protocol.[34] To begin, briefly after processing, 5 µm brain coronal tissue sections obtained are cleared in xylene, rehydrated with gradient ethanol washes and stained with haematoxylin for 2 min. Then, the samples were counterstained with eosin and mounted with DPX. For Nissl staining, slides were first hydrated in decreasing alcohol gradient, followed by staining with 0.5% cresyl violet. Subsequently, the slices were thoroughly washed, dehydrated in increasing ethanol gradient, cleared in xylene and then mounted in DPX. In order to assess the magnitude of the injury, optical brain images were taken immediately after perfusion for the analysis.

2.3.29 Immunofluorescence: Immunofluorescence were performed according to the previously reported protocol with brief modifications.[41] Animals were perfused and fixed with PBS and 10% formalin, respectively, the brain samples was collected and fixed in formalin for another 24 hrs. After that the brain sample were processed accordingly to the protocol and embedded in paraffin, paraffin-embedded blocks were then sliced into 5 µm thickness for immunohistochemistry. The brain slices were first deparaffinized in xylene, rehydrated in gradient ethanol and then incubated with primary antibody (GFAP ab68428, 1:250, Iba1 ab178846 1:2000, NeuN ab104225, 1:500) overnight at 4 °C after performing the antigen retrieval in Tris-EDTA (pH=9), citrate buffer (pH=6) for 30 minutes. After that, the brain slices were washed with PBST and incubated with specific FITC-TRITC-labelled secondary antibodies for 2h at room temperature. Slices were counterstained with DAPI, and all images were acquired using an Olympus IX83 fluorescent microscope.

2.3.30 Measurement of Proinflammatory Cytokines using ELISA for TNF-α and IL-6: Following the CBI and different treatments, the brains were immediately removed and put on an ice-cold plate. The further brain was thoroughly washed with ice-cold PBS (pH 7.4), and preserved at a temperature of -80 °C for subsequent assays. The brain tissue was thoroughly homogenized in 100mg/mL of ice-cold PBS. The expression levels of different cytokines were measured using commercially available ELISA assay kits (Quantikine ELISA).

The relative expression of TNF-α in SH-SY5Y cells was measured in cell lysates using ELISA kits from Quantikine ELISA kit, following the instructions provided by the manufacturer. Briefly, 50 µL of cell supernatant from each group was added into

triplicated along with 50 µL of assay diluent RD1F buffer and incubated for 2 h at the room temperature, following which the solution was aspirated and each well was washed thoroughly with wash buffer and 200 µL of human TNF-α was added for 2 h at room temperature, after the completion of 2h the plate was gently washed and a stopping solution was added into each well and optical density was calculated at 450 nm.

2.3.31 Manual Analysis of Astrocytes and Microglia Morphology: Images were acquired in Olympus IX83 microscope with a 40X objective lens. The manual morphological analysis was conducted utilizing FIJI software (Version 2.0) and the Sholl analysis plugin. In addition, the FIJI Sholl analysis plugin was utilized with default parameters, including a radius step size set to automatic (0.00), an enclosing radius cut-off of 1 intersection, and the Sholl Method set to linear.

2.3.32 Neurological Functional Assessment: The Morris water maze test was performed to evaluate cognitive abilities like learning and memory in rats.[34] The water maze was divided into four directional quadrants, and the platform was concealed in the centre of the target quadrant, approximately one centimetre below the surface of the water. The standard training regimen was prolonged for a total of 5 days. Each animal participated in a total of four separate trials every single day, with the beginning points of each test located in one of the tank's four distinct quadrants. The wall of the tank was decorated with markers for spatial navigation, and the duration of the test was one minute for each trial. The rats that did not make it to the platform within one minute were trained by placing them on the platform and keeping them there for around 20 seconds. Parameters like escape latency, distance travelled etc., were recorded as learning indicators over the course of 5 days. On the final day of testing, a space probe experiment was performed in which the platform was removed, the animal was placed in the contralateral platform, and their swimming pattern was observed for a period of 60 seconds.

2.3.33 Statistical Analysis: All of the results that were presented as the mean accompanied by the standard deviation (SD) were representative of at least three or four separate experiments. When comparing the mean values of more than two different groups, a one-way analysis of variance (ANOVA) was performed on the data using Prism software (GraphPad Software Inc., Version 3.0, California, United States). A statistic was considered statistically significant if it had a p-value of less than 0.05. Some components of the figures were made using Biorender.

2.4 RESULTS AND DISCUSSIONS

2.4.1 Synthesis and Characterization of Bioactive Nanoparticles: Overall, the proposed design aims to deliver a neurogenic small molecule drug at the injury site for neurogenesis and simultaneously eradicate excessive ROS with the help of PDA coating. While conventional MSNs are recognized for their porous structure, the typical pore size has been limited to around ~2 nm in diameter. For this purpose, we prepared large pore-size mesoporous silica nanoparticles (L-MSN) using hexane as a pore-size expander. Both conventional (S-MSN) and L-MSN were synthesized using

the sol-gel synthesis method, as reported in the previous literature, with several modifications.[25]

In this sol-gel process, a surfactant known as cetyltrimethylammonium bromide (CTAB) was employed as a liquid crystal template. CTAB possesses hydrophilic head groups and long hydrophobic organic tails, enabling it to spontaneously self-aggregate into micelles. Field emission scanning electron microscopy (FE-SEM) showed that both types of nanoparticles (S-MSN and L-MSN) are highly dispersible and spherical (**Figure 2.2 A, B**). The size of these two types of nanoparticles was further analyzed by FE-SEM images (**Figure 2.2 C, D**). The average size of S-MSN was found to be 125.70 ± 19.8 nm with a size distribution ranging from 80-180 nm (**Figure 2.4 C**), while for the L-MSN, the average size was found to be 145.91 ± 30.65 nm with a size distribution ranging from 80-220 nm (**Figure 2.2 D**).

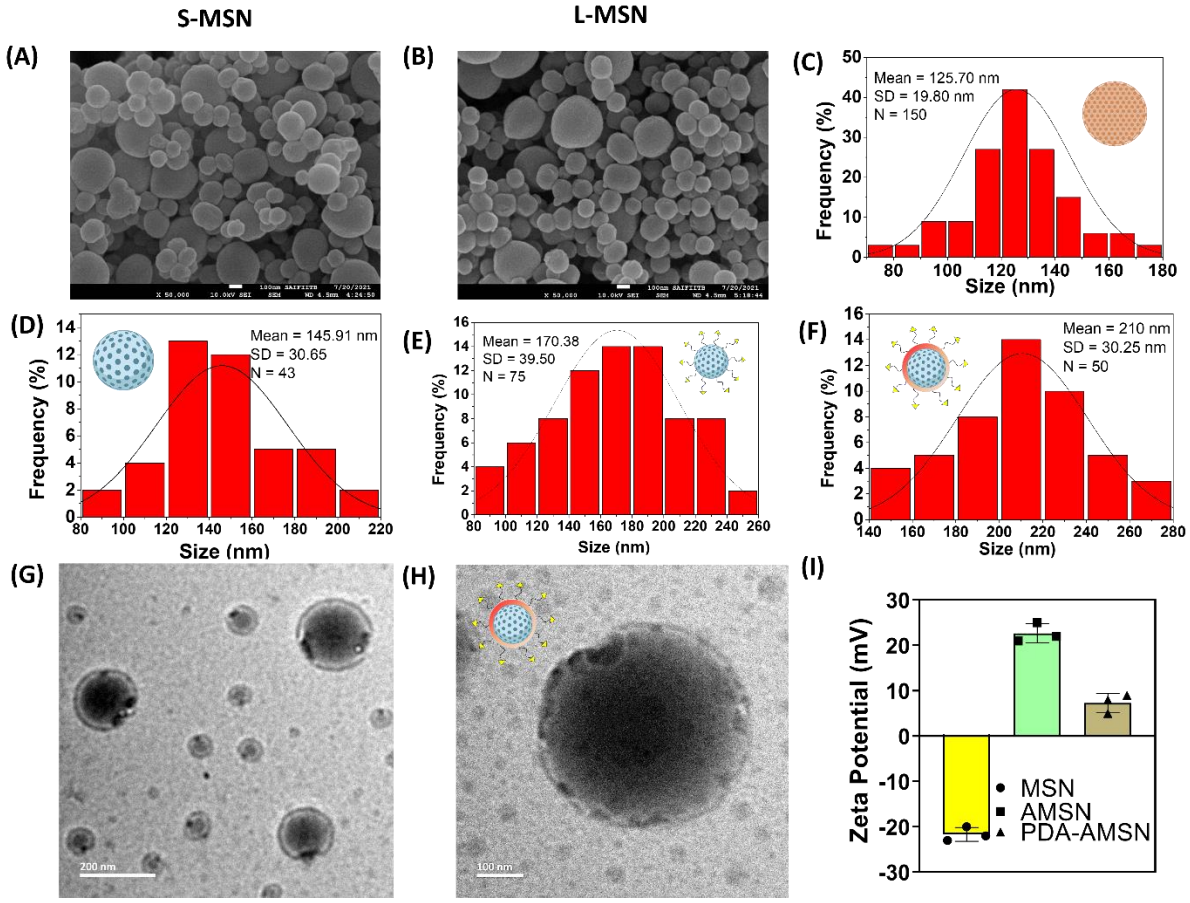


Figure 2.2 FE-SEM images of the synthesized (A) S-MSN, (B) L-MSN, (C), (D), (E) and (F) size distribution analysis of S-MSN, L-MSN, AMSN & PDA-AMSN, (G) TEM micrograph images of PDA-AMSN, (H) TEM image of single PDA-AMSN, (I) Zeta potential of MSN, AMSN and PDA-AMSN

Nitrogen absorption and desorption tests and Brunauer-Emmett-Teller (BET) analyses showed that S-MSN and L-MSN pore sizes were about 1.62 and 4.15 nm, respectively so that the nanoparticles can load the NCM (**Figure 2.3 Figure 2.4 A-D, Figure 2.5 A, B**). The drug loading capacity (DLC) and drug encapsulation efficiency (DEE) of both types of nanoparticles were evaluated with the help of a small molecule drug, i.e., NCM. As shown in **Figure 2.5 C**, DEE for L-MSN was 71%, and DLC was 16.2%, while for S-MSN, DEE was 51% and DLC was 7.7%, suggesting that L-MSN with large pore

size can hold a higher amount of drug. Hence, L-MSN was used further for all the subsequent assays. Subsequently, to make a strong electrostatic attraction with the cell membrane (negative charge) and enhanced cellular uptake, we modified the as-synthesized L-MSN with an amine group to enhance their positive charge on the surface of large pore-size nanoparticles; these types of NPs are now called as AMSNs (**Figure 2.2 D**). The size of the AMSNs increased significantly compared to the L-MSN; the average size of AMSNs was 170.38 ± 39.50 nm with a size distribution range of 80-280 nm. The increase in size was due to the modification of the amine.

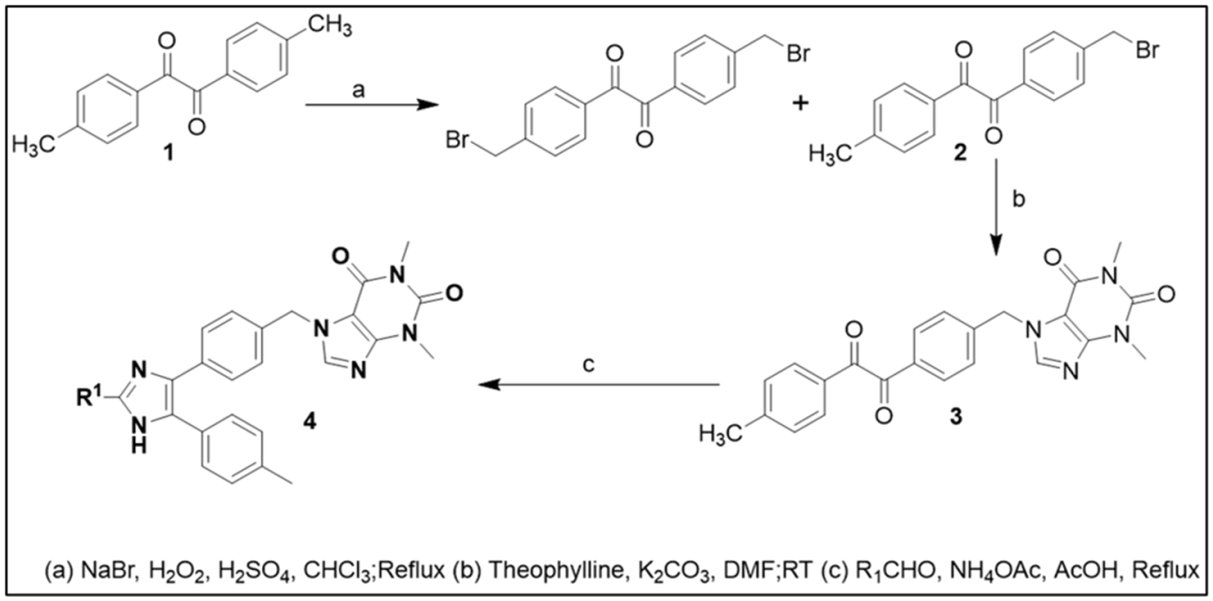


Figure 2.3 Synthetic scheme of Imidazole-based neurogenesis molecule (NCM)

Additionally, the AMSNs are now coated with PDA coating with an aim to improve the biocompatibility of NPs and provide an antioxidant nature to the AMSNs. PDA-coated AMSNs were synthesized by dispersion of AMSNs in dopamine hydrochloride solution while stirring for 12 h. TEM micrograph and FE-SEM images show the successful synthesis of PDA-AMSN. (**Figure 2.5 E**).

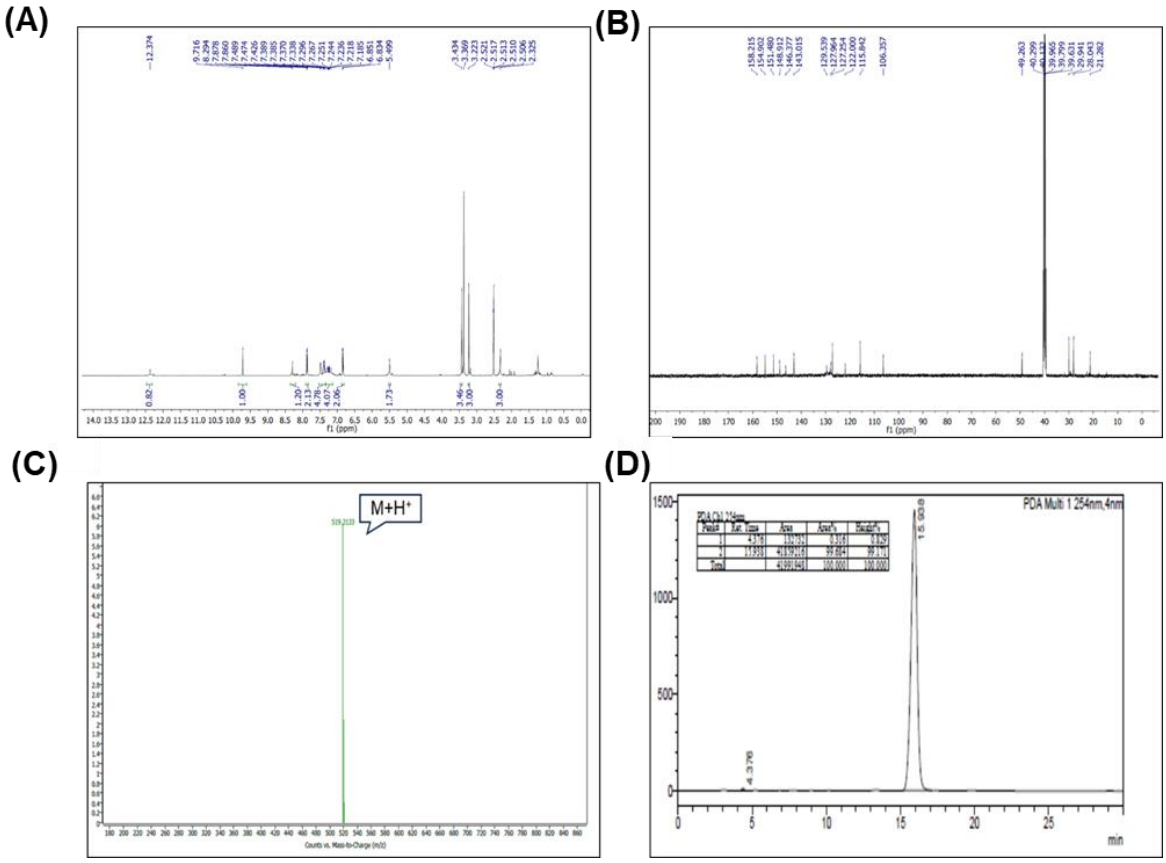


Figure 2.4 (A) 1H & (B) 13C NMR spectra of imidazole-based neurogenesis molecule (NCM) (C) LCMS & (D) HPLC chromatogram of NCM of imidazole-based GSK-3 beta inhibitor neurogenesis molecule.

Furthermore, FT-IR spectral studies were performed, which provide evidence of functionalization of various functional groups in the silica framework. As shown in **Figure 2.5 F**, the broad band peak at 3450 cm^{-1} can be attributed to O-H stretching vibration and surface Si-OH functional groups from the water molecules. The MSNs surface silanol functional groups Si-O-Si are verified at 790 and 1085 cm^{-1}, and Si-O-H functional groups are seen at 970 cm^{-1}, representing the stable formation of a silica framework in all samples. The presence of PDA coating on AMSNs may be confirmed by the peak at 1662 cm^{-1} from the C=C (1675–1640 cm^{-1}) stretching vibration in PDA's indole structure and the faint absorption peak of benzene at 1600-1450 cm^{-1}.

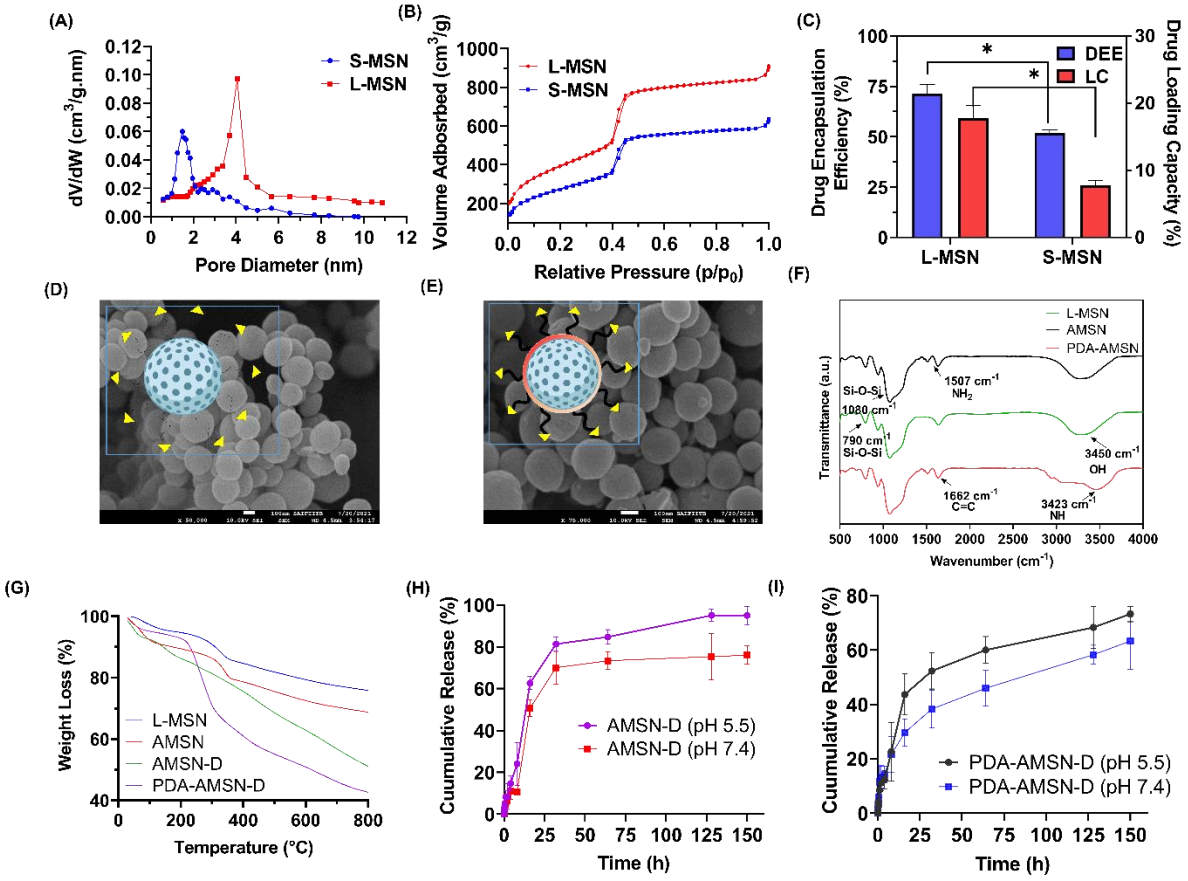


Figure 2.5 Characterization of nanoparticles. (A) and (B) Pore size distribution and nitrogen absorption–desorption isotherms of L-MSN and S-MSN, respectively. (C) Drug encapsulation efficiency (EE) and drug loading capacity (DLC) of model drug. (D) and (E) Representative FE-SEM images of AMSN and PDA-AMSN, respectively. Scale bar corresponds to 100 nm. (F) FT-IR spectra of L-MSN, AMSN, and PDA-AMSN. (G) TGA analysis of L-MSN, AMSN, AMSN-D, and PDA-AMSN-D. (H) In vitro drug release profile of AMSN-D at pH 5.5 and 7.4 at different times (n = 3 per group). (I) In vitro drug release profile of PDA-AMSN-D at pH 5.5 and 7.4 at different times (n = 3 per group). Data represent mean ± SD of three independent experiments. The statistical significance of all the results was calculated by using a one-way analysis of variance (ANOVA) with Tukey's post hoc test. *p < 0.05, **p < 0.01, and ****p < 0.0001 in GraphPad Prism.

Moreover, the drug loading and surface functionalization were also confirmed with the help of TGA; the TGA analysis results are displayed in **Figure 2.5 G**. The weight loss from MSNs, AMSNs, AMSN-D and PDA-AMSN-D were 75.81%, 68.70%, 50.93% and 42.59% when heated in a N_2 environment at 800 °C, respectively. An ~7% weight loss from AMSNs to MSNs could be attributed to the removal of the amine group from the AMSNs. Additionally, a further 18% weight loss from AMSN-D to AMSNs was consistent with the drug loading efficiency (17.7%), and 8% weight loss from AMSN-D to PDA-AMSN-D could be due to the removal of PDA from the silica surface. The zeta potential plays a crucial role in maintaining the stability of nanoparticles in suspension by facilitating electrostatic repulsion among the particles. As shown in **Figure 2.5 I**, the zeta potential of L-MSN was determined to be -21.6 ± 1.24 mV. This can be attributed to the existence of silanol groups that carry a negative charge. AMSN has a zeta potential of +22.6 ± 1.69 mV due to the protonation of the amine group present on the surface of L-MSN. After surface modification with PDA, the zeta

potential of PDA-AMSN decreased to +7.3 ± 1.7 mV, which can be attributed to the deprotonation of PDA coating phenolic hydroxyl groups at neutral conditions.

In addition to determining the retention efficiency of dug loading before and after PDA coating, we have tested the release of small molecule drugs from AMSN-D and PDA-AMSN-D at pH 5.5 and pH 7.4. Around 90%, 80% and 70% of the drug has been released from the AMSN-D at pH 5.5, 6.8 and 7.4, respectively, on day 7. Moreover, around 70%, 60% and 65% of the drug have been released from PDA-AMSN-D at pH 5.5, 6.8 and 7.4, respectively, on day 7 (**Figure 2.5 H, I, Figure 2.6**).

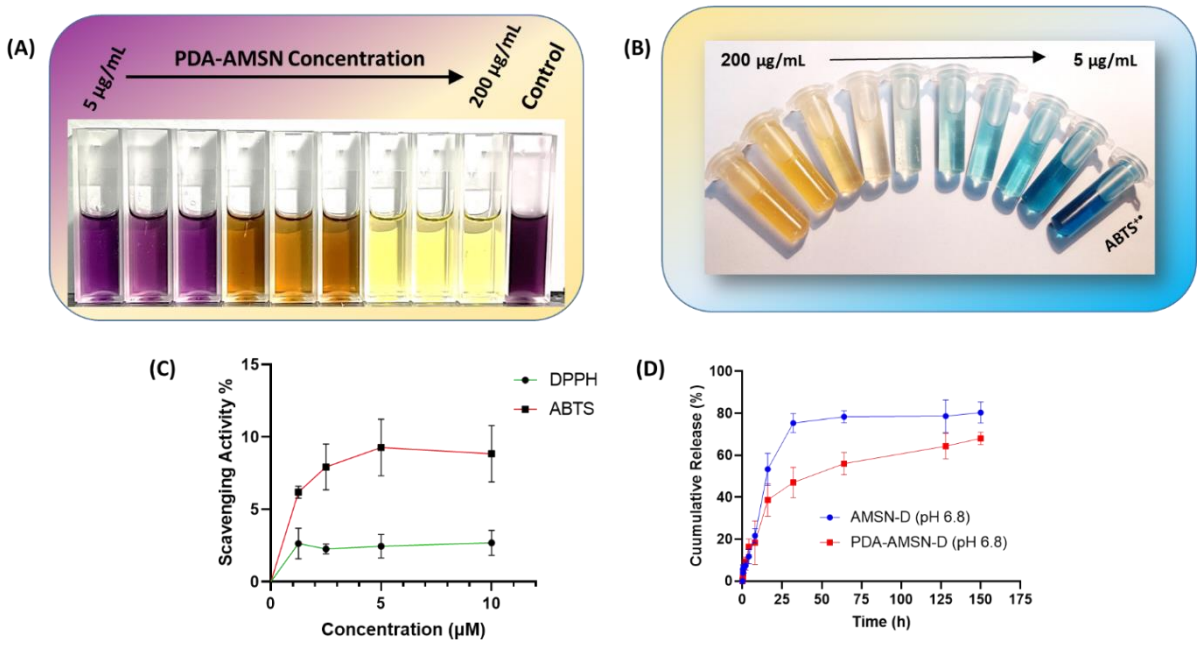


Figure 2.6 (A) Visual representation of colorimetric change in the DPPH solution upon incubation/addition of or with increasing concentration of PDA-AMSN from left to right. (B) Visual representation of colorimetric change in the ABTS free radical upon reacting with decreasing concentration of PDA-AMSN from left to right. (C) DPPH and ABTS free radical scavenging activity of NCM, (D) *In vitro* drug release profile of AMSN-D and PDA-AMSN-D at pH 6.8 at different time (n=3 per group). Data represent mean ± SD of three independent experiments.

Therefore, the drug release from MSN-based nanocarriers is found to be dependent on the pH value and surface modification. Together, these results show that we successfully synthesized two different types of nanoparticles with almost similar size and different pore sizes and surface-coated the AMSN with PDA to provide them antioxidant properties, which could be used as a Trojan horse for drug delivery.

2.4.2 Free Radical Scavenging Ability of Bioactive Nanoparticles: After the comprehensive characterization of PDA-AMSNs, their multiple antioxidant properties were evaluated. Owing to its PDA coating, these bioactive PDA-AMSNs exhibit an impressive ability to scavenge free radicals (ROS and RNS) and have excellent antioxidative ability. 2,2-diphenyl-1-picrylhydrazyl (DPPH) and 2,2′-azino-bis(3-ethylbenzothiazoline-6)-sulfonic acid (ABTS) has been widely used as a standard

assay to measure the scavenging ability of any antioxidant materials.[30] Therefore, we characterized the antioxidant activity of our nanoparticles by measuring their DPPH scavenging ability and ABTS radical scavenging assay (**Figure 2.6 A-D**).

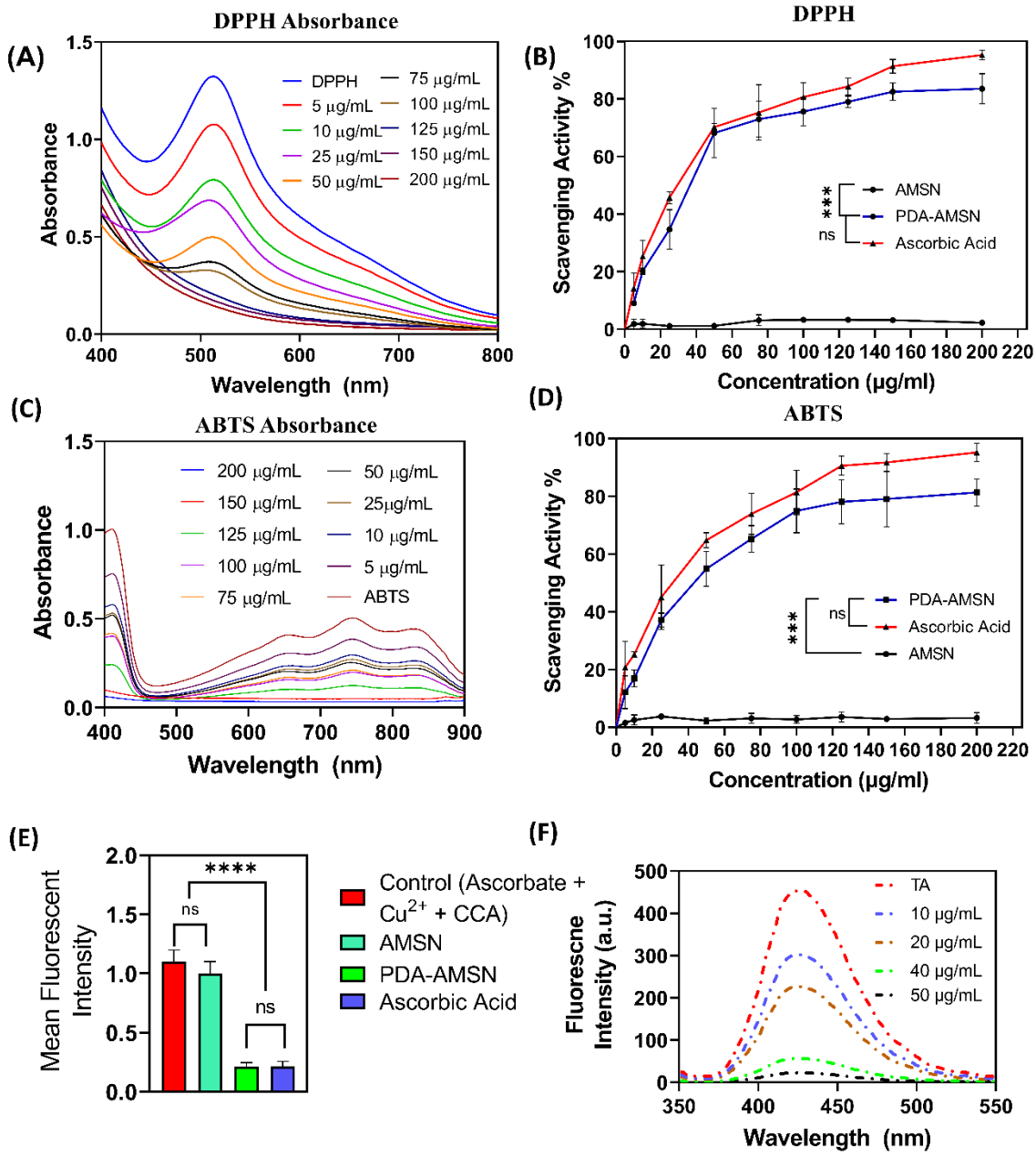


Figure 2.7 In vitro free radical scavenging activity of PDA-AMSN. (A) DPPH absorbance after treating with different concentration of PDA-AMSN. (B) DPPH• radical scavenging rate plotted as their percentage of scavenging rate (%) of PDA-AMSN at different concentrations, respectively. (C) ABTS+• absorbance after treating with different concentrations of PDA-AMSN. (D) ABTS+• radical scavenging rate plotted as their percentage of scavenging rate (%) of PDA-AMSN at different concentrations, respectively. (E) Mean fluorescence intensity (452 nm) of 7-OH-CCA generated in ascorbate assay with different treatment conditions after 1 h incubation at 37 °C. (F) Fluorescence spectra of TA at various concentration of PDA-AMSN. Data represent mean ± SD of three independent experiments. The statistical significance of all the results was calculated by using a one-way analysis of variance (ANOVA) with Tukey's post hoc test. *p < 0.05, **p < 0.01, and ****p < 0.0001 in GraphPad Prism.

In the DPPH assay, the DPPH free radical changes its colour from purple to yellow upon quenching in the presence of an antioxidant. Moreover, the DPPH free radical also shows a typical absorbance peak at around 517 nm in methanol, which decreases upon quenching by an antioxidant.[30] As shown in **Figure 2.7 A**, the decrease in the absorbance of DPPH free radicals could be attributed to the increasing concentration of PDA-AMSNs. In **Figure 2.7 B**, the percentage of DPPH radical quenching was calculated to assess the antioxidant ability of nanoparticles in comparison with the positive control ascorbic acid (5-200 μg/mL). The results show that PDA-AMSNs effectively scavenge free radicals with an EC_{50} value of 46.5 μg/mL, which is slightly better than that of ascorbic acid at 52.4 μg/mL. On the other hand, due to the lack of PDA coating on AMSNs, they do not exhibit any antioxidant activity. Overall, to reiterate, we can say that owing to its PDA coating, PDA-AMSNs show exceptionally good antioxidant activity. We have also checked the DPPH and ABTS free radical scavenging activity of our designed NCM. To this end, we found that NCM itself does not have any antioxidative properties (**Figure 2.6 C**).

Encouraged by the PDA-AMSNs capacity to scavenge ROS, we looked into whether or not they could also do so for RNS. In this regard, we subjected the PDA-AMSNs to an ABTS assay to measure their capacity to quench stable ABTS radicals. Briefly, ABTS was incubated independently or in the presence of different concentrations of PDA-AMSNs and ascorbic acid (5-200 μg/mL) for 30 min under dark conditions, followed by monitoring the absorbance at 734 nm. It was observed that PDA-AMSNs exhibited excellent scavenging activity compared to the positive control ascorbic acid (**Figure 2.7 C and D**) with an EC_{50} value of 43.8 μg/mL for PDA-AMSN while for ascorbic acid it was 52.8 μg/mL.

The potential of PDA-AMSNs to mitigate the effects of ROS was also assessed through a coumarin-3-carboxylic acid (CCA) assay.[31] CCA assay is a fluorescent detection method to detect •OH (hydroxyl radical) in aqueous solution. In the present analysis, the reducing agent ascorbate facilitates the conversion of Cu^{2+} to Cu^{+}. However, it should be noted that Cu^{+} exhibits a high degree of instability and can readily undergo oxidation, leading to its rapid conversion back to Cu^{2+}. H_2O_2 is a prominent ROS component generated during the aforementioned process. However, upon exposure to H_2O_2, the non-fluorescent CCA underwent a transformation, resulting in the formation of the fluorescent compound known as 7-hydroxycoumarin-3-carboxylic acid (7-OH-CCA). By measuring the intensity of a florescent 7-OH-CCA (λ_{ex} = 385 nm and λ_{em} = 452 nm), the amount of H_2O_2 can be determined in the aqueous solution. As expected, strong fluorescence was detected in the control group (Control + Cu^{2+} + Ascorbate) due to the absence of any antioxidant, while the fluorescent intensity was decreased in the presence of ascorbic acid and PDA-AMSNs (**Figure 2.7 E**). These results conclusively demonstrate that PDA-AMSNs are highly antioxidant and have an exceptional ROS scavenging ability.

Further, the CAT-like activity of PDA-AMSN was evaluated with fluorescence spectroscopy method. The reaction between H_2O_2 and terephthalic acid (TA) results in the formation of 2-hydroxyterephthalic acid, which exhibits a fluorescence peak at a wavelength of 425 nm (**Figure 2.7 F**). Nevertheless, the inclusion of PDA-AMSN leads to a notable decrease in the magnitude of this fluorescence peak through the

efficient facilitation of H_2O_2 degradation. In conclusion, our results unequivocally demonstrate that PDA-AMSN successfully imitate the activity of the catalase enzyme, thus can act as a proficient CAT analogue.

2.4.3 Protective Effect of Nanoparticles on Cell-Based Model of Oxidative Stress Injury: After demonstrating the multifunctional ability of PDA-AMSN to inhibit the multifaceted ROS and RNS toxicity *in vitro*, we investigated their effectiveness in cellular system. To examine the biopotential of PDA-AMSN, first 3-(4,5-dimethylthiazol-2-yl)2,5-diphenyltetrazolium bromide (MTT) assay was performed to test their cytocompatibility in SH-SY5Y neuroblastoma cells.[42] SH-SY5Y cells were treated with different concentrations of PDA-AMSN (7.81 to 1000 µg/mL) and wt% of PANAP and incubated at 37 °C for 24 h. It was observed that PDA-AMSNs showed no apparent toxicity up to 60 µg/mL with high cell viability of >90% compared to untreated cells for 24 h (**Figure 2.8 A**). Also, the PANAP hydrogel does not exhibit any toxicity on SH-SY5Y, as evident in the MTT assay results (**Figure 2.8 B**).

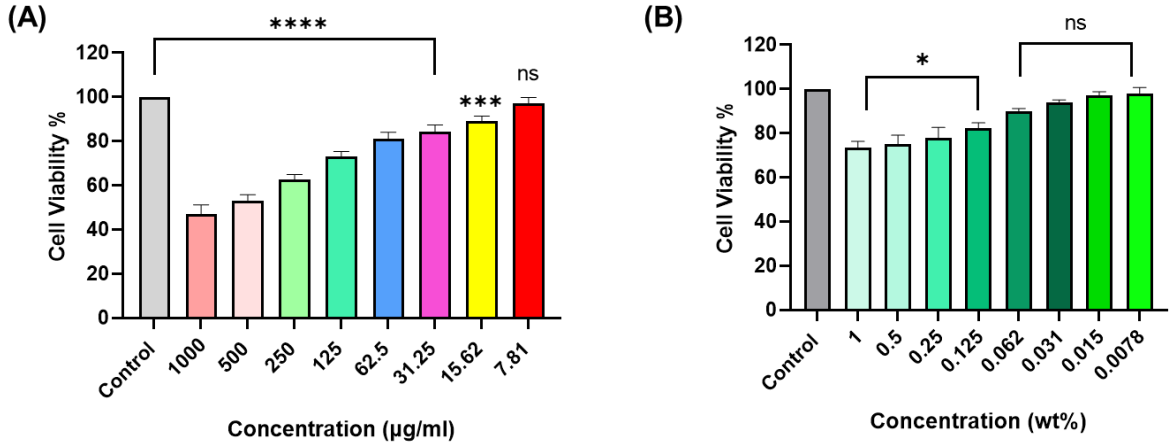


Figure 2.8 Cell viability assay (MTT assay) of SH-SY5Y treated with (A) different concentration (7-1000 µg/mL) of PDA-AMSN nanoparticles and (B) different wt% of PANAP hydrogel. Data are represented as the mean ± s.d. from three independent experiments. Significances are marked as *P < 0.05, **P < 0.01, and ***P < 0.001; one-way analysis of variance (ANOVA).

DNA damage, protein oxidation, lipid peroxidation, generation of ROS and disruption of mitochondrial function are just a handful of the detrimental effects of oxidative stress.[43] In neuronal cells, this oxidative stress ultimately leads to surplus accumulation of ROS, which triggers a cascade of events that leads to neuroinflammation, decreased neurite outgrowth and eventually neuronal cell death.[44] Moreover, individuals with TBI have also been found to have an oxidative stress environment.[45] Therefore, to stimulate the *in vitro* model of TBI, an oxidative stress injury model with SH-SY5Y cells was established. In this regard, we have treated the cells with different concentrations of H_2O_2 (50-1000 µM) for 4 h, to determine the IC_{50} value (**Figure 2.9 A**). Compared with the control group, treatment with 500 µM H_2O_2 showed significant cytotoxicity; therefore, 500 µM of H_2O_2 was used for further experiments. To test the neuroprotective effect of PANAP and PDA-

AMSNs, SH-SY5Y cells were pretreated with 500 µM of H_2O_2 for 4 h before being exposed to different concentrations of PDA-AMSN, MTT cell viability results show that treatment with PDA-AMSNs significantly reduces the H_2O_2 induced cell death in a dose depended on manner (**Figure 2.9 B**) and 40 µg/mL was used in further experiments. For PANAP hydrogel, the cell viability was found to be increased with increasing concentration of peptide hydrogel against H_2O_2 induced oxidative stress. However, best efficacy of PANAP was observedon 80 µM hence it will be used for further *in vitro* assays (**Figure 2.9 C**).

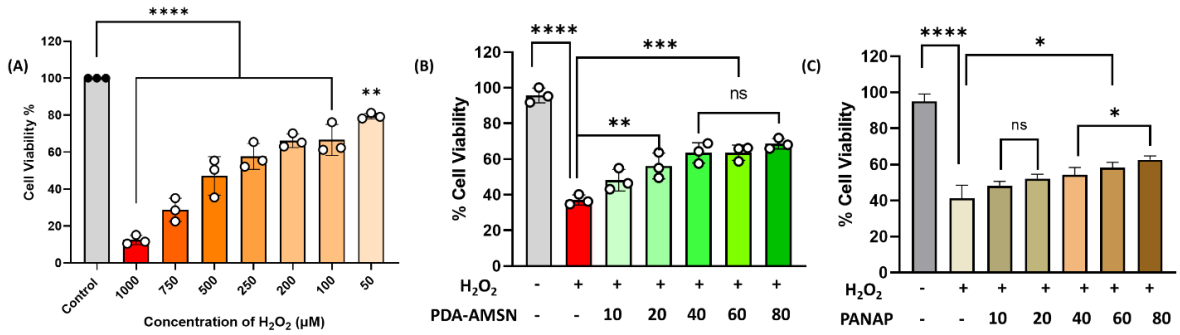


Figure 2.9 (A) Cell viability assay (MTT assay) of SH-SY5Y cells upon treating with different concentration of H_2O_2 to determine the inhibitory concentration of H_2O_2. (B) Cell viability of SH-SY5Y cells with pretreated H_2O_2 followed by treatment of different concentration of PDA-AMSN. (C) Cell viability of SH-SY5Y cells with pretreated H_2O_2 followed by treatment of different concentration of PANAP. Data are represented as the mean ± s.d. from three independent experiments. Significances are marked as *P < 0.05, **P < 0.01, and ***P < 0.001; one-way analysis of variance (ANOVA).

Apoptotic cell death can also be readily identified by determining the morphology of the nuclei. In apoptosis cell death, the nuclei of cells experience certain alterations, such as condensation and fragmentation[46]. As expected, the cells in the control group displayed normal nuclear morphology, exhibiting no abnormalities in the shape of their nuclei or the presence of any apoptotic bodies. However, the nuclei in the H_2O_2 group exhibited noticeable alterations in their morphology, characterized by shrinkage, and heterogeneity in nuclear size and shape (**Figure 2.10**). These changes were a result of the oxidative stress caused by the H_2O_2, which affected the overall integrity of the cells. Contrary to the H_2O_2 group, the PDA-AMSNs treatment group had a healthy nuclei morphology that was better than that of PANAP hydrogel group, suggesting a protective effect of PDA-AMSNs (**Figure 2.10**). This data is also consistent with the fluorescent microscopic analysis of live-dead fluorescent images as shown in **Figure 2.11.**

The *in vitro* ROS scavenging effect of PDA-AMSNs was also determined with the help of a fluorescent DCFH-DA dye. Almost no green fluorescent was observed for the cells without any induced stress injury (**Figure 2.12**). However, cells pretreated with H_2O_2 showed a very strong green fluorescent, indicating a high level of ROS. When the H_2O_2 pretreated cells were further incubated with PDA-AMSNs, there was a decrease in intracellular ROS, as evident from the decrease in intensity of the green signal (**Figure 2.12**). However, when H_2O_2 pretreated cells were treated with AMSN, there was no change in green fluorescent signal compared to the H_2O_2-treated group.

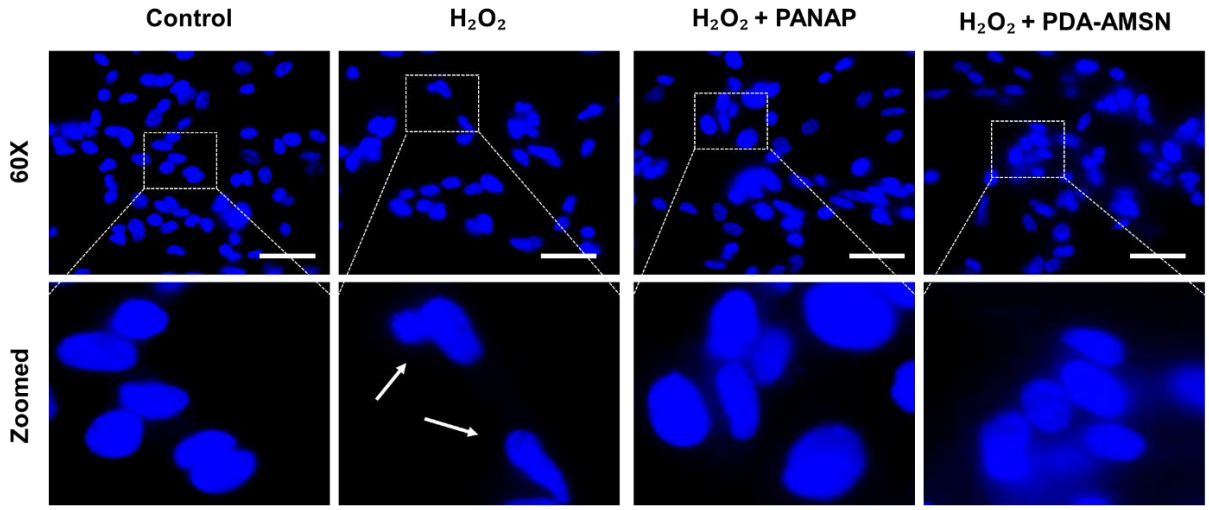


Figure 2.10 Protective effect of PDA-AMSN and determination of total cellular ROS against H2O2-induced ROS stress in SH-SY5Y cells. Fluorescent microscope images of Hoechst staining of SH-SY5Y cells after different treatment conditions. Scale bar corresponds to 20 µm.

Indicating that AMSNs does not have any antioxidant properties and ROS scavenging effect of PDA-AMSNs is due to PDA coating. However, the PANAP hydrogel could able to scavenge the ROS but the PDA-AMSN group showed the highest ROS scavenging as compared to the all other groups.

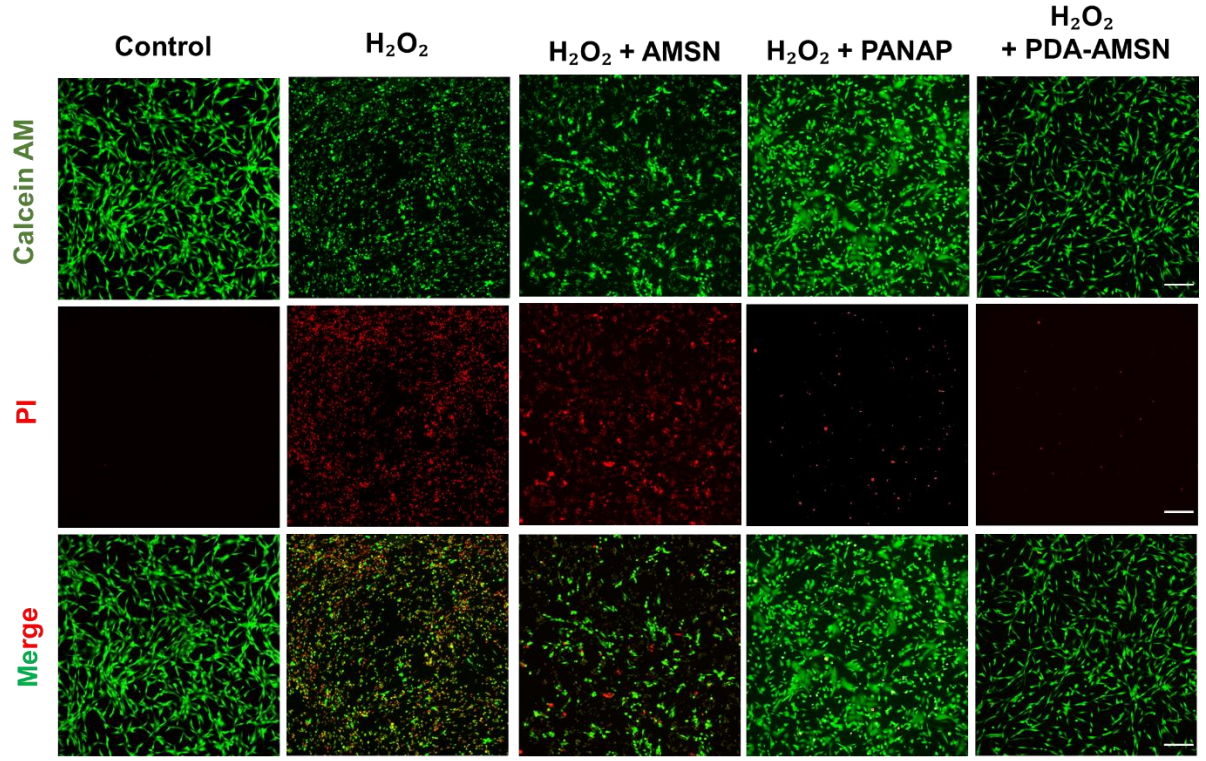


Figure 2.11 Protective effect of PDA-AMSN and determination of total cellular ROS against H_2O_2-induced ROS stress in SH-SY5Y cells. (A) Calcein-AM/PI images of SH-SY5Y treated with H2O2 alone, H_2O_2 + AMSN, and H_2O_2 + PDA-AMSN (40 µg/mL). Scale bar corresponds to 200 µm.

Further, to verify whether H_2O_2 pretreatment overproduced intracellular ROS could be scavenged by PDA-AMSNs, a secondary investigation was carried out on the amount of intracellular ROS generated with the help of CellROX dye.

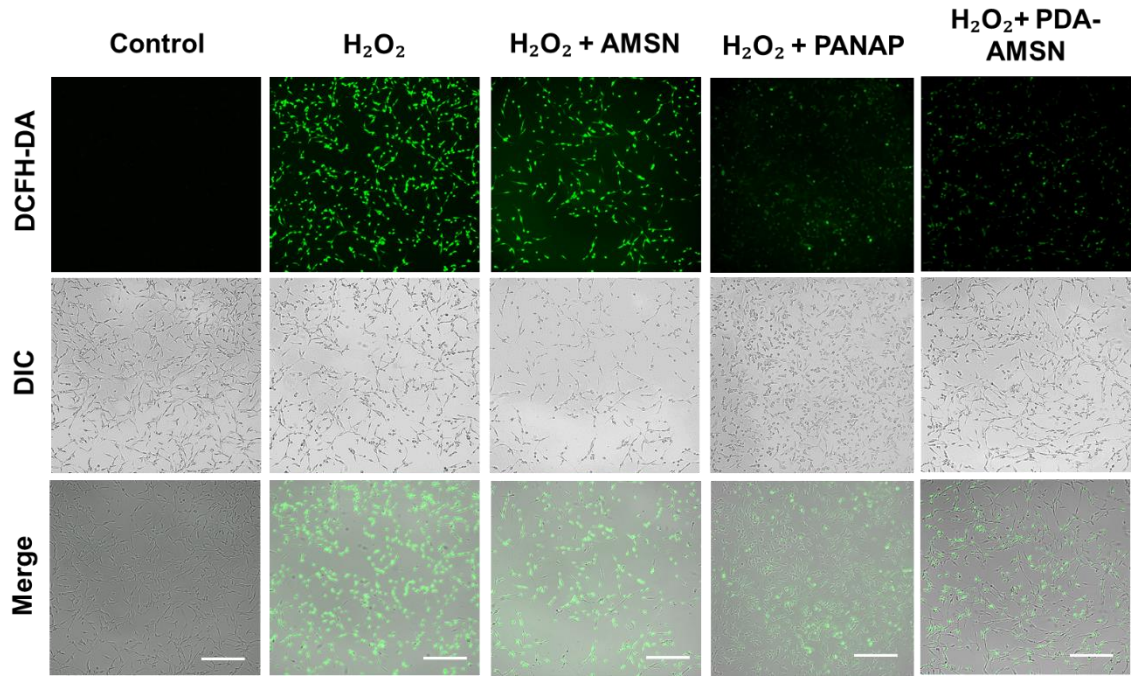


Figure 2.12 Fluorescent and DIC Images of DCFH-DA assay for the detection of total ROS level in SH-SY5Y cells. Scale bar corresponds to 200 µm.

As shown in **Figure 2.13**, there is an increase in red fluorescence in the H_2O_2 pretreatment, whereas H_2O_2 pretreated cells cultured in the presence of PANAP and PDA-AMSNs showed a notable reduction in red intensity. Therefore, these overall results indicate that PDA-AMSNs could effectively scavenge the intracellular overproduced ROS.

2.4.4 Effect of Nanoparticles on Mitochondria Morphology and ROS in H_2O_2 induced Oxidative Stress: Since mitochondria are the site for oxidative phosphorylation and electron transport chain, it is one of the primary sources for producing superoxide and other ROS, this excessive ROS production leads to disruption in mitochondria morphology and membrane potential.[47] Mitochondria play a crucial role in the secondary injury cascade response in TBI; therefore, it is a significant target for therapies to mitigate cellular death and dysfunction.[48] Analysis of mitochondria morphology is pivotal in determining their structure and function. In this study, we evaluated the mitochondrial ROS scavenging ability of PDA-AMSNs using MitoSOX (Red) dye. Live cell images under a fluorescent microscope reveal that compared to PDA-MSNs treated cells, the fluorescent intensity of MitoSOX was higher in H_2O_2-induced cells (**Figure 2.14**). This clearly shows the remarkable ROS scavenging ability of PDA-AMSNs.

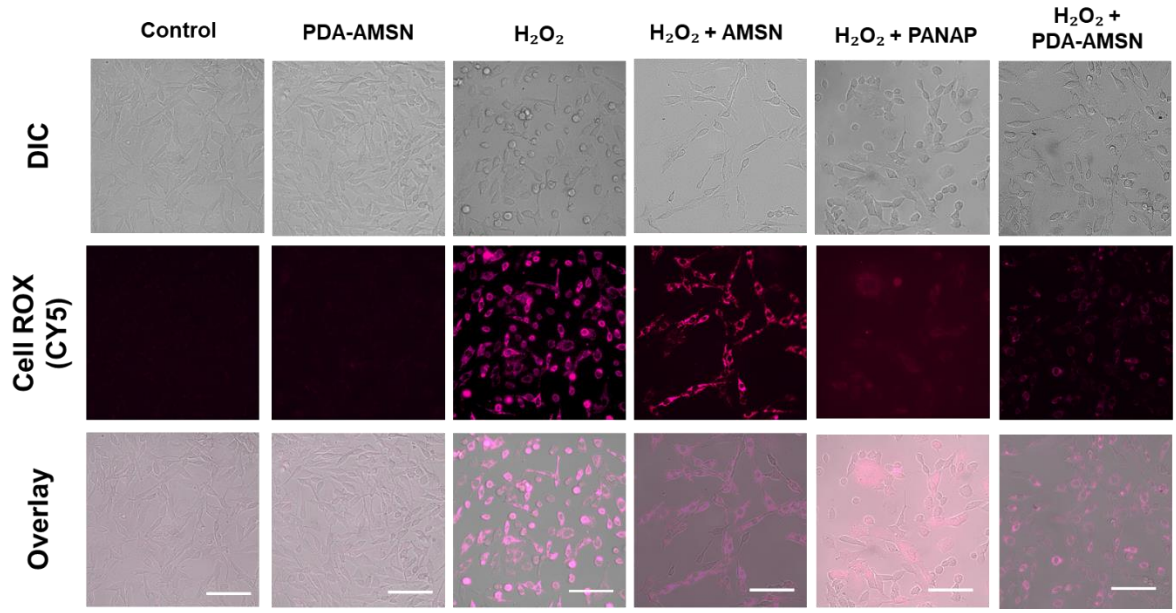


Figure 2.13 Protective effect of PDA-AMSN and determination of total cellular ROS against H_2O_2-induced ROS stress in SH-SY5Y cells. Fluorescent microscopic and DIC images after staining SH-SY5Y cells with CellROX under different treatment conditions. Scale bar corresponds to 50 µm.

Further, to determine the total mitochondrial content and morphology, cells were co-stained with Mitotracker Green. Here, we observed that the mitochondria in the untreated group were primarily healthy filamentous, tubular and in a hyperfused state (**Figure 2.14**). However, when cells were exposed to H_2O_2 the portion of round like mitochondria increased with enhanced swelling, formation of punctiform and disintegration of filamentous structure (**Figure 2.14 A**). This shift from a highly branched morphology state to a round-like state has been inhibited by the PDA-AMSNs (**Figure 2.14 A)**. Meanwhile, to quantify the changes in mitochondria morphology, we processed the raw Mitotracker Green images using the Mitochondria analyzer in Fiji/Image J to analyze the indices like perimeter, circularity and average size.[32] According to our data, after H_2O_2 pretreatment, elevated levels of ROS induced transient abnormalities in the shape of the mitochondria, indicated by the increase in mitochondria perimeter (**Figure 2.14 B**), decrease in mitochondria per cell count (**Figure 2.14 C**), increase in circularity and average size (**Figure 2.14 D,E**).

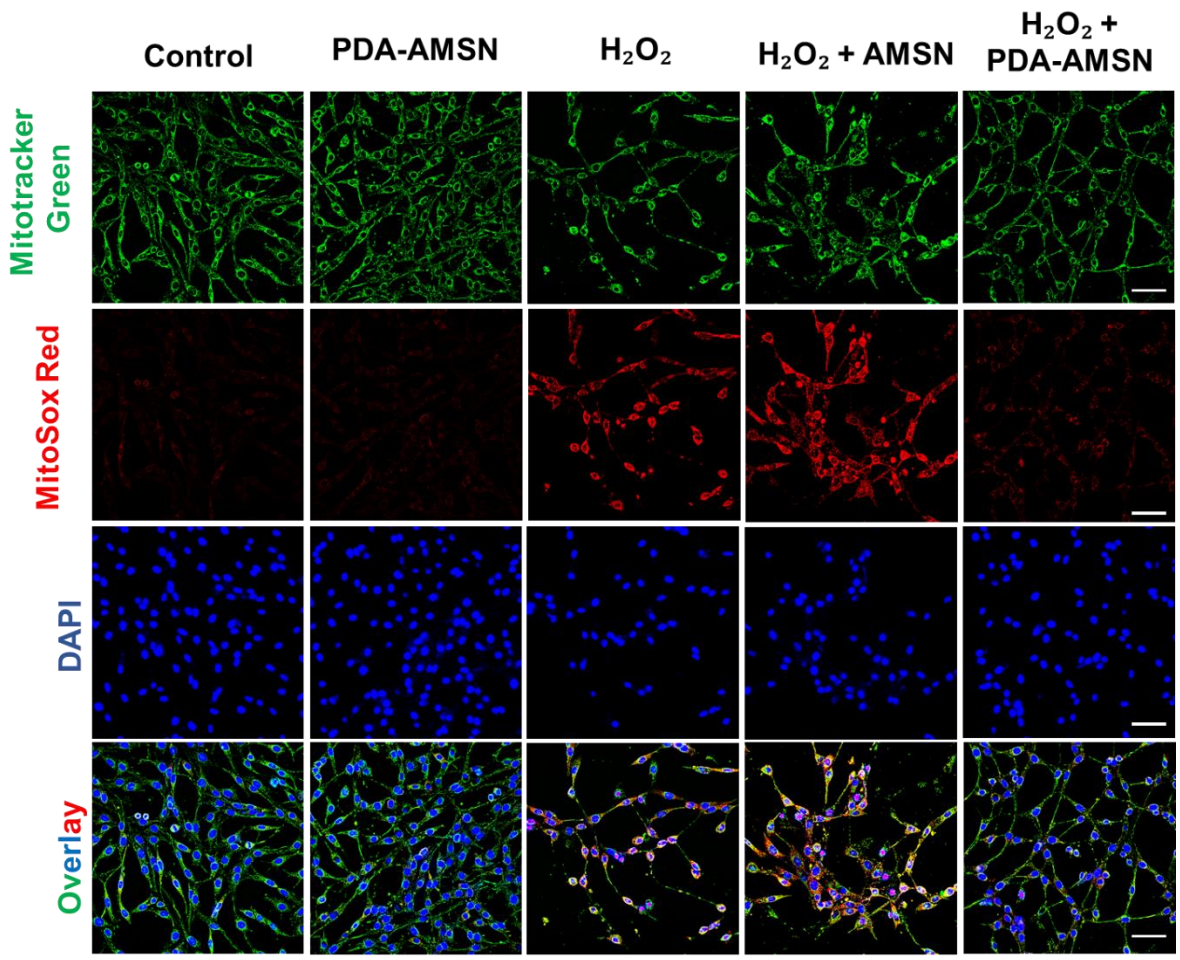


Figure 2.14 PDA-AMSN restores mitochondria morphology and reduces H_2O_2-induced oxidative stress in SH-SY5Y cells. Fluorescent microscopy images of Mitotracker Green and MitoSOX Red staining in fixed SH-SY5Y cells, counterstained with DAPI. Scale Bar corresponds to 50 µm.

We next wondered if our findings with mitochondria fragmentation in H_2O_2 oxidative stress also held true with the hypothesis that apoptosis also leads to loss of mitochondrial membrane potential ($\Delta\Psi_{M,}$ MMP).[37] Therefore, quantitative and qualitative change of $\Delta\Psi_{M\ was}$ measured by fluorescent JC-1 staining. In cells that are in a healthy state, the JC-1 molecules undergo assembly within the matrix of mitochondria to form J-aggregates under the condition of high $\Delta\Psi_M$, which display strong red fluorescence with excitation and emission at 560 and 595 nm, respectively. However, within apoptotic cells, JC-1 cannot gather in the matrix; hence exists the matrix and present in the form of monomers that exhibit a robust green fluorescence emission under the condition of low $\Delta\Psi_{M.}$ Therefore, the quantification of mitochondrial membrane depolarization can be achieved by evaluating the degree of change from red to green fluorescence. Cells were exposed to (40 µg/mL) of free PDA-AMSN, (500 µM) of H_2O_2, (500 µM) of H_2O_2 + (40 µg/mL) of AMSNs and (500 µM) of H_2O_2 + (40 µg/mL) of PDA-AMSNs.

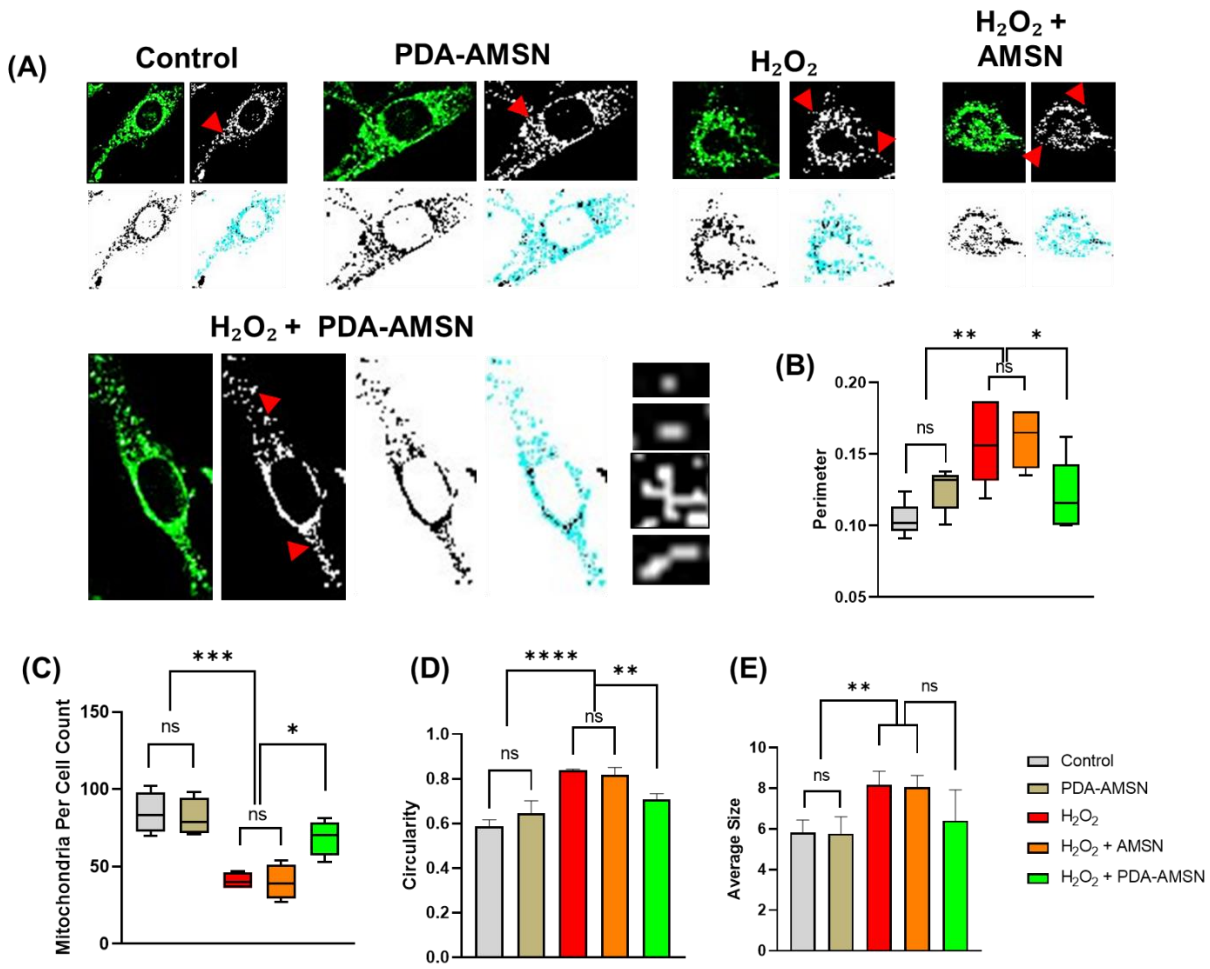


Figure 2.15 PDA-AMSN restores mitochondria morphology and reduces H_2O_2-induced oxidative stress in SH-SY5Y cells. (A) Single cell images of SHSY5Y to detect mitochondria morphology after treating with PDA-AMSN, H_2O_2, H_2O_2 + AMSN, and H_2O_2 + PDA-AMSN. (B) Analysis of different mitochondrial parameters like perimeter, (C) mitochondria per cell count, (D) circularity, and (E) average size under different treatment conditions (n = 3 per group). Data are presented as means ± standard deviations, n = 3 for each group. Data represent mean ± SD of three independent experiments. The statistical significance of all the results was calculated by using a one-way analysis of variance (ANOVA) with Tukey's post hoc test. *p < 0.05, **p < 0.01, and ****p < 0.0001 in GraphPad Prism.

The obtained fluorescent images of mitochondria stained with JC-1 dye (**Figure 2.16 A and B**) showed red fluorescence in control and free PDA-AMSNs treated cells, showing healthy and active mitochondria. However, exposure to H_2O_2 showed a significant red-to-green shift in the fluorescence of JC-1 dye compared to control and free PDA-AMSNs treatments. Thus, mitochondrial membrane integrity is lost by inducing depolarization of $\Delta\Psi_{M,}$ MMP by $H_2O_{2,}$ which has been rescued after treatment with PDA-AMSNs. The $\Delta\Psi_{M,}$ MMP of cells treated with PDA-AMSNs showed a gradual recovery as indicated by the reappearance of red-stained mitochondria. Fluorescence intensity was also quantified in each group using Image J, NIH analysis software (USA) and the ratio of red to aggregate to monomer was calculated, which clearly depicts that H_2O_2 induces loss of membrane potential, which can be rescued after treatment with PDA-AMSNs (**Figure 2.16 B and 2.20 C**).

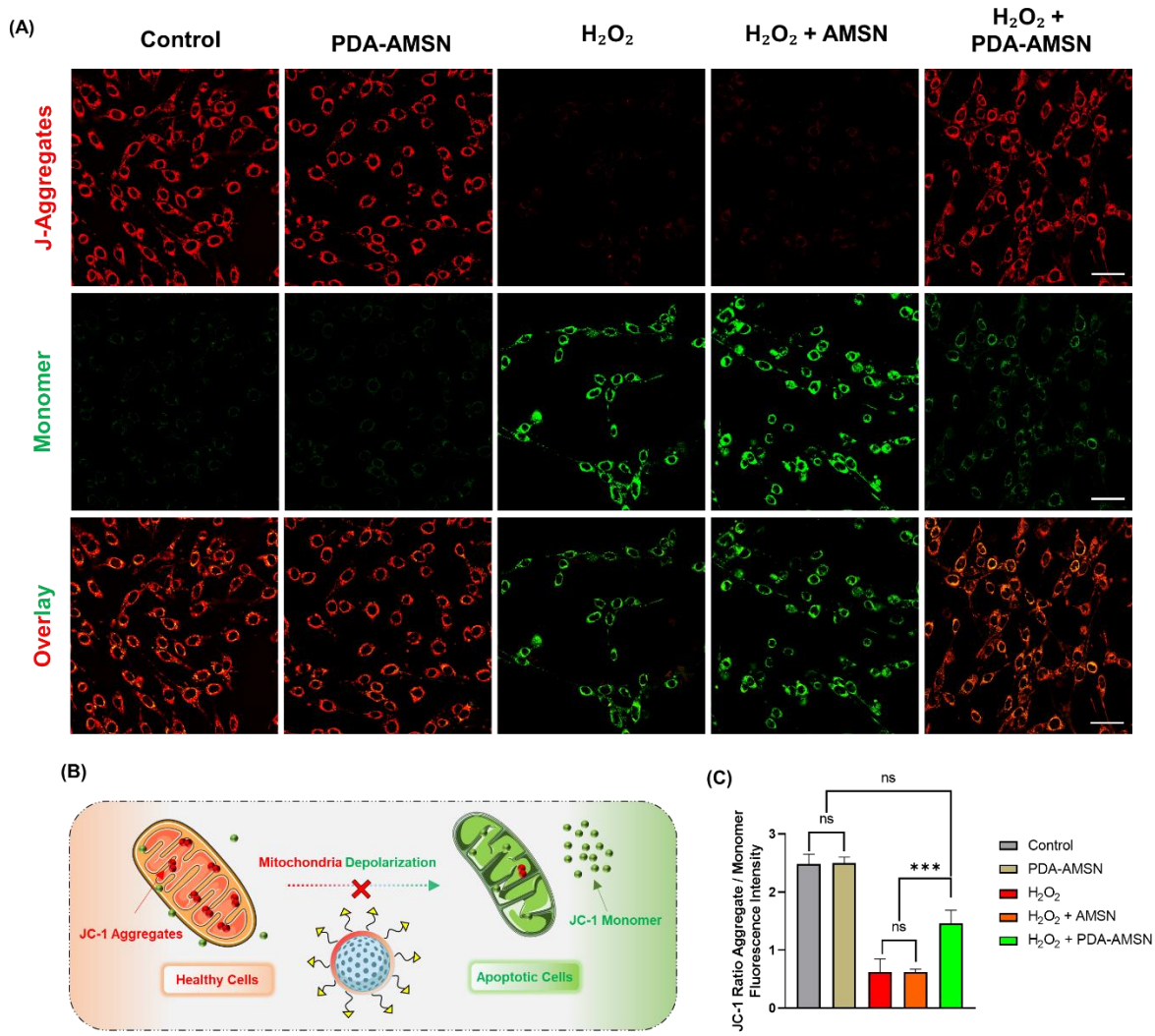


Figure 2.16 PDA-AMSN restores mitochondria morphology and reduces H_2O_2-induced oxidative stress in SH-SY5Y cells. (A) Fluorescent images of JC-1-stained SH-SY5Y images under different treatment conditions. (B) Schematic illustration of the mechanism of JC-1 dye to observe mitochondria depolarization where JC-1 dye shows its reversible fluorescence between its healthy (red fluorescent) and apoptotic (green fluorescent) cells. (C) Quantitative analysis of ratio of aggregates and monomer of JC-1 dye. Data represent mean ± SD of three independent experiments. The statistical significance of all the results was calculated by using a one-way analysis of variance (ANOVA) with Tukey's post hoc test. *p < 0.05, **p < 0.01, and ****p < 0.0001 in GraphPad Prism.

2.4.5 PDA-AMSNs Protect Neuroblastoma SH-SY5Y cells against H_2O_2 Induced Apoptosis and Inflammation: The regulation of the intrinsic apoptotic pathway is predominantly governed by a group of proteins known as the Bcl-2 and caspase families. Changes in the expression levels of pro-apoptotic and anti-apoptotic members within these gene families can have a substantial effect on the beginning of programmed cell death.[49] To determine whether PDA-AMSNs could rescue the H_2O_2-induced apoptosis and acts by modulating the abundance of apoptotic proteins, the protein levels of pro-apoptotic gene Bax, Bad, and cleaved-caspase-3 and anti-apoptotic gene Bcl-xL were measured using western blot analysis. When cells were

pretreated with only H_2O_2, there was a significant increase in pro-apoptotic genes such as Bax, Bad, and cleaved caspase 3. However, when cells were exposed to PDA-AMSNs after pretreating them with H_2O_2, the expression of the pro-apoptotic gene decreased significantly (**Figure 2.17 A**). These results imply that PDA-AMSNs could attenuate H_2O_2-induced apoptosis.

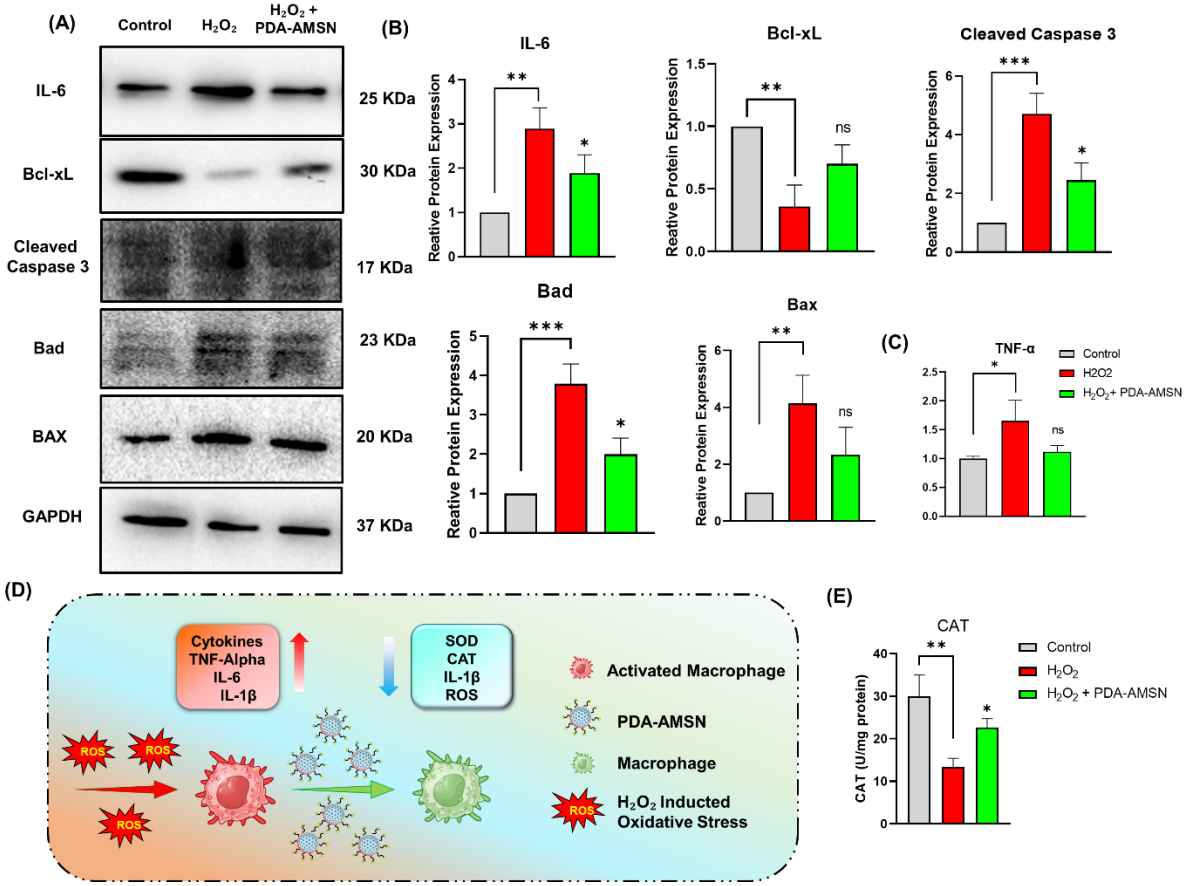


Figure 2.17 Schematic illustration of the anti-inflammation and ROS scavenging activity of PDA-AMSN. (A) Western blot analysis of different apoptotic and inflammatory markers in SH-SY5Y cells and its (B) densitometry analysis. (C) Quantitative analysis of TNF-α levels in SHSY5Y cells as determined by ELISA under different treatment conditions. (D) Schematic illustration of the anti-inflammatory and ROS scavenging activity of PDA-AMSN (E) Representative bar graph showing CAT activity in SH-SY5Y cells. Data are presented as means ± standard deviations, n = 3 for each group. Scale Bar corresponds to 50 µm. Data represent mean ± SD of three independent experiments. The statistical significance of all the results was calculated by using a one-way analysis of variance (ANOVA) with Tukey's post hoc test. *p < 0.05, **p < 0.01, and ****p < 0.0001 in GraphPad Prism.

It has been widely recognized that pro-inflammatory cytokines, such as IL-1β, IL-6, and TNF-α, play a pivotal role in orchestrating neuroinflammation and initiating neuronal death in many neurodegenerative disorders, including TBI.[40] Therefore, we investigate the role of PDA-AMSNs in mitigating pro-inflammation cytokines in SH-SY5Y cells. To determine its expression, we used western blotting and ELISA assay. As shown in **Figure 2.17 A and B** western blot results demonstrate that the pretreatment with H_2O_2 induces the secretion of pro-inflammatory cytokines (IL-6), which has been successfully turned down with the help of PDA-AMSNs. We also

measured the TNF-α, a pro-inflammatory cytokine level, after H_2O_2 pretreatment by ELISA. Consistent with the previous western blot results, TNF-α expression levels were lowered after treatment with PDA-AMSNs in H_2O_2 pre-treated cells. Furthermore, these findings illustrate that PDA-AMSNs can effectively mitigate the H_2O_2-induced cell apoptosis and additionally inhibits the secretion of pro-inflammatory cytokines (**Figure 2.17 C**). Moreover, the aforementioned evidence suggests that PDA-AMSNs exhibit both biocompatibility with neuronal cells and robust scavenging capabilities towards excessive ROS and RNS, hence facilitating neuronal protection.

2.4.6 CAT Mimetic Activity of PDA-AMSN: An increase in oxidative stress results in enhanced production of ROS, which, in turn, leads to excess lipid peroxidation and ultimately leads to cellular apoptosis. Antioxidant enzymes such as SOD and CAT play an important role in driving a series of reactions by converting superoxide radicals into H_2O_2 and H_2O and, finally, into water and oxygen. Hence, maintaining the levels of peroxidase enzyme is of the most important for the cellular defense mechanism. Hence, we also measured the CAT mimetic activity of our PDA-AMSN in SH-SY5Y cells. Cells treated with only H_2O_2 has a very low expression of CAT activity (**Figure 2.17 D and E**). However, the expression of CAT activity has been shown to increase in the PDA-AMSN treatment case. Based on the results obtained from TA assay and CAT mimetic assay, we strongly believe that the present synthesized PDA-AMSN exhibits excellent CAT mimetic activity.

2.4.7 Treatment of hMSCs with PDA-AMSN-D Promotes its Neuronal Differentiation: The Wnt/β-catenin signaling system is of significant importance in regulating patterning, proliferation, and differentiation during the progression of neural development in vertebrates. [38,50]. In addition to its essential role in promoting neuronal survival and neurogenesis, it also serves as a crucial factor in regulating synaptic plasticity and preserving the structural and functional integrity of the blood-brain barrier. In the canonical Wnt pathway, glycogen synthase kinase-3 (GSK-3β), operating as a serine-threonine kinase, plays an essential role in promoting the phosphorylation of β-catenin, which ultimately results in its destruction through the proteasome pathway.[50] The described procedure hinders the movement of β-catenin to the nucleus, a critical stage usually necessary for maintaining the ongoing regeneration of stem cells. Hence, targeting and activating the canonical Wnt pathway with a designed therapeutic can provide a possible avenue in the field of neurogenesis. To this end, our lab has recently synthesized a novel GSK-3β inhibitor for the successful transdifferentiation of hMSCs into functional neurons.[38] Although the designed molecule (NCM) successfully generated neural differentiation from stem cells, several limitations still exist. However, it is crucial to recognize that the administration of small molecules cannot be increased without constraints. This is because exceeding the pharmacological concentration during neural differentiation could lead to a substantial decline in cell viability.[51]

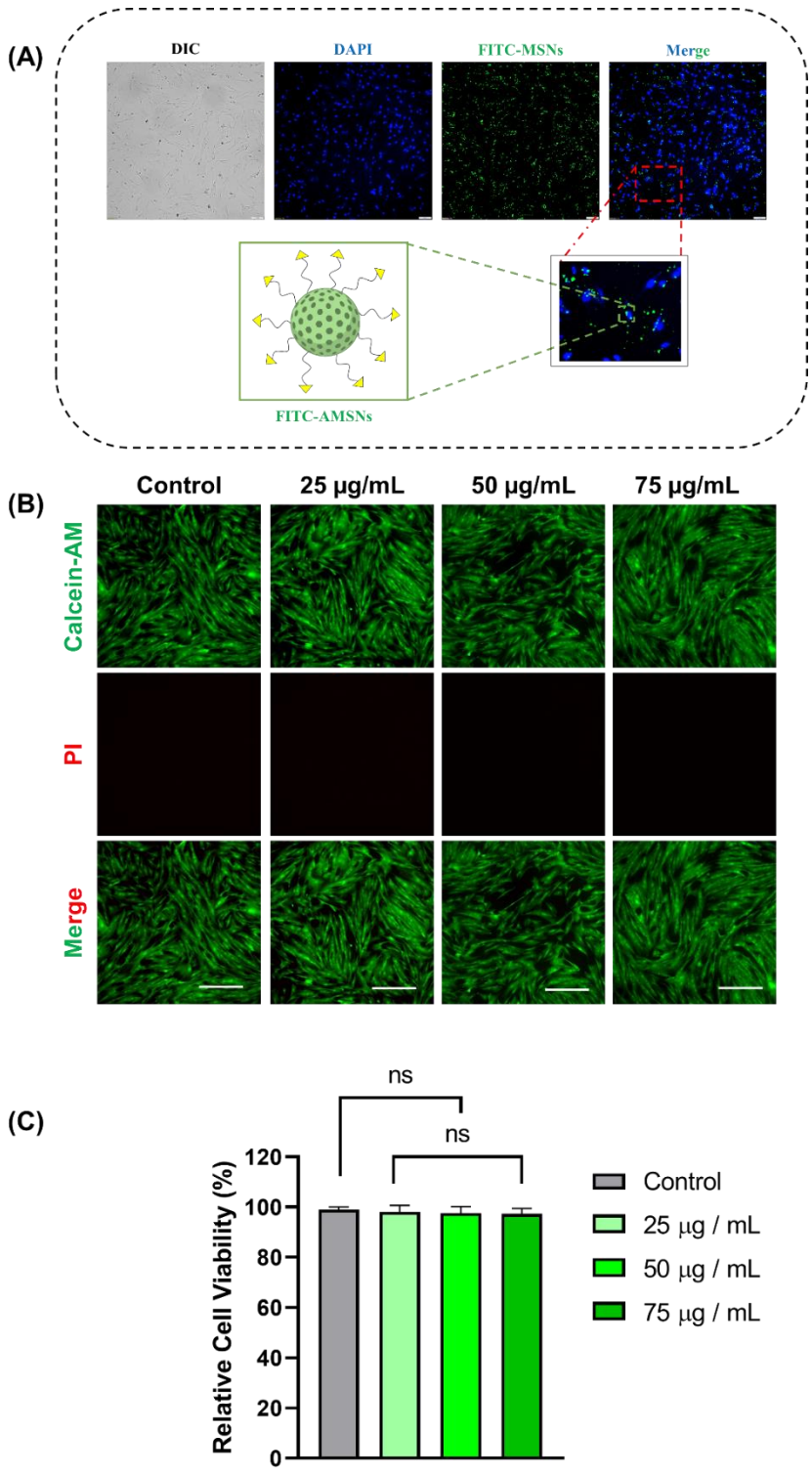


Figure 2.18 (A) Fluorescent microscopic images of hMSCs counter-stained with DAPI treated with FITC tagged MSN to check the cellular uptake efficiency of AMSN. (B) Calcein-AM / PI images of hMSCs after treatment with different concentration of PDA-AMSN. (C) Quantitative analysis of relative cell viability of hMSCs with different concentration of PDA-AMSN calculated with Image J (n=3 per group). Scale bar corresponds to 200 μm.

Furthermore, considering that a small molecule enters the cell membrane through diffusion, it is important to note that the stochastic kinetics associated with the interaction between a small molecule and its target GSK-3β would also be contingent upon the concentration of the small molecule. Therefore, to attain optimal neuronal differentiation, it is imperative to optimize intracellular delivery pathways while minimizing slight molecule loss, thereby facilitating its sustained and adequate supplementation to meet the demands of neural induction. The MSNs have become a prominent instance of intracellular delivery candidates with high functionality, owing to their unique features derived from their complex porous structure. Hence, here we have shown an alternate approach to enhance the conversion of hMSCs cells into functional neural cells by using NCM-loaded PDA-AMSNs (i.e., PDA-AMSN-D). The overall aim here is to achieve a more expedited and effective neural differentiation process. Prior to the differentiation study, the viability of the hMSCs cells was measured after treatment with PDA-AMSN-D. MTT assay results show that PDA-AMSN-D had no impact on the cell viability of hMSCs, even at the particle concentration significantly beyond the threshold necessary for neural induction (57 μg/mL); these results demonstrate the PDA-AMSN-D are biocompatible for sensitive cell lines like hMSCs.

Further, the cellular uptake efficacy of NPs was tested when the hMSCs were treated with FITC-AMSN. We observed that FITC-tagged nanoparticles internalized in the hMSCs nucleus (**Figure 2.18 A**) 24 h post-treatment. The above studies suggest that FITC-AMSN can effectively internalize into the hMSCs and therefore can regulate their biological activities such as differentiation and proliferation. The cytocompatible nature of PDA-AMSN-D was also checked after staining them with Phalloidin to stain the actin filaments. Importantly, it was observed that PDA-AMSN-D does not alter actin filaments even at a higher concentration of 100 μg/mL (**Figure 2.18 B, C and Figure 2.19**). We have also checked the cytobiocompatability of hMSCs along with different concentrations of PDA-AMSN. As shown in the **figure 2.19 A-D,** the PDA-AMSN does not exert any adverse effect on the cell viability of hMSCs as they have minimal red-stained cells (**Figure 2.18 B and C**).

Additionally, the amount of PDA-AMSN-D needed to be treated for successful transdifferentiation was calculated based on the loading capacity and release kinetics. For example, in the case of PDA-AMSN-D, the required amount was 57 μg/mL to ensure sustained release of approximately 5 x 10^{-6} M in 7 days when intracellular uptake occurs. As a control 5 μM of Retinoic acid (R.A.) was added to the differentiation media of hMSCs. The morphological changes of the cells were monitored at regular intervals during the whole process of differentiation in order to assess the efficacy of our designed nanoparticles in generating neuronal cells from stem cells. In particular, the cells subjected to PDA-AMSN-D treatment exhibited a more expedited and robust augmentation in the cytoplasmic component, accompanied by a discernible morphological transformation into a fibrous configuration, in comparison to the cells treated just with R.A. and NCM (**Figure 2.20 A-C**).

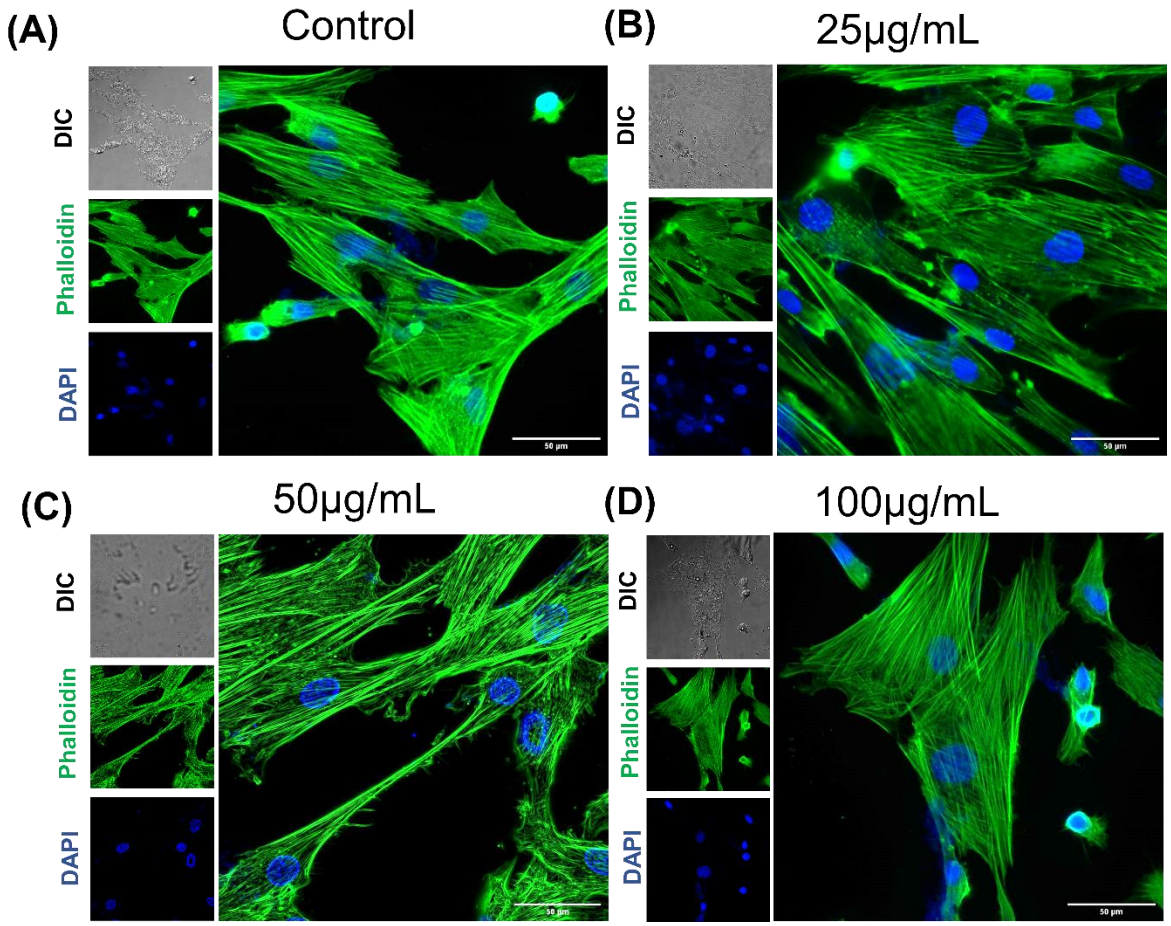


Figure 2.19 Cytoskeleton evaluation, characterization of the hMSCs derived neurons and neurogenic potential of PDA-AMNS-D. Fluorescent microscopic images of hMSCs stained with Phalloidin to check the cytoskeleton and counterstained with DAPI under (A) control condition and after treating with different concertation of PDA-AMSN-D (B) 25 µg/mL, (C) 50 µg/mL, (D) 75 µg/mL for 24 h. Scale bar corresponds to 50 µm.

Further, the patch clamp approach was employed to assess the functioning of transdifferentiated hMSCs. A setup for a single-cell current clamp was established. Electrical stimulation was employed to induce a potential difference inside the cells. Spikes were generated in response to episodic stimulation lasting 50 milliseconds. The neurons that underwent transdifferentiation exhibited action potentials, therefore validating their functional capacity (**Figure 2.21 A**). During a continuous observation period of 3 minutes, uninterrupted instances of spontaneous creation of electrical impulses were seen (**Figure 2.21 B**). In summary, we have shown a novel approach for enhancing neuronal differentiation by integrating NPs into the existing methodology.

2.4.8 Effect of PDA-AMSN-D on Cortical Neuron and Neurosphere Development from Mixed Primary Neuron Culture: Based on our previous empirical findings, it was shown that the application of PDA-AMSN-D promoted the transdifferentiation of neurons from hMSCs. Given this context, our next objective was to examine its differentiation ability in primary rat cortical neurons. In order to accomplish this goal, cortical neurons were isolated from the cortex of Sprague-Dawley rats at embryonic

day 18 (E18) and then cultured on coverslips coated with poly-d-lysine (PDL) solution.[39] After the cells had gently adhered, the plating media was removed from each well and replaced with a new maintenance medium. Upon completion of 24 h, the morphology of the neurons was observed, and neurons were treated with PDA-AMSN-D. Upon further analysis, it was shown that the rat cortical neurons effectively adhered and experienced extensive neuronal growth and dendritic projections in the treatment conditions. The neuronal nature of the primary cortical neurons was further confirmed with ICC by the use of TUJ1 (a neuron-specific marker for the early stage of neuronal differentiation) and MAP2 (a neuron-specific cytoskeletal protein, predominantly localized inside dendrites and has a pivotal function in the process of microtubule construction, also plays a significant role in the stabilization of dendritic morphology during the process of neurogenesis) antibody labelling (**Figure 2.22 A-J**). The MAP2-stained images of primary cortical neurons treated with PDA-AMSN-D clearly demonstrated its capability to enhance the neuronal morphology of cortical neurons by delivering a neurogenic small molecule; it has to be noted here that treatment group showed more extensive neurite length and connection as compared to the control group (**Figure 2.22 A-D**), these NPs also provided added stability to their microtubule network, which might be due to the PDA coating of NPs (**Figure 2.22 E-H**).

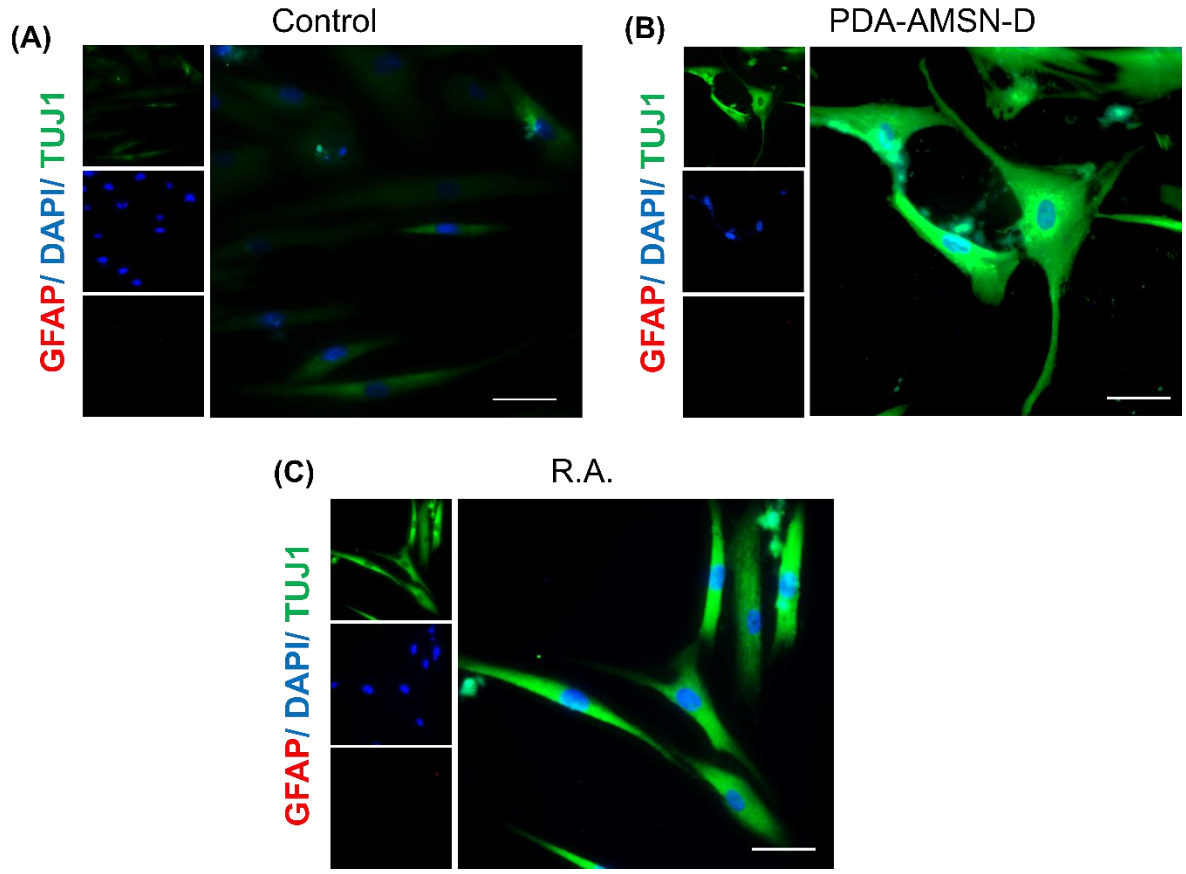


Figure 2.20 Immunocytochemical analysis of hMSCs derived neurons stained with TUJ1 and GFAP under control (A) condition after treating with PDA-AMSN-D (B) and R.A. (C). Scale bar corresponds to 50 µm.

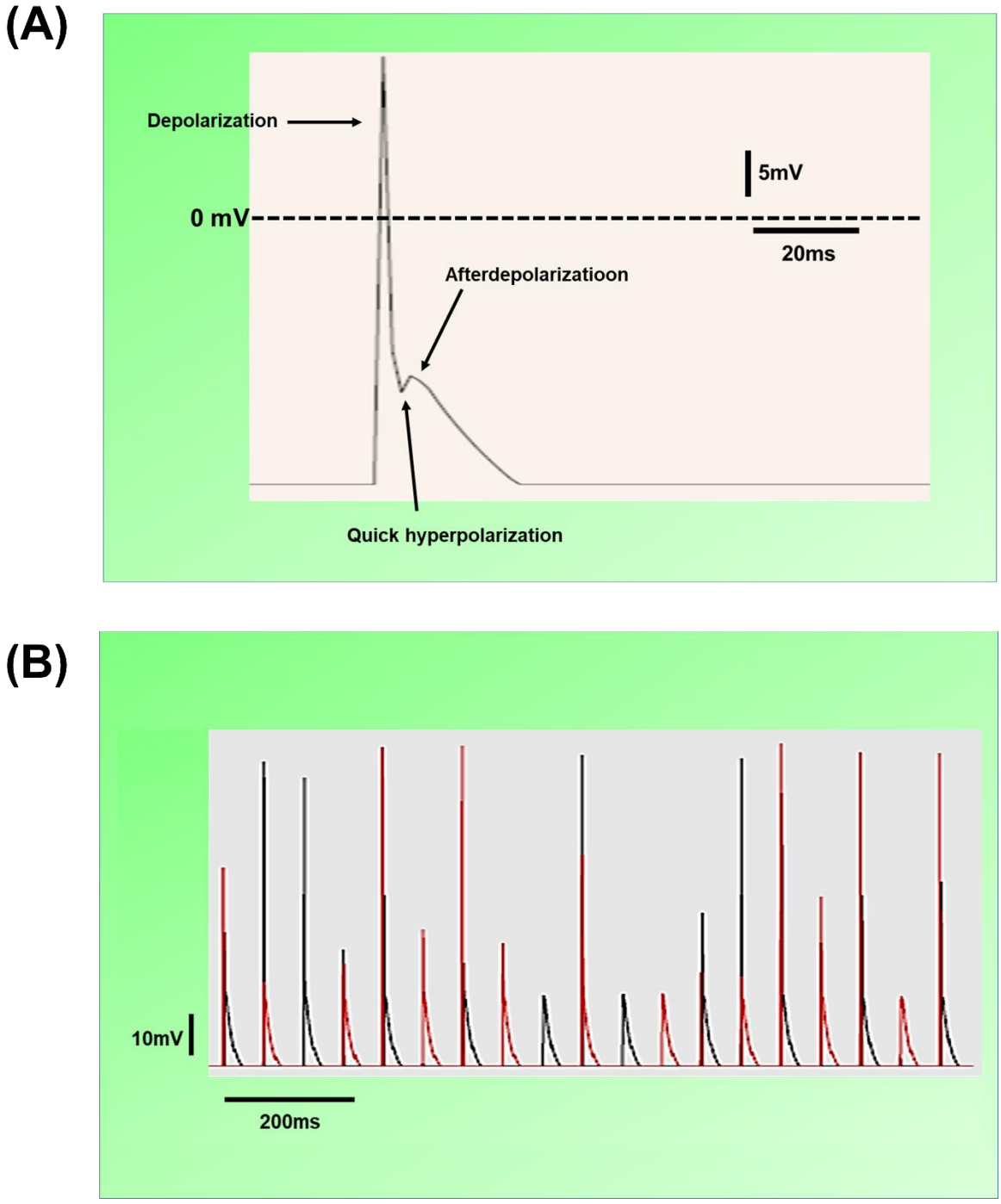


Figure 2.21 (A) and (B) Electrophysiology of transdifferentiated hMSCs showing spikes upon performing voltage clamp and continuous observation period of 3 minutes, uninterrupted instances of spontaneous creation of electrical impulses, respectively.

The neurosphere produced by primary neuron culture presents a novel framework that exhibits a greater similarity to the *in vivo* brain. They have their application in several areas of neuroscience study, encompassing neurotoxicology evaluations, studies into cellular differentiation, and the simulation of neurodegenerative conditions.[39] Hence, in pursuit of this objective, we generated a neurosphere model to assess the efficacy of our nanoparticles in inducing neurosphere differentiation, particularly with regard to neuron-specific genes. It has been observed that the

neurosphere developed by treating with PDA-AMSN-D had a significant lack of astrocyte lineage expression, as compared to the control group (**Figure 2.22 I, J**), which is consistent with the hMSCs transdifferentiation results. This finding provides us with more evidence supporting the neurocompatable nature of PDA-AMSN-D. Hence, these results offer us a crucial benchmark for assessing the efficacy of our nanoparticles in an *in vivo* rat model of CBI.

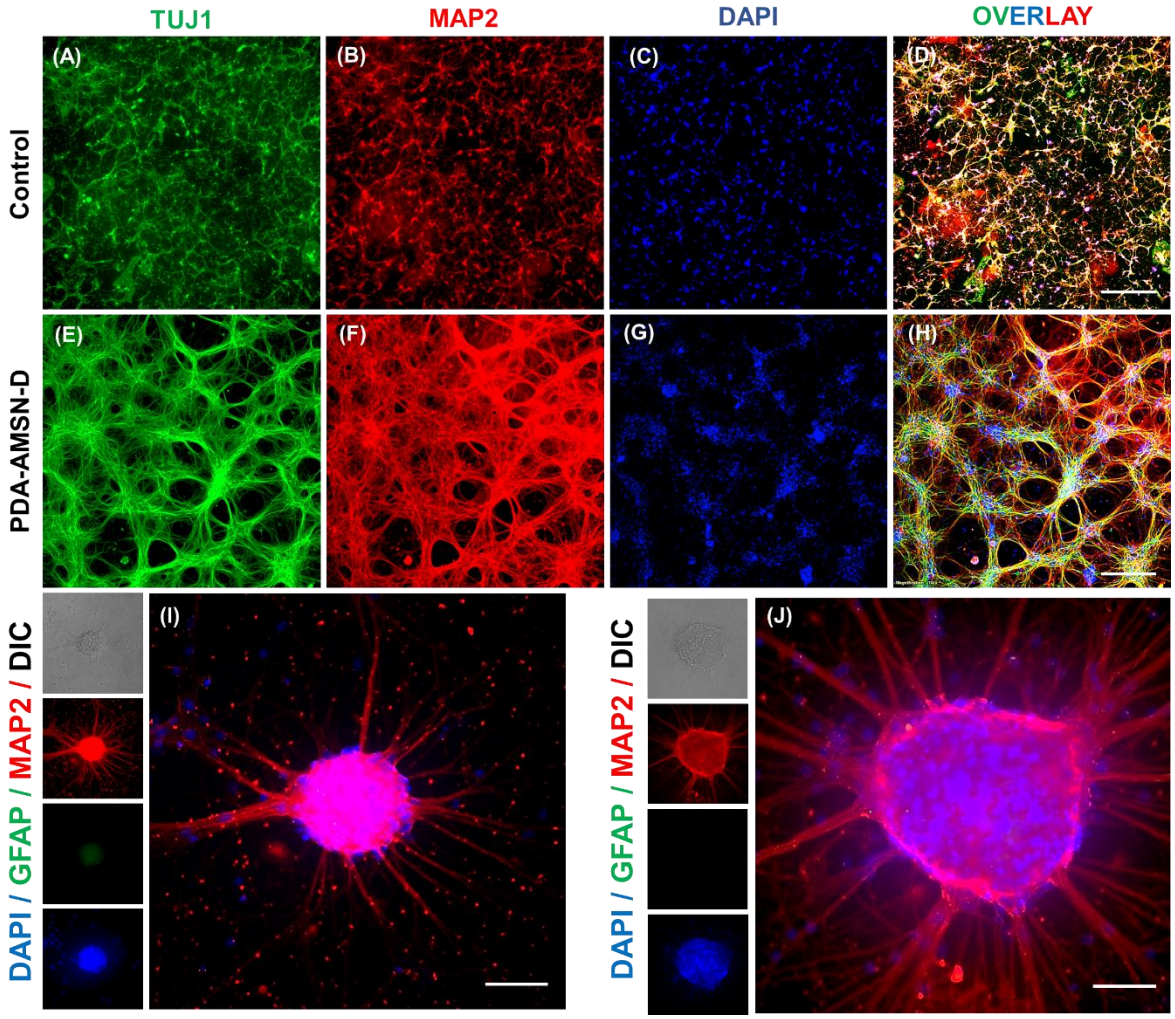
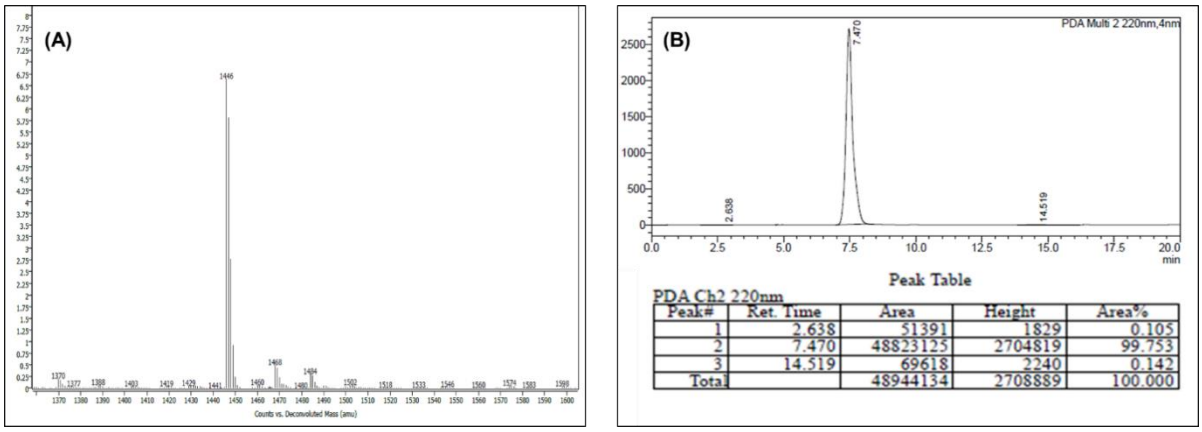


Figure 2.22 (A-H) ICC of E18 primary cortical neurons stained with TUJ1 and MAP2 and counterstained with DAPI under control conditions and when treated with (I–L) PDA-AMSN-D. Scale bar corresponds to 200 µm. ICC of primary neurosphere to check the neurogenic efficiency of PDA-AMSN-D without (I) any treatment and when treated with (J) PDA-AMSN-D neurosphere were stained with MAP2 and GFAP. Scale bar corresponds to 50 µm.

2.4.9 Synthesis, Characterization and Measurement of Injectability Property of PANAP Hydrogel: The peptide with the sequence NAPVSIPQKKK was created in a solid-phase peptide synthesiser (CEM Liberty1, USA) by employing Rink Amide AM resin. Further, palmitic acid (PA) was attached to the peptide (PANAP). It was then purified using reverse-phase HPLC (**Figure 2.23 A**) and lyophilized to produce pure PANAP (**Figure 2.23 B**). Then, we generated the 1wt% PANAP PBS, where

intermolecular hydrogen bonding helps to build a β-sheet-like structure that then self-assembles to form a dense fibre-like network.



Peak#	Ret. Time	Area	Height	Area%
1	2.638	51391	1829	0.105
2	7.470	48823125	2704819	99.753
3	14.519	69618	2240	0.142
Total		48944134	2708889	100.000

Figure 2.23 (A) ESI Mass spectra & (B) HPLC chromatogram of PANAP peptide.

Next, a rheology experiment using 1% (w/v) PANAP hydrogel was conducted to evaluate the hydrogel's mechanical strength. The results of a frequency sweep experiment (conducted at a constant strain of 0.1%), which showed that PANAP hydrogel behaves like a normal hydrogel, indicate that the hydrogel has a larger storage modulus (G′) than loss modulus (G″) and that this difference is significant (**Figure 2.24 A-D**). The values of G′ and G″ showed a weak dependence on angular frequency within the examined range of 1–100 rad/s.

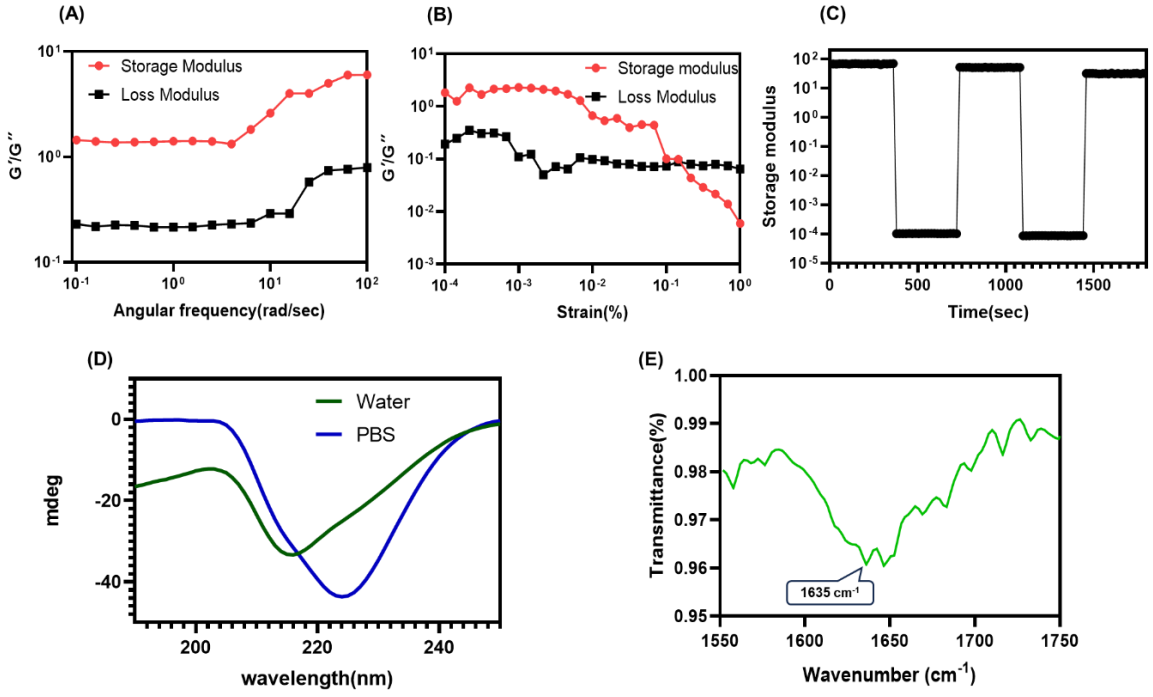


Figure 2.24 Viscoelastic property of PANAP peptide; (A) Frequency sweep study, (B) Strain sweep study, (C) Thixotropic study (D) CD spectra & (E) IR spectra of PANAP peptide.

We then further carried out an FT-IR experiment in order to gain a thorough understanding of the mechanical details of the PANAP hydrogel's self-assembly process. The PANAP hydrogel's amide-I peak, which correlates to the β-sheet

structure, was found at 1635 cm^{-1} (**Figure 2.24 E**). These modifications to the secondary structure make it abundantly evident that the β-sheet structure formed by the PANAP molecules is what causes them to hydrogel. We then examined the PANAP hydrogel's morphology using atomic force microscopy (AFM). Strong interfiber contacts led to the creation of three-dimensional cross-linked dense fibril networks, as shown by AFM (**Figures 2.25 A**). These three-dimensional networks can bind to molecules of drugs or water. Furthermore, we confirm the formation of hydrogel with a vial inversion assay, as shown in the **Figure 2.25 B**, we noticed that the hydrogel had a homogenous character.

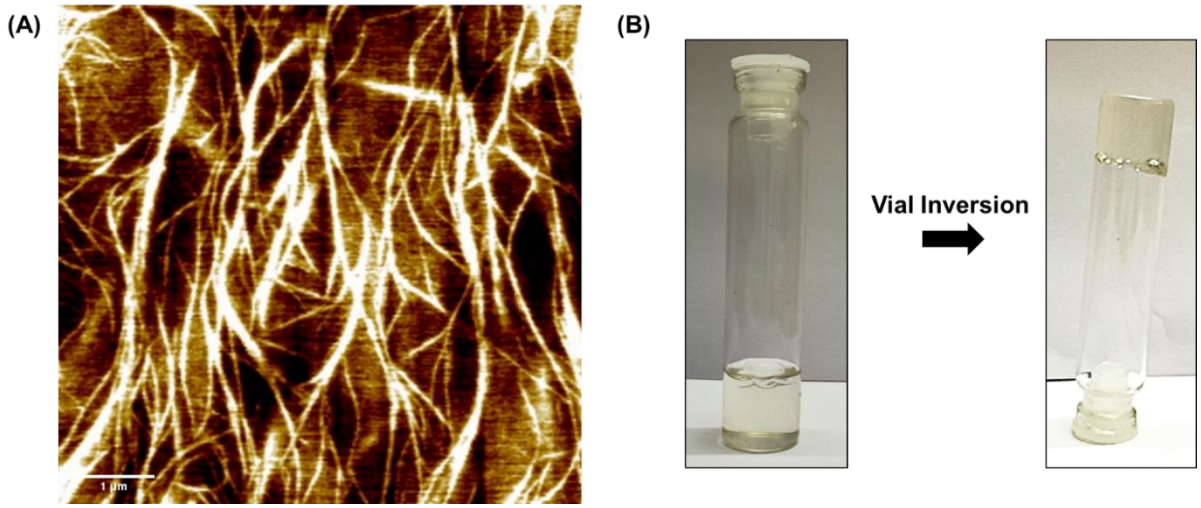


Figure 2.25 Characterization of PANAP hydrogel; (A) AFM of PANAP hydrogel, (B)Vial inversion test to check the formation of hydrogel. Scale bar corresponds to 1 µm.

Because of the injectable nature of peptide hydrogel, it attracts a lot of interest in the medical industry. With the use of a straightforward syringe, injectable hydrogels can be simply administered to the desired region *in vivo* without causing the patient any discomfort during surgery. As a result, we examined the type of hydrogel's practical applicability, or more specifically, its injectability. Using a syringe, the hydrogel's injectable nature was verified. The pictures showed that hydrogel may be taken out of a syringe as a sol and injected through a syringe (**Figure 2.26**). After some time, the sol gradually itself transforms into the gel.

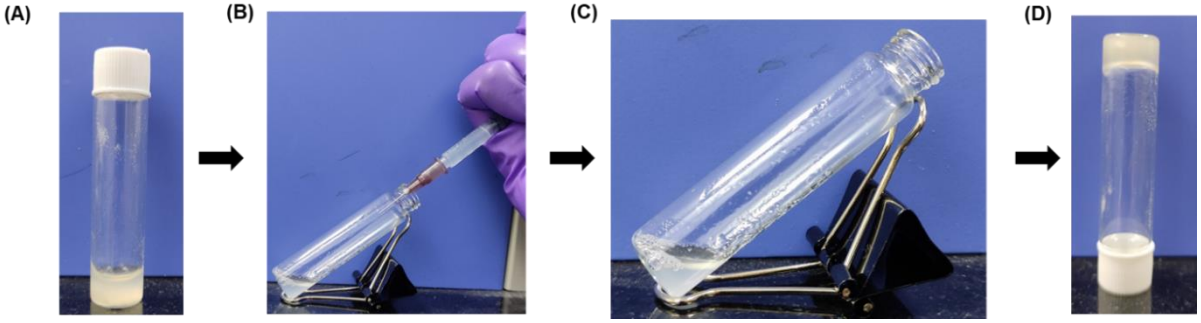


Figure 2.26 Illustration of injectable nature of PANAP hydrogel; (A) PANAP Hydrogel in the vial, (B) Sol" inside injection syringe, (C) "Sol" within the vial, (D) Recovery of "gel" nature within a few minutes as shown with inverted vial**.**

2.4.10 PDA-AMSN-D Mitigates the Pathological lesion on Brain Tissue in Cryogenic Brain Injury (CBI) Rats: The production of free radicals is an inevitable byproduct of metabolic processes and diverse enzymatic activity. In typical physiological conditions, the existence of several antioxidant systems (SOD, CAT, GPx) effectively counteracts the harmful effects of free radicals, therefore minimizing any adverse outcomes. However, the brain is exceptionally susceptible to oxidative stress due to its elevated oxygen demand, weak antioxidant system and the presence of lipid-rich cells, which makes it more prone to peroxidation.[52] The pathophysiological aetiology of TBI is diverse and manifests at multiple levels. TBI leads to several pathological alterations, such as the occurrence of axonal shearing, referred to as diffuse axonal injury (DAI), damage to the neurovascular compartment, neuroinflammation, disruption of neuronal networks, and apoptotic and necrotic cellular damage. The neuroinflammatory response to a TBI is characterized by the release of pro-inflammatory cytokines and the generation of free radicals, which ultimately leads to tissue damage and mitochondrial dysfunction.[40] Oxidative stress is one of the most important factors in generating free radicals, ROS and RNS, and it is characterized by an imbalance between the production of free radicals and their removal in the brain system.[40,53] With advantages in terms of their suitable physiochemical properties, biocompatibility, antioxidative properties, and *in vitro* neuroprotective effects, we subsequently evaluated the *in vivo* neuroprotective effect of PDA-AMSN-D to alleviate the progression of brain injury in rats. For that purpose, the PANAP hydrogel was first doped with PDA-AMSN-D to be used as an injectable therapy.

Firstly, the *in vivo* neuroprotective effect of nanoparticles was accessed by hematoxylin and eosin (H and E) staining and Nissl staining. A comprehensive examination was conducted on the morphology and structural integrity of brain tissue slices following CBI using the HandE staining technique. Regions with a high concentration of proteins, such as the cytoplasm, blood cells, and collagen, exhibited a pink staining pattern. On the contrary, regions that are characterized by a significant presence of nucleic acids demonstrated a blue staining pattern (**Figure 2.27**).[54] Following a mild controlled brain injury, it was observed that the group which received saline as a treatment had evident cortical damage in the region directly underneath the point of impact of the cryogenic cold rod. As shown in Figure 6, 7 days post-injury, there was a significant reduction in dorsal cortical volume in the Gel and Gel / PDA-AMSN-D system treatment group compared to saline treatment (Injury). A close examination of the sham (Control) group region marked with an arrow in the inset clearly shows that the cells are uniformly and densely placed with clear neuronal structure (**Figure 2.27 A-B**). However, the saline treatment group exhibited significant pathological alterations, including a substantial decrease in cellular density, unequal cell distribution, and cytoplasmic vacuolization (**Figure 2.27 C-D**). In the Gel treatment group, there was a gradual decrease in lesion area and an increase in tissue regeneration; however, significant decreases in lesion area, edema and necrosis were found in the affected regions of the brain subjected to the treatment with Gel / PDA-AMSN-D system (**Figure 2.27 E-H**). Also, the amount of tissue regeneration was highest in the Gel / PDA-AMSN-D treatment group. Furthermore, a notable increase

in the quantity of neural cells was seen in the Gel / PDA-AMSN-D system treatment group compared to the saline group.

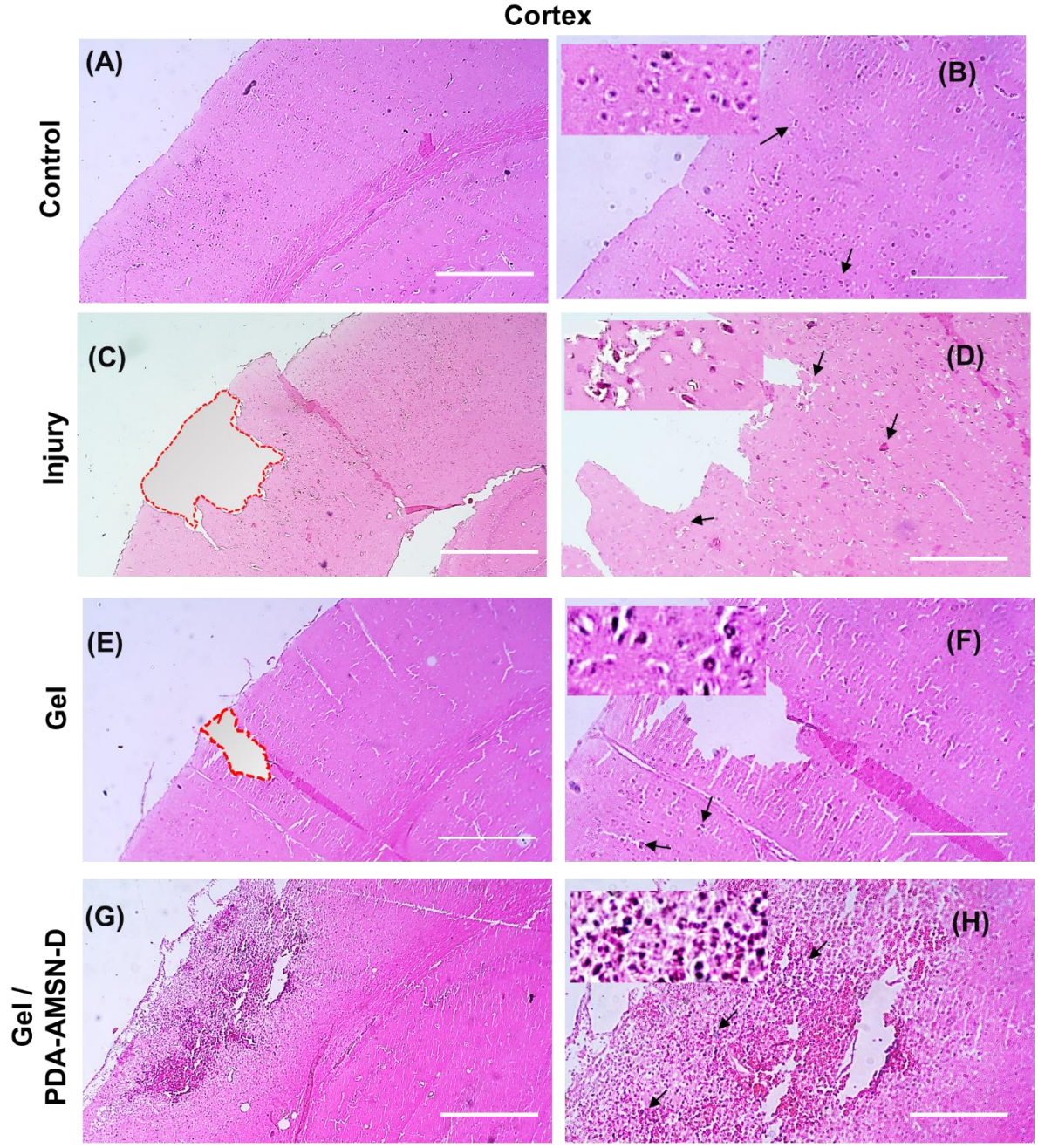


Figure 2.27 PDA-AMSN-D reduces tissue damage and helps in tissue regeneration. (A–H) Hematoxylin and Eosin and Cresyl Violet staining of the cerebral cortex of rat brain sections on day 7 after CBI. (A, B) Densely packed cells in the control group have a clear neuronal structure, as shown in the inset and marked with the black arrow. (C, D) Cytoplasmic vacuolization and uneven distribution of cells in the injured area are shown in the inset and marked with a black arrow. (E, F) Decrease in the injured tissue area when treated with gel as shown in the inset and marked with the black arrow. (G, H) Significant increase in tissue regeneration and a decrease in the injured area, and cell necrosis as compared to the Injury group, as shown in the inset and marked with the black arrow. Scale bar corresponds to 100 µm.

Further brain slices were also stained with Nissl stain. Nissl staining is an effective method for evaluating the degree of neuronal damage due to its remarkable sensitivity. Nissl bodies, which are found in basophilic granules inside neurons, exhibit a tendency to undergo dissolution and reduction in quantity following the occurrence of brain damage.

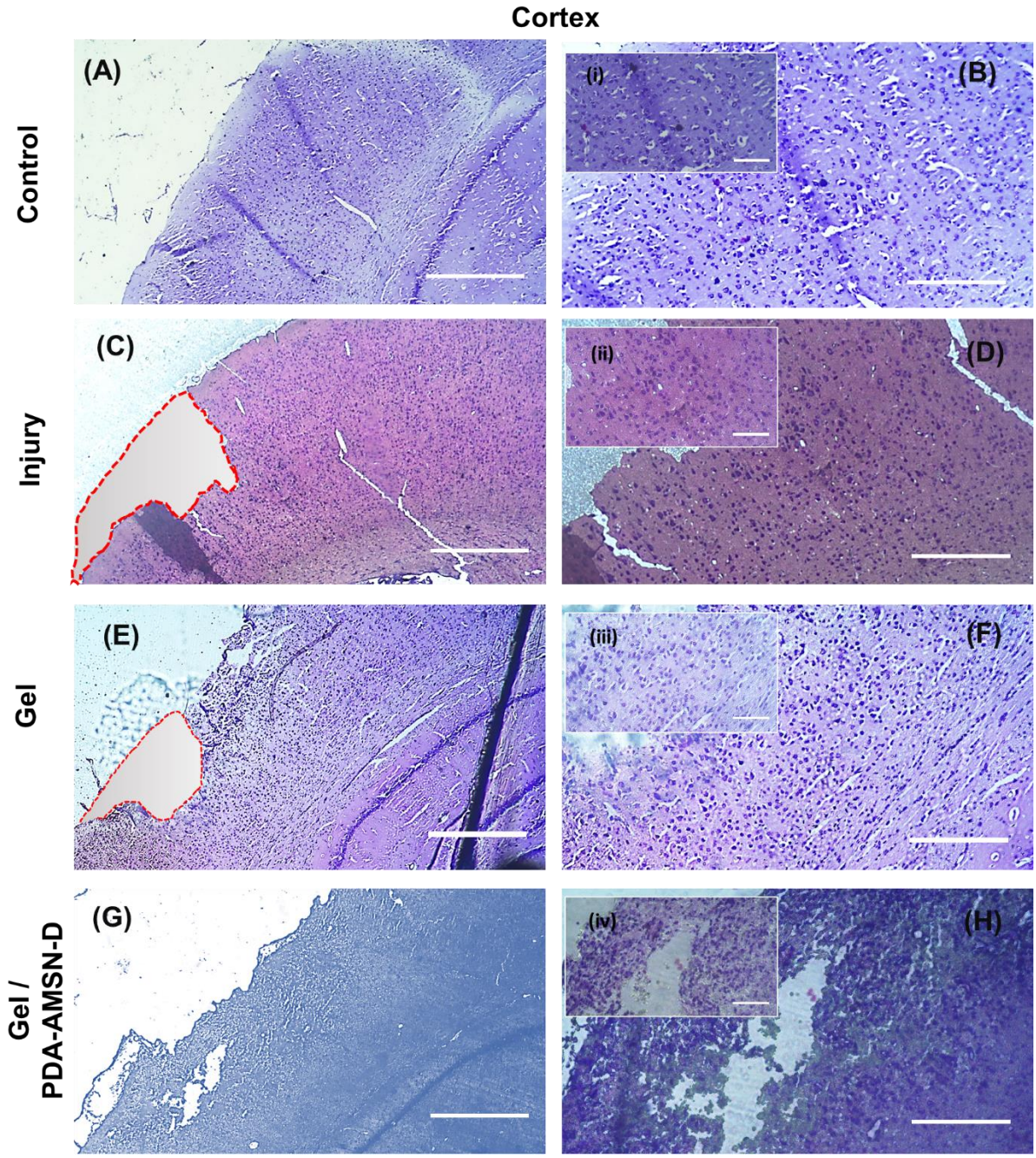


Figure 2.28 PDA-AMSN-D reduces tissue damage and helps in tissue regeneration. Cresyl violent-stained sections of rat cerebral cortex on day 7 after CBI under Control (A, B), Injury (C, D), Gel (E, F), and Gel/PDA-AMSN-D system (G, H). Scale bar corresponds to 100 µm. Scale bar in i–iv corresponds to 50 µm.

As shown in **Figure 2.28 A, B,** the neurons are in healthy morphology. However, as depicted in (**Figure 2.28 C, D**), brain sections stained with cresyl violet revealed loss of Nissl bodies and cortical neurons in the brains of injured rats. In contrast, in the Gel and Gel / PDA-AMSN-D system, a notable reduction in brain necrosis was evident and very minimal tissue lesion was observed in the cortex region after treatment (**Figure 2.28 E-H**). The group that underwent sham treatment showed no observable evidence of cerebral contusion and had a meticulously structured configuration characterized by typical morphology and consistent nuclear staining. We also quantitatively analyzed the lesion volume after the CBI with or without treatment to evaluate and quantify the neuroprotection. Our data showed a significant reduction in lesion volume in the Gel and Gel / PDA-AMSN-D system ($p<0.05$) (**Figure 2.29 A**), suggesting substantial neuroprotection by NPs.

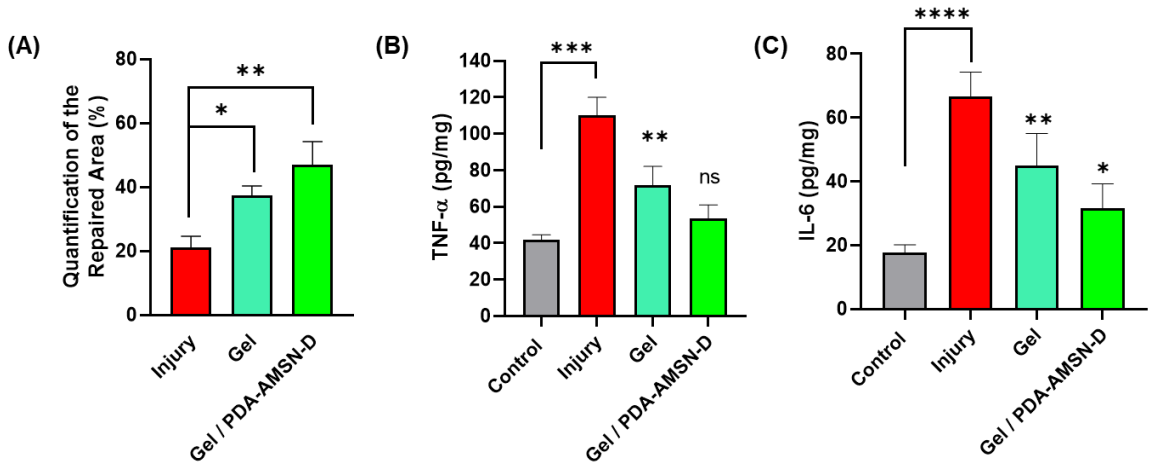


Figure 2.29 Quantification of the repaired area after injury in different group calculated using Image J. (B) Quantification of the expression levels of proinflammatory markers TNF-α and IL-6 in rat brain after CBI with different treatment conditions measured using ELISA technique. Data represent mean ± SD of three independent experiments. The statistical significance of all the results was calculated by using a one-way analysis of variance (ANOVA) with Tukey's post hoc test. *p < 0.05, **p < 0.01, and ****p < 0.0001 in GraphPad Prism.

To investigate the expression of proinflammatory markers in the model rat brain after CBI, we have also checked the expression levels of various proinflammatory cytokine markers like TNF-α and IL-6. As shown in **figure 2.29 B and 2.29 C** the expression level of both the markers were found to be significantly higher in the injury group, which might be due to the secondary injury following CBI. However, compared with the injury group the expression levels of cytokines were significantly lowered in the Gel and Gel / PDA-AMSN-D group. The Gel / PDA-AMSN-D group showed significantly higher neuroprotection by maintaining the levels of both the markers as compared the only Gel group.

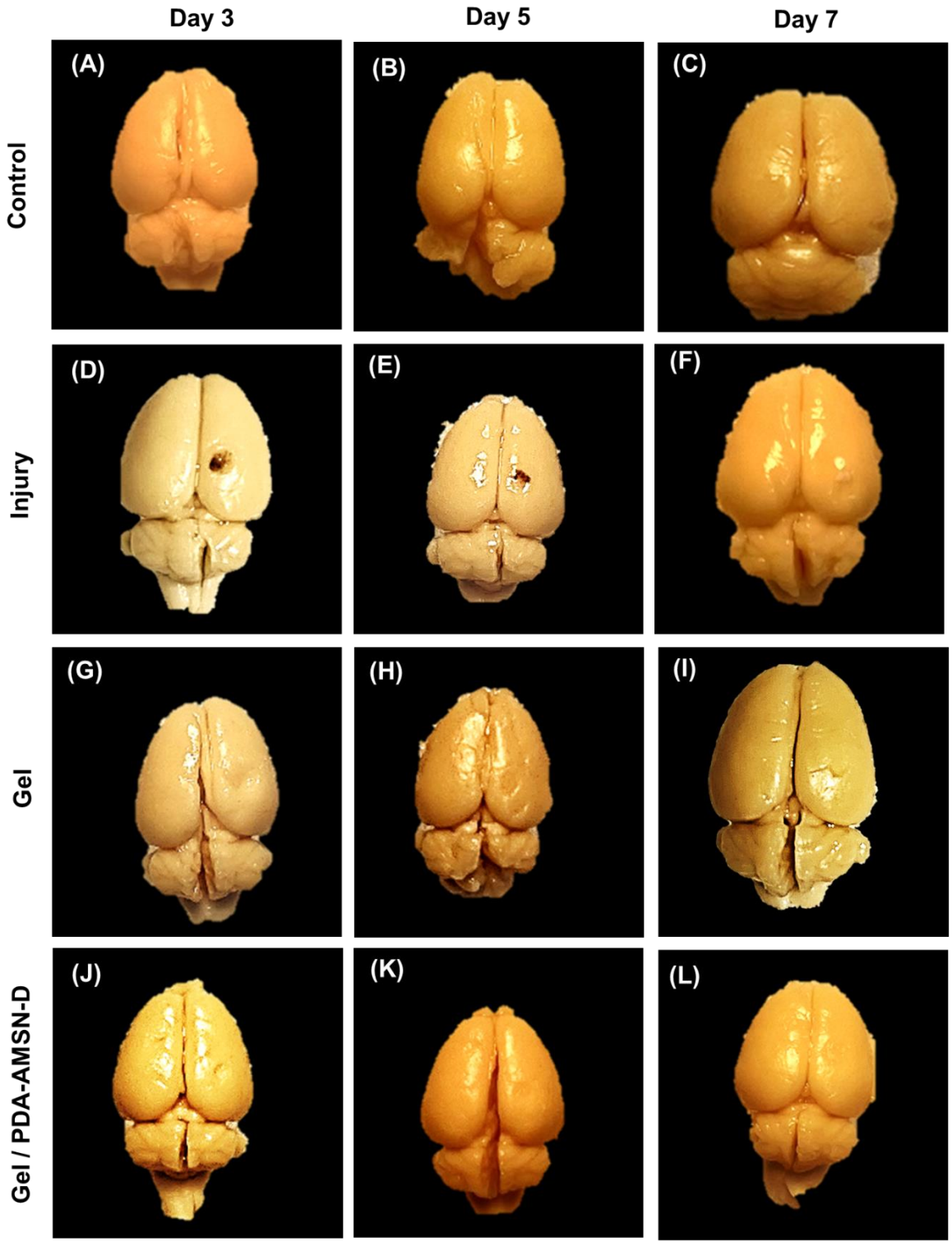


Figure 2.30 Protective effect of PDA-AMSN-D in TBI. (A-C) Representative images of sham rat brain at D3, D5, and D7, respectively. (D-F) Representative images of injured rat brain after saline treatment at D3, D5, and D7, respectively. (G-I) Representative images of injured rat brain that received only Gel as a treatment after injury at D3, D5, and D7, respectively. (J-L) Representative images of injured rat brain that received Gel/PDA-AMSN-D system as a treatment after injury at D3, D5, and D7, respectively.

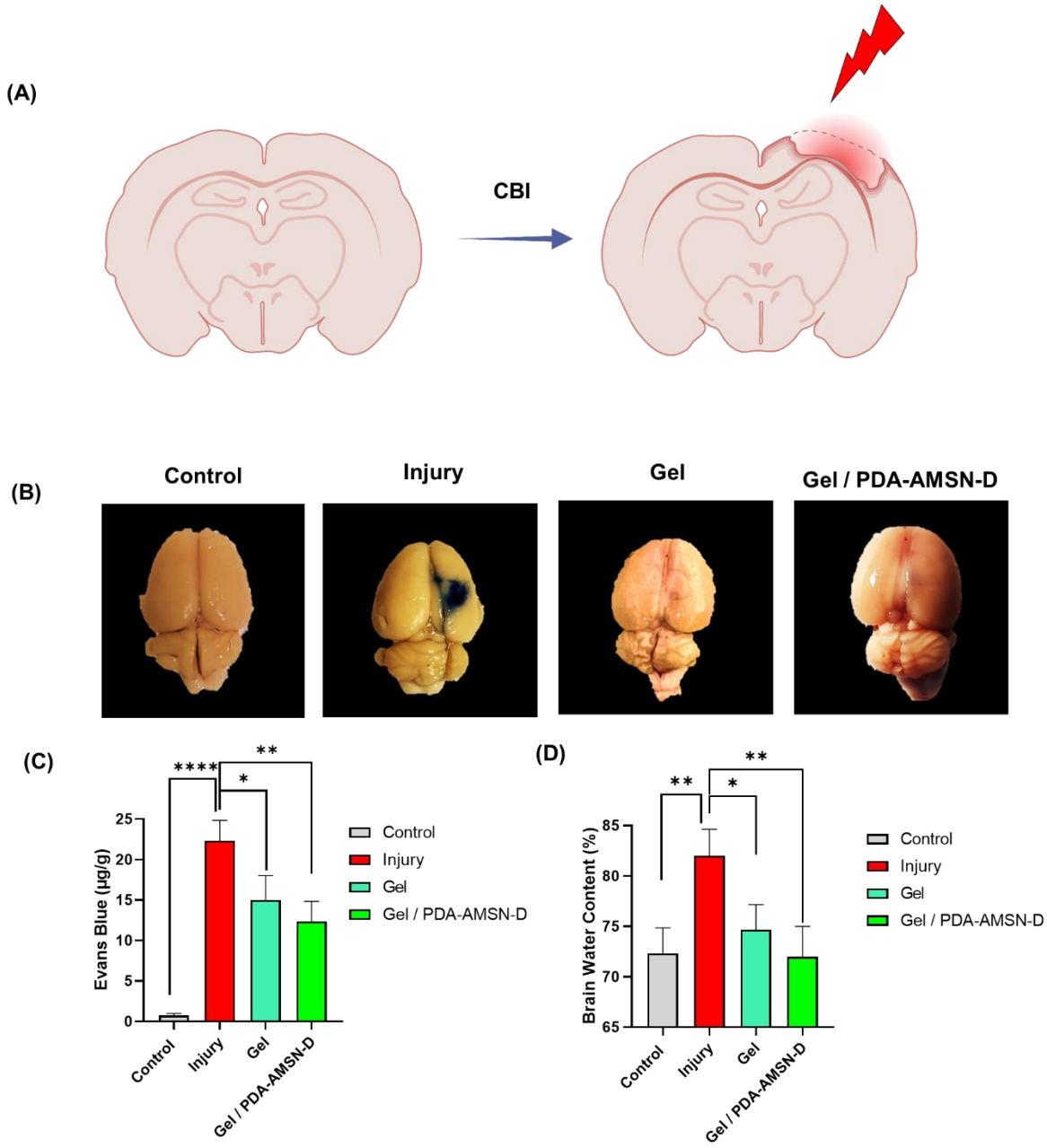


Figure 2.31 Protective effect of PDA-AMSN-D in TBI. (A) Schematic illustration showing the coronal brain section before and after the injury. (B) Evaluation of BBB permeability measured using intravenous injection of EB at day 3 post injury. (C) Quantitative analysis EB leakage in each group (D) Quantitative analysis of Brain edema after post injury. Data represent mean ± SD of three independent experiments. The statistical significance of all the results was calculated by using a one-way analysis of variance (ANOVA) with Tukey's post hoc test. *p < 0.05, **p < 0.01, and ****p < 0.0001 in GraphPad Prism.

Further, as shown in **Figure 2.30**, images exhibited visual representations of brain injuries subjected to various treatment groups for 7 days. As expected, no lesion was observed in the sham group (**Figure 2.30 A-C**). Although, as seen in the images, the circular void resulting from the presence of the copper rod in the saline treatment group (**Figure 2.30 D-F**) exhibited the greatest extent of injury, there was a notable presence of blood stasis in the injury group as well. However, there was no noticeable blood stasis in the group treated with the Gel / PDA-AMSN-D system despite the presence of non-significant abnormalities. Both the groups treated with Gel and Gel /

PDA-AMSN-D system exhibited a decrease in brain tissue defects (**Figure 2.30 G-I**). Nevertheless, significant recovery was observed in the Gel / PDA-AMSN-D system treatment group, and there was no observable damage by the end of the 7th day (**Figure 2.30 J-L**). Hence, it is noteworthy to mention that the Gel / PDA-AMSN-D system had the lowest volume of edema surrounding the lesion, suggesting that the application of the Gel / PDA-AMSN-D system can effectively mitigate the extent of brain tissue injury following CBI.

2.4.11 Effect of the PDA-AMSN-D on BBB Permeability and Brain Edema after Brain Injury: The comprehensive disruption of the BBB and the subsequent occurrence of brain edema contribute to the exacerbation of adverse consequences associated with brain injury. According to prior research findings, secondary injury in TBI conditions has resulted in a range of repercussions, including cellular apoptosis, enhanced permeability of endothelial cells, and the disintegration of tight and intercellular junction proteins. Disruption in BBB is a recognized pathophysiological characteristic of severe TBI and is closely linked to neuroinflammatory processes (**Figure 2.31 A**).[55] The Gel / PDA-AMSN-D system has demonstrated the capacity to mitigate the extent of BBB damage and alleviate cerebral edema. Consequently, in a separate study, we assessed BBB permeability through Evans Blue (EB) staining. As illustrated in **Figure 2.31 B**, when compared to the saline treatment group, both the Gel / PDA-AMSN-D system and the Gel group notably diminished the extent of EB penetration and the EB content within the brains of CBI rats. As shown in **Figure 2.31 C**, we observed a significantly greater extravasation of i.v. EB dye into the brains of saline-treated rat, as compared to the brains of the Gel and Gel / PDA-AMSN-D system-treated group. These results demonstrated that Gel / PDA-AMSN-D system could protect BBB integrity in CBI rat. Further, brain edema was also assessed in each group by quantifying the brain water content three days post-treatment **Figure 2.31 D**. The findings obtained were in accordance with the observations made using EB staining and visual representation of the brain. The water content of the Gel group exhibited a statistically significant reduction ($p < 0.01$). The observed reduction in the Gel / PDA-AMSN-D system was quite pronounced and essentially reached a level comparable to that of the injury and Gel group ($p > 0.05$).

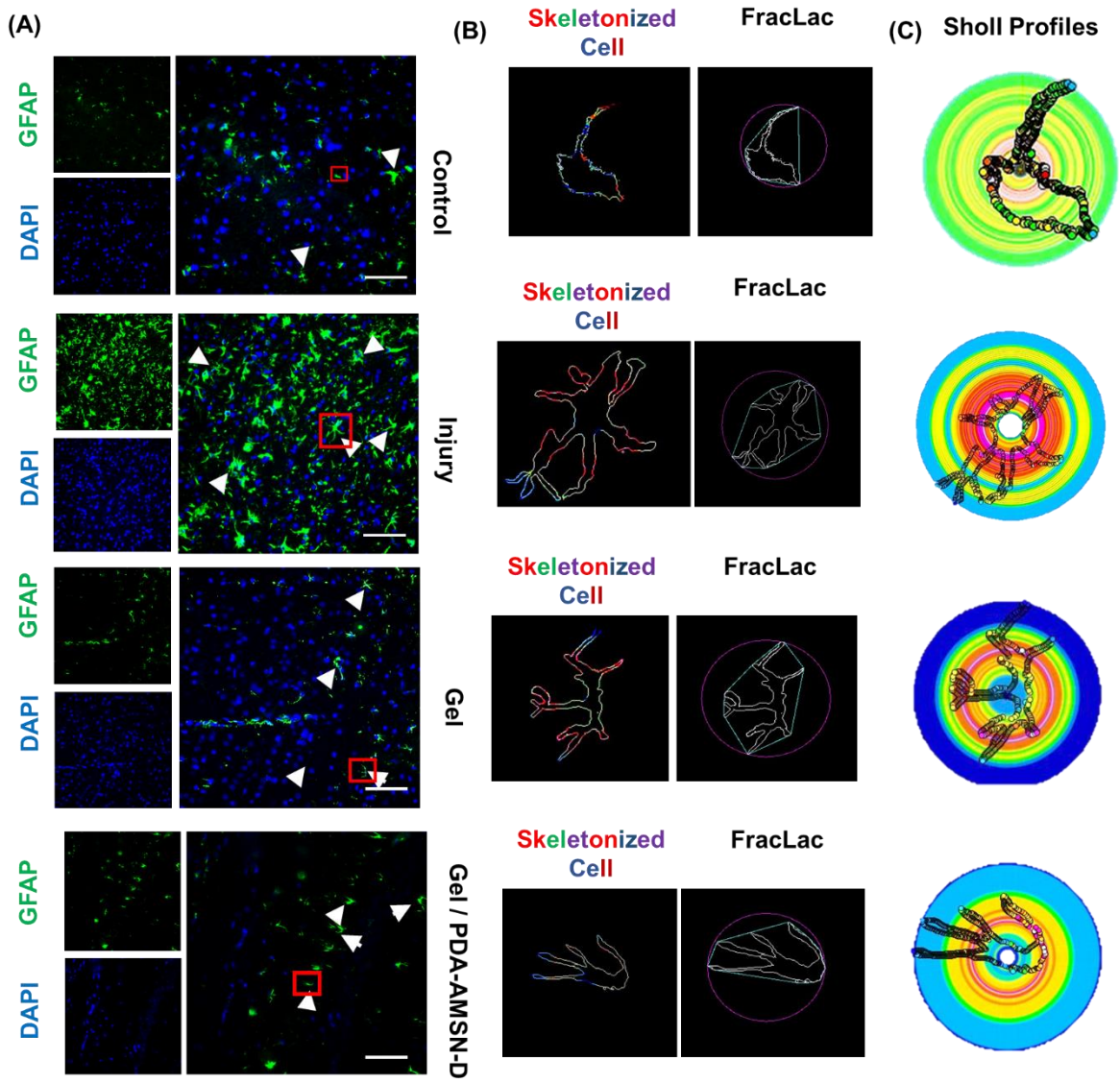


Figure 2.32 PDA-AMSN-D attenuated oxidative, inflammatory response in CBI and promotes neurological functional recovery. (A) Fluorescent images of GFAP-stained cortex and straitum section of Control, Injury, Gel, and Gel/PDA-AMSN-D system brain 7 days after CBI. Highly branched, highly reactive astrocytes are marked with white arrow. (B) Schematic illustration of a single skeletonized microglia with annotations points and its FracLac analysis output. (C) For Sholl analysis, circles show overlaid spheres centered around microglia somata. Scale bar corresponds 50 µm.

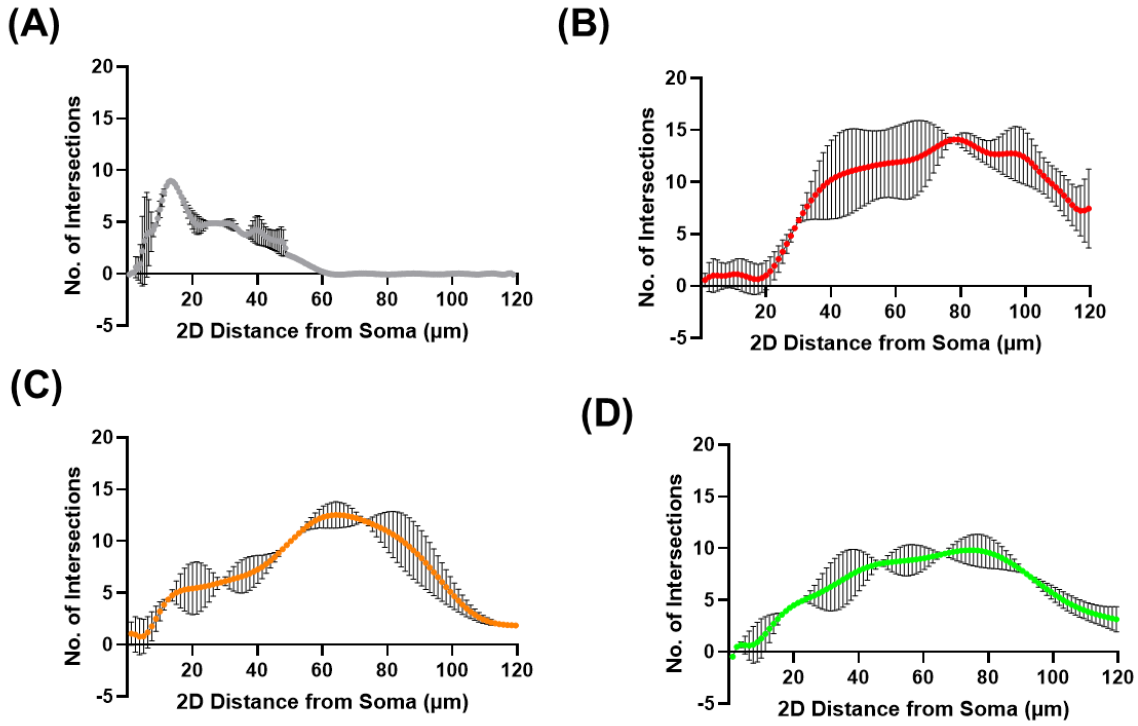


Figure 2.33 Quantification of GFAP stained astrocytes complexity using Sholl analysis of GFAP-stained ipsilateral cortex section of (A) Control, (B) Injury, (C) Gel, and (D) Gel/PDA-AMSN-D system brain 7 days after CBI.

2.4.12 Treatment with PDA-AMSN-D System Effectively Reduces Neuroinflammation and Neuronal Death after CBI: It is evident that the loss of neuronal cells, activation of reactive astrocytes and the activation of glial cells represent significant pathophysiological characteristics in brain injury. Neuronal apoptosis stands as the primary contributor to neurological impairment subsequent to brain injury.[56] The prognosis of TBI is predominantly shaped by the inflammatory response that occurs following the damage. The buildup of ROS within brain tissue gives rise to a detrimental microenvironment in which several inflammatory agents can trigger the death of nerve cells through necrosis and apoptosis.[57] Effective mitigation of ROS levels at the location of cerebral trauma has emerged as a crucial determinant influencing the outcome of subsequent brain damage. Moreover, the activation of astrocytes and microglia is a common immune response aimed at preventing pathological processes in healthy tissues. However, when astrocytes become over-reactive and microglia are activated, they can release excessive amounts of neurotoxic and pro-inflammatory mediators, including reactive oxygen and nitrogen species (RONS). These mediators are believed to play a role in the development of neurodegenerative diseases. The upregulation of ionized calcium binding adaptor molecule 1 (Iba-1) was seen in microglial cells upon activation and the surge in glial fibrillary acidic protein (GFAP) is a distinctive cellular response seen by astrocytes in the event of significant brain injury. In this context, the inhibition of microglia-mediated inflammation and the mitigation of oxidative stress have been recognized as effective strategies to attenuate neuronal necrosis.

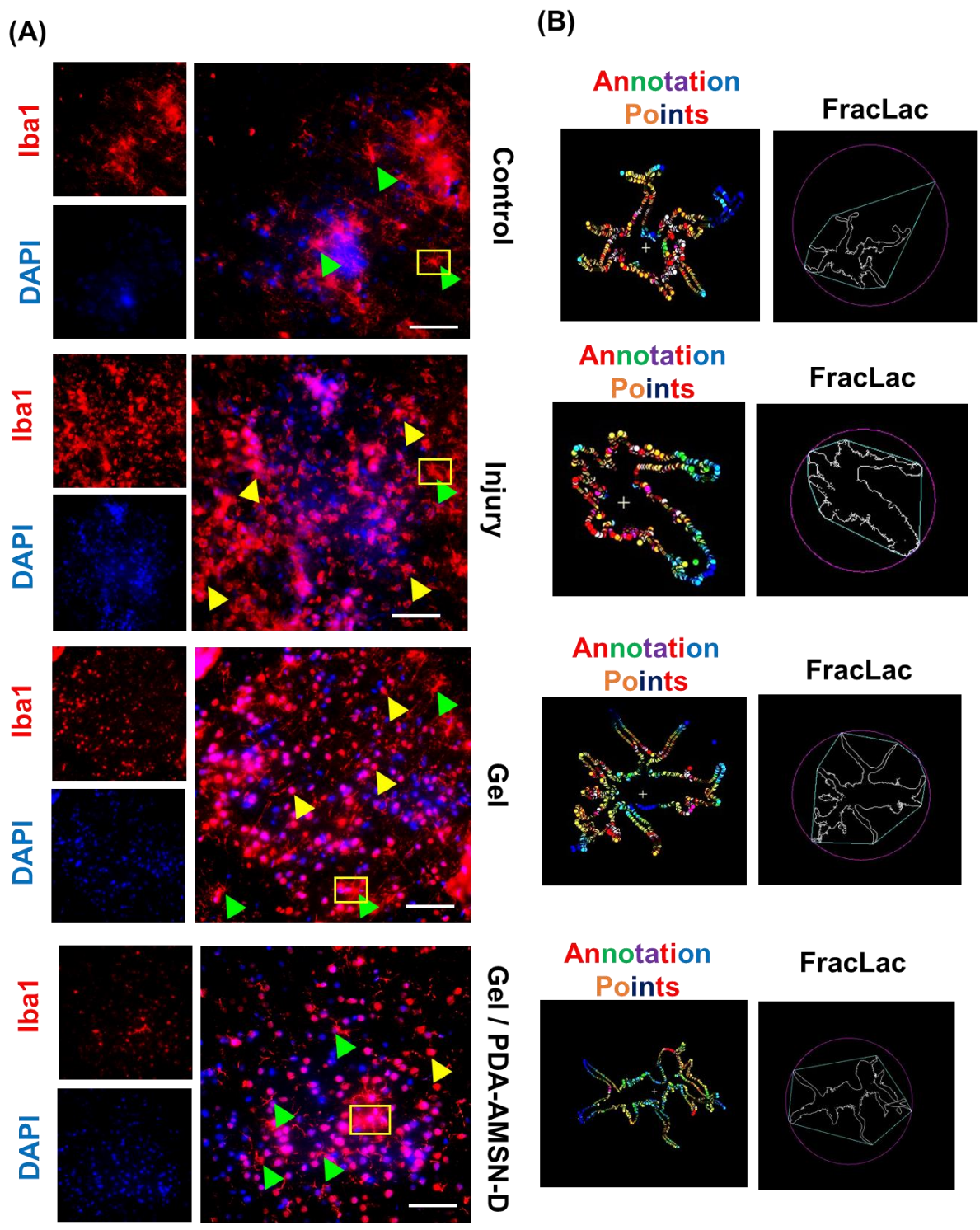


Figure 2.34 (A) Fluorescent images of Iba1-stained ipsilateral cortex section of Control, Injury, Gel, and Gel/PDA-AMSN-D system brain 7 days after CBI. Highly branched, highly ramified microglia are marked with green arrow, and deramified amoeboid microglia are marked with yellow arrow. (B) Schematic illustration of a single skeletonized microglia with annotations points and its FracLac analysis output. Scale bar corresponds to 50 μm.

Therefore, immunohistochemistry was employed to quantify the expression levels of GFAP and Iba-1 at the end of 7 days in order to evaluate the temporal variations in inflammation levels following treatment in CBI rat.

Furthermore, one straightforward approach to assess potential alterations in astrocytes and microglia classification/activation is analyzing their traces by comparing raw morphometric data acquired from various experimental groups. Cell soma, cell volume, ramification indicated by sholl analysis (proximal and distal processes to the cell), number of terminal points, total length of all processes, and territorial coverage of the cells are some of the most prevalent metrics of astrocytes and microglia to analyze[58]. When these characteristics are combined, they give a more complete understanding of these cells in the relative environment. A Sholl analysis was conducted on sections stained with GFAP and Iba1 to measure the quantity of intersections between astrocytes and microglial processes, relative to the radial distance from each individual cell soma inside the molecular layer of the cortex [59].

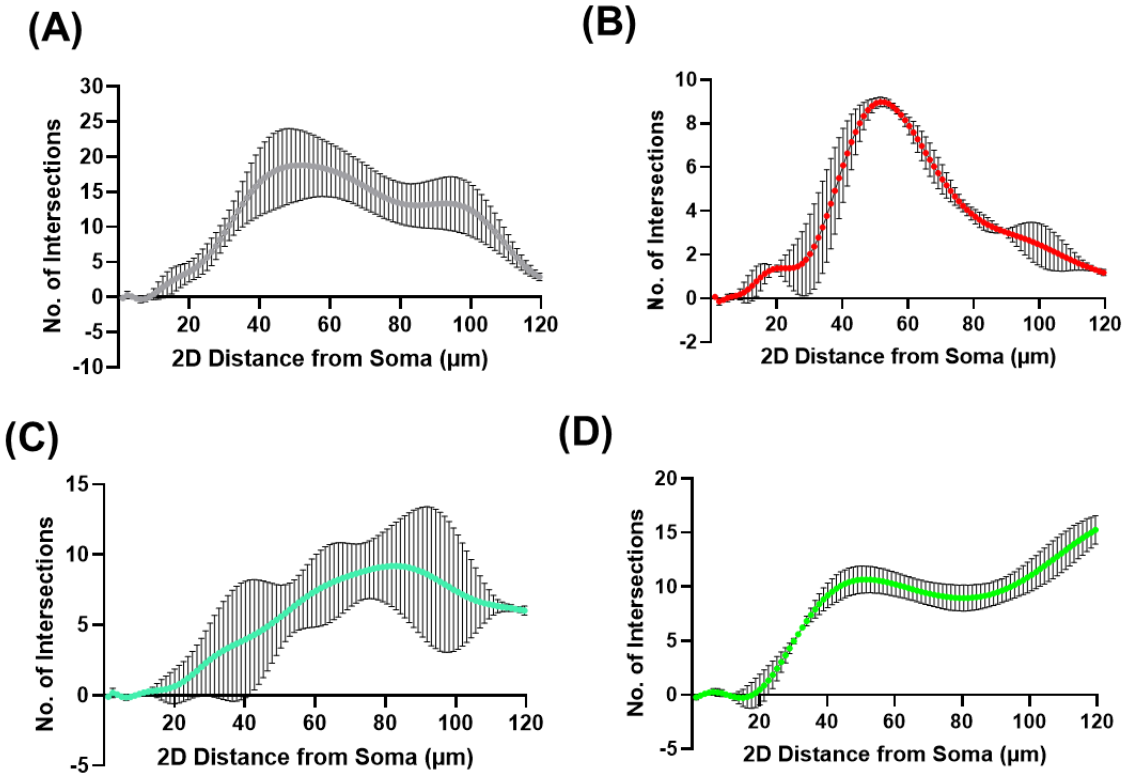


Figure 2.35 Quantification of microglial dendrite ramification complexity using Sholl analysis of Iba1-stained ipsilateral cortex section of (A) Control, (B) Injury, (C) Gel, and (D) Gel/PDA-AMSN-D system brain 7 days after CBI.

In *in vivo* conditions, the activation of astrocytes is concomitant with a discernible alteration in morphology, wherein astrocytes in an activated state undergo a shift from a less branching form to a highly branched morphology. Upon comprehensive analysis of the complete dendritic tree, encompassing both the apical and basal regions, it was observed that in the injury group, cortex astrocytes exhibited a higher number of intersections, indicating a greater occurrence of dendritic bifurcations,

compared to the treatment group of Gel / PDA-AMSN-D. This disparity was evident across all radii ranging from 20 to 120 µm (**Figure 2.32 A-C and Figure 2.33 A-D**).

The number of processes and sum of intersections were used to quantify the glia morphometric properties using sholl analysis to determine the number of intersections at 2 µm radial intervals starting from the soma's central point, which served as a gauge for the intricacy of the glial cells' ramifications and branches (**Figure 2.34 A, B**). The mean peak number of sholl intersections was reached with a broad peak ranging from 40-100 µm distance from the soma for the sham group, while for the injury group, it was quite low with sharp single peak at around 50 µm. Interestingly, we found significantly different mean peak number and broader peaks for both the groups Gel and Gel / PDA-AMSN-D (80 µm and 110 µm), which seem to have lowered down after treatment with Gel and Gel / PDA-AMSN-D systems, respectively **Figure 2.35 A-D**.

The immunostained section of the hippocampus shows a significant difference in the expression of GFAP in different treatment conditions (**Figure 2.36**). Interestingly, the results shown in **Figure 2.37 A, B** demonstrate a higher expression of GFAP-positive cells and IBA1-positive in the saline treatment group compared to the control group in the striatum region. This finding suggests a notable activation of microglia and astrocytes following injury. Overall, our findings indicate that Gel / PDA-AMSN-D system exhibited a more potent protective effect against stress-induced glia activation when compared to gel. The pan-neuronal marker, NeuN, was also employed to measure the neuronal population within the regions affected by the injury. As seen in **Figure 2.38**, a significant reduction in NeuN-positive cells was observed in the rats who received only saline as a treatment, suggesting the occurrence of neuronal loss subsequent to injury. The administration of Gel / PDA-AMSN-D system resulted in a decrease in astrocyte and microglia activation in both cortex and striatum regions. This was evidenced by a reduction in cell size an increase in cell number and fraction for GFAP-positive (**Figure 2.39 A**) cells and IBA1-positive (**Figure 2.39 B**). In contrast, the administration of only Gel did have the same effect, but the Gel / PDA-AMSN-D system has a significantly superior protective effect. However, our results provide compelling evidence that PDA-AMSN-D effectively attenuated the decrease in neuronal count (**Figure 2.39 C**).

This was corroborated by quantifying NeuN+/DAPI+ cells within both the cortex and striatum of the rat subjected to CBI. In contrast, the group that received only Gel as a treatment did not exhibit a noticeable increase in NeuN-positive cells as compared to PDA-AMSN-D. The results demonstrated that PDA-AMSN-D had a greater ability to protect against neuronal death when compared to Gel. In summary, combination of PDA-AMSN-NPs and gel significantly and consistently reduces the hyperplasia and hypertrophy of astrocytes and microglia in the injured lesion which significantly maintain cell homeostasis, and thereby ameliorates neuroinflammation induced by brain injury.

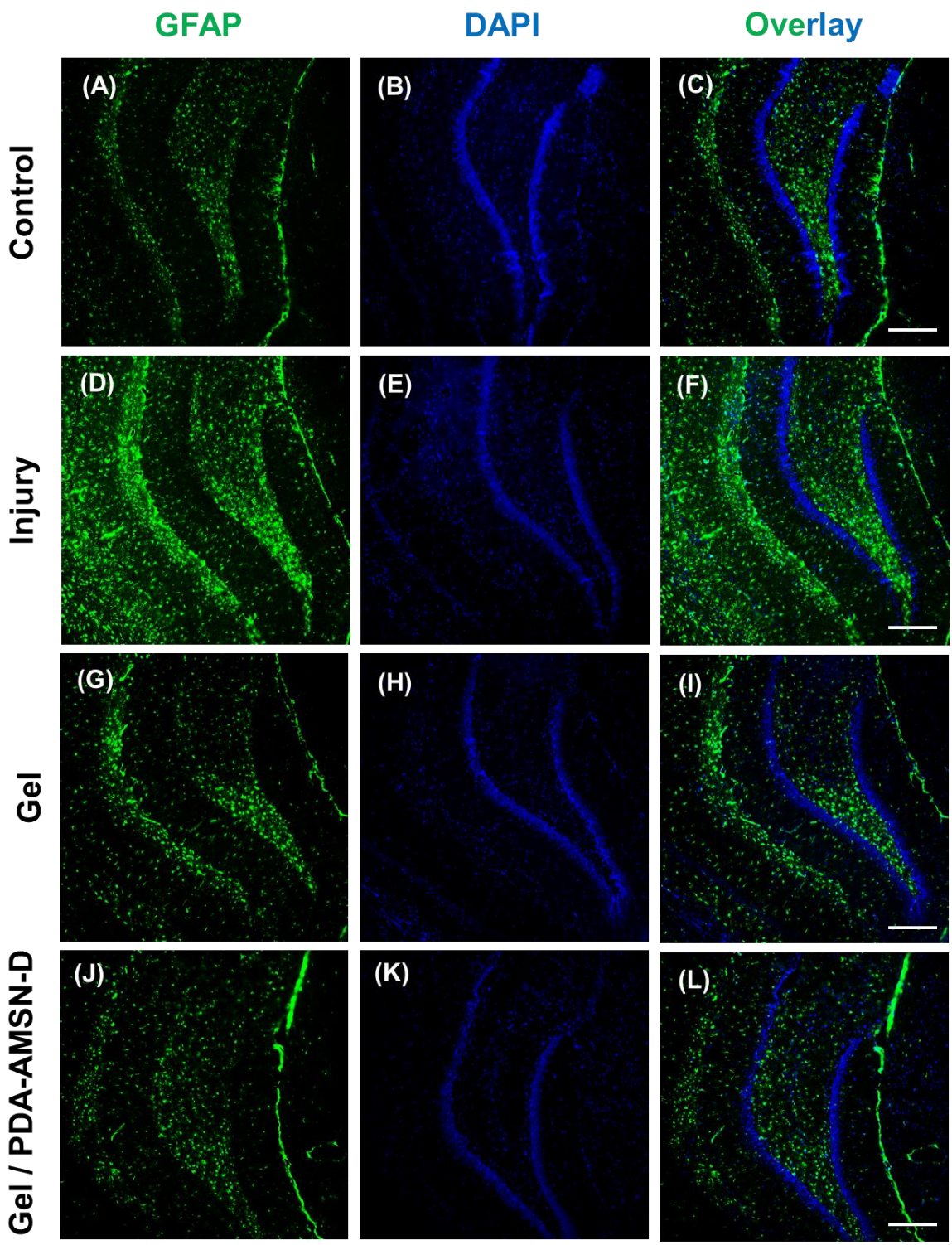


Figure 2.36 Increased GFAP astrocytes expression in the ipsilateral section of the hippocampus after CBI. (A-C) Representative images of GFAP immunostaining in the Control, (D-F) Representative images of GFAP immunostaining in the Injury, (G-I) Representative images of GFAP immunostaining in the Gel and (J-L) Representative images of GFAP immunostaining in the Gel / PDA-AMSN-D hippocampus region of brain. Counter stained with DAPI. Scale bar corresponds 200 μm.

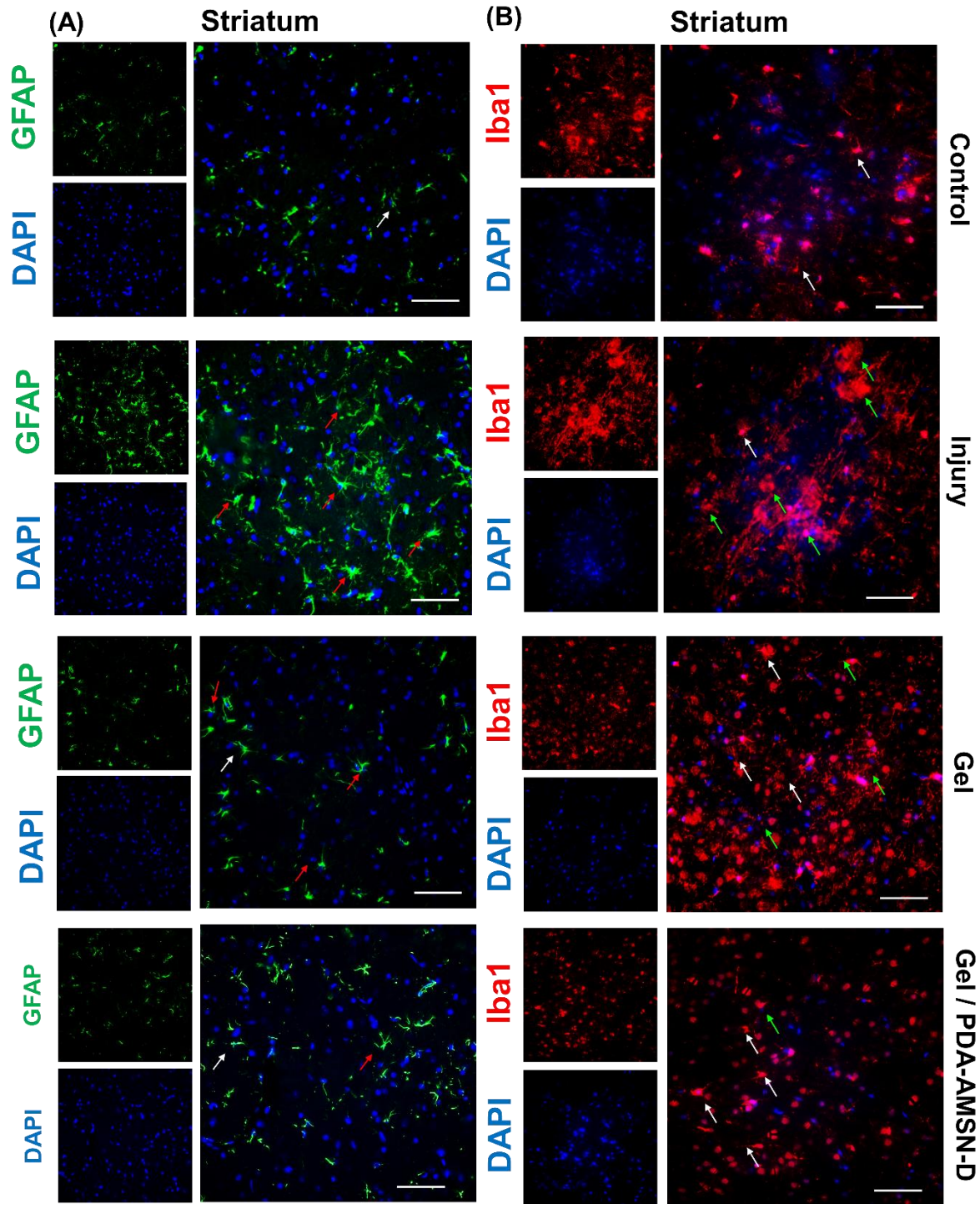


Figure 2.37 PDA-AMSN-D attenuated oxidative, inflammatory response in CBI and promotes neurological functional recovery. (A) Fluorescent images of GFAP-stained straitum section of Control, Injury, Gel, and Gel/PDA-AMSN-D system brain 7 days after CBI. Highly branched, highly reactive astrocytes are marked with white arrow. (B) Fluorescent images of Iba1-stained straitum section of Control, Injury, Gel, and Gel/PDA-AMSN-D system brain 7 days after CBI. Scale bar corresponds 50 μm.

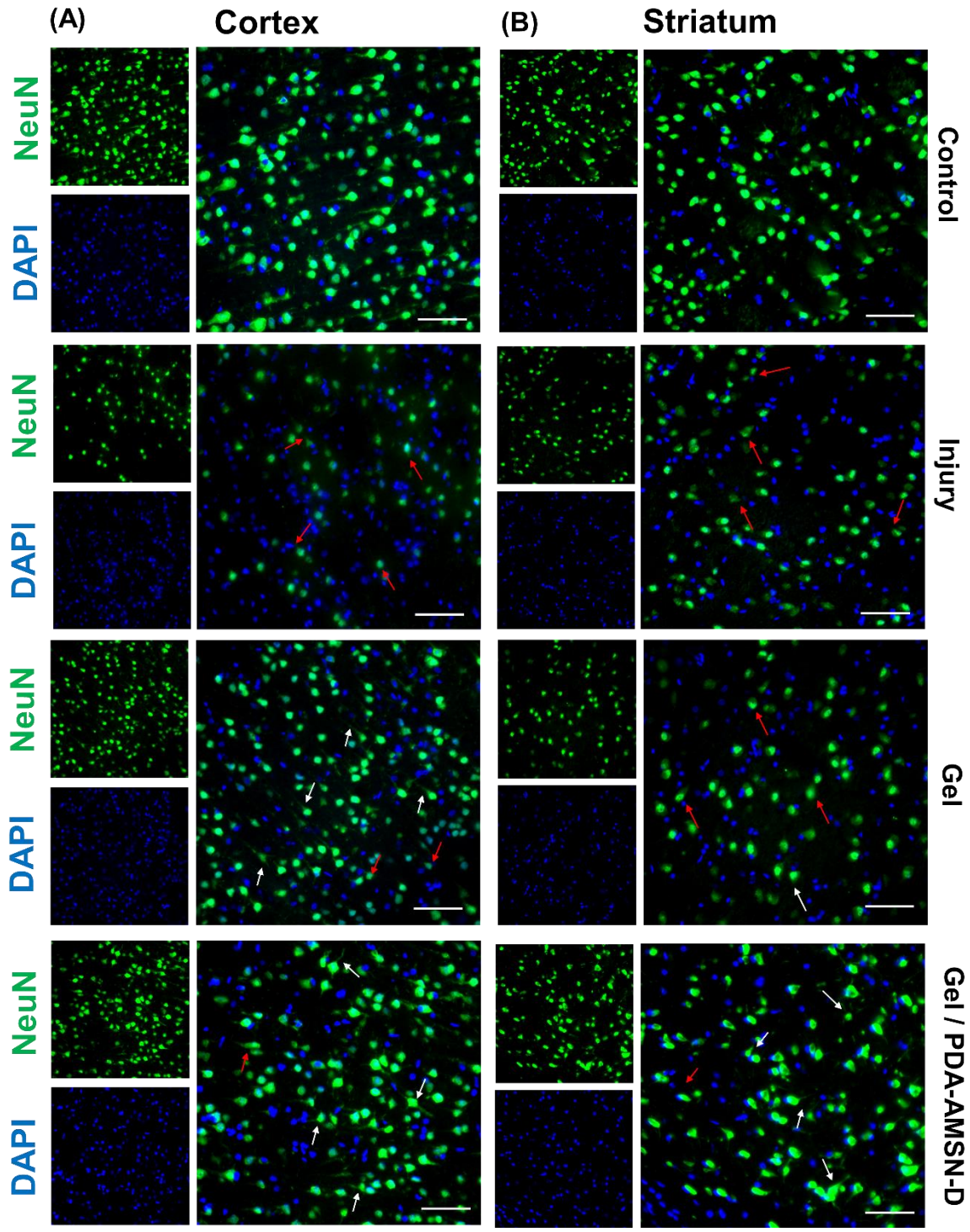


Figure 2.38 Fluorescent images of NeuN-stained (A) cortex and (B) straitum section of Control, Injury, Gel, and Gel/PDA-AMSN-D system brain 7 days after CBI. Neurons with injury and retracted neurite length are marked with red arrow. Neurons with injury and retracted neurite length are marked with red arrow. Scale bar corresponds 50 μm.

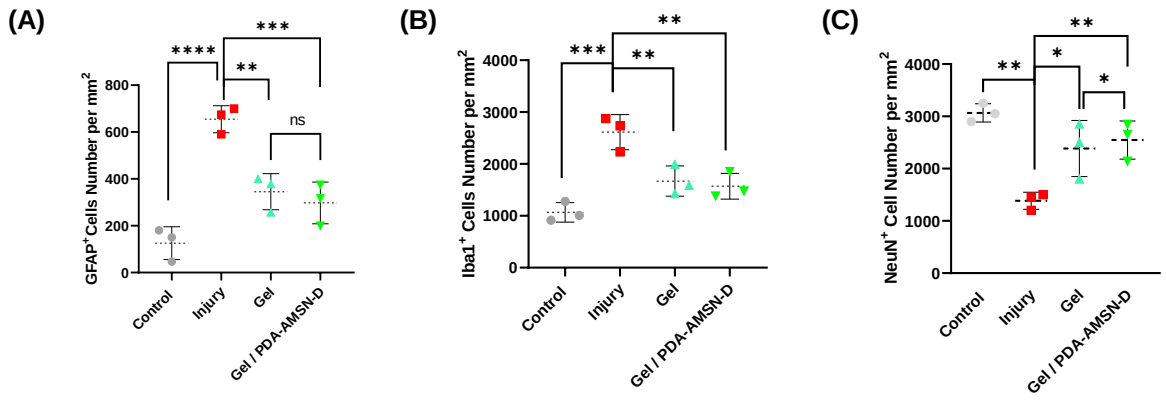


Figure 2.39 (A), (B) and (C) Quantification of astrocytes, microglia & NeuN in the cortex region. Data are represented as the mean ± s.d. from three independent images. Significances are marked as *P < 0.05, **P < 0.01, and ***P < 0.001; one-way analysis of variance (ANOVA).

2.4.13 PDA-AMSN-D NPs facilitate the recovery of neurological function following TBI: Given the evidence that the brain lesion typically triggers systemic immune-inflammatory responses, which leads to the disruption of the BBB, resulting in significant astrogliosis and neuronal cell death, it is obvious that these factors also play a role in the deterioration of cognitive performance and motor function.[56] The Morris water maze (MWM) stands as a classic behavioural experiment employed to investigate long-term learning and memory in rats. In this study, we performed behavioural tests to assess spatial navigation and reference memory over a period of 5 days (**Figure 2.40 A**). As seen in **Figure 2.40 A**, each group of rats were trained and learned for spanning a duration of 5 days. Throughout this period, the time required to reach the platform (referred to as searching time) was evaluated. Interestingly, the group treated with PDA-AMSN-D had the most prominent enhancement, suggesting that these rats exhibited the highest level of recovery in terms of spatial learning capacity subsequent to the treatment (**Figure 2.40 B**).

Following the completion of the learning phase, the rats also underwent a testing procedure in which the platform was removed to evaluate their capacity for memory retention. The experimental findings indicated that the rat belonging to the Gel / PDA-AMSN-D system had the ability to recall the precise position of the platform. In contrast, the injury group and the Gel group exhibited more chaotic swimming tracks (**Figure 2.40 B**). Besides, the group treated with the Gel / PDA-AMNS-D system had the lowest swimming distance required to reach the first platform (**Figure 2.41A, B**). Moreover, in the evaluation of criteria such as time spent in the target quadrant and the frequency of traversing the platform area inside the target quadrant, the Gel / PDA-AMSN-D system exhibited the most advantageous results when compared to the other groups (**Figure 2.41 C-E**).

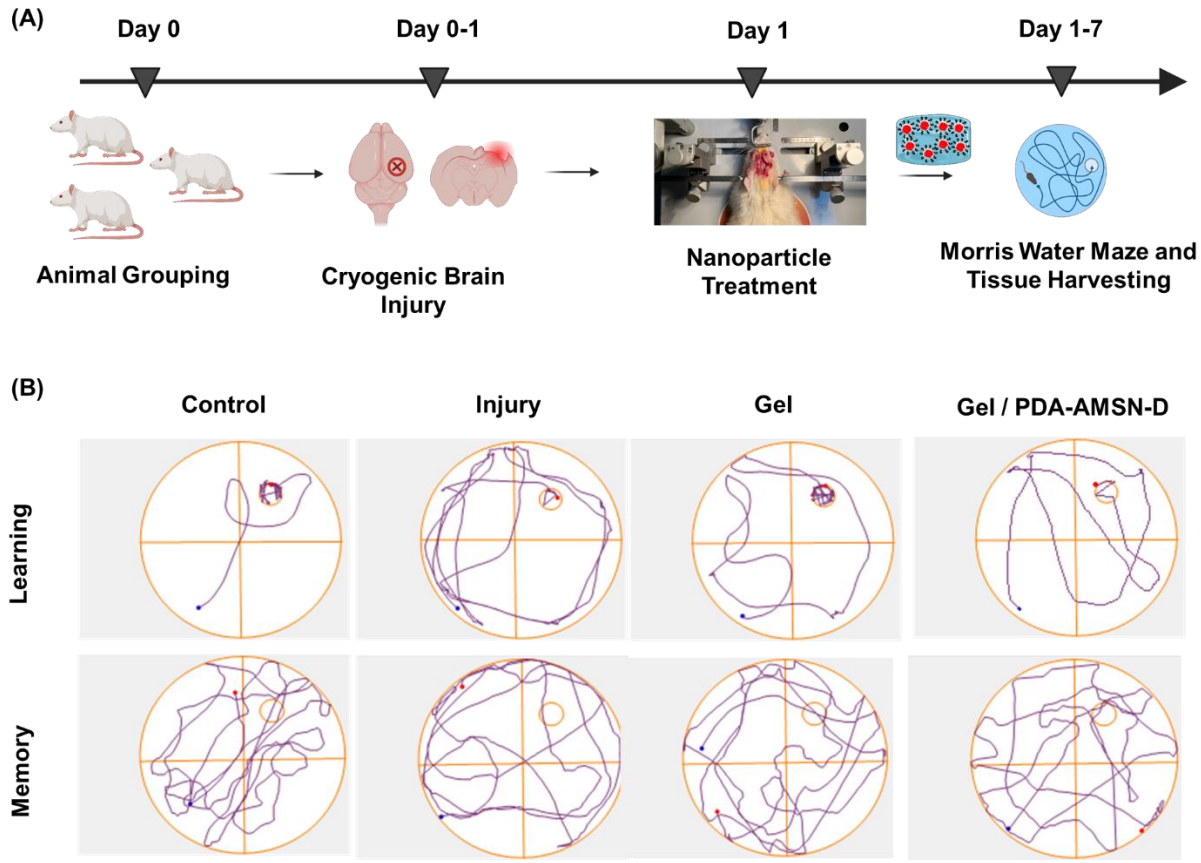


Figure 2.40 MWM behavioral set up for the CBI rats (A) A timeline illustration of the CBI from day 0 of animal grouping to day 7. (B) Representative images of track plots of animals during learning and memory phase.

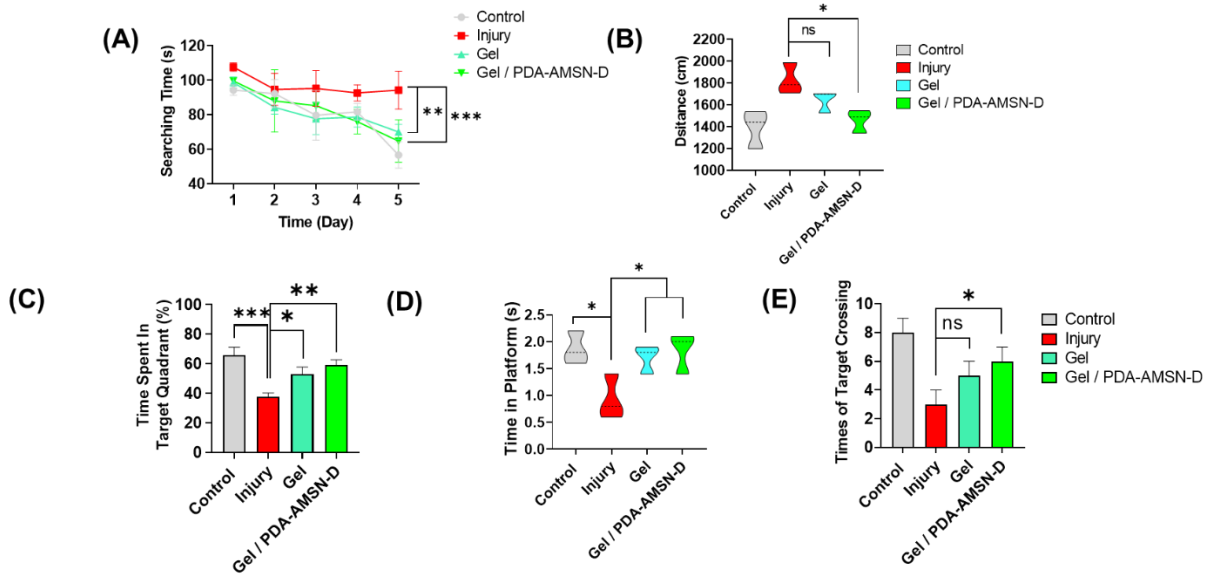


Figure 2.41(A) Searching time of the platform for each day during the last trial for 5 days. (B–E) Distance to the platform, time spent in target quadrant during the learning phase, time spent at the platform, and number of times platform crossing during the probe trial. Data are represented as the mean ± s.d. from three independent experiments. Significances are marked as *P < 0.05, **P < 0.01, and ***P < 0.001; one-way analysis of variance (ANOVA).

2.5 Conclusion

Although conventional systemic drug therapy is commonly employed in clinics, it is accompanied by significant limitations that impede its efficacy in combating the problem of excessive ROS in TBI (Scheme 2). Nanotechnology provides a hopeful answer by facilitating the creation of medication delivery devices that can efficiently cross the BBB and directly administer therapeutic medicines to damaged areas of the brain. Nanotechnology can also effectively mitigate off-target effects and minimize potential adverse effects of conventional pharmaceutical therapies by precisely targeting sites of inflammation. Moreover, the accurate administration of therapeutic substances to affected areas can potentially result in increased effectiveness and enhanced patient outcomes in the management of neurological illnesses.

Hence, to this end in this study, we designed an antioxidative Gel / PDA-AMSN-D system by combining the antioxidase mimicking PDA-AMSNs with neuroprotective injectable hydrogel (PANAP) for TBI, in which the effective anti-inflammatory component PDA-AMSN NPs were also loaded with a neurogenic small molecule (NCM) for the effective neurogenesis at the lesion site. The antioxidative PDA-AMSN effectively ameroliate mitochondria dysfunction, rescues neuroblastoma cells from apoptotic cell death *in vitro*, dramatically reduces the formation of the glial scar, neuroinflammation, loss of neurons, reverses BBB senescence and rescues memory deficit. This Gel / PDA-AMSN-D acts as an AND logic gate where both PDA-AMSN and NCM collectively mitigate the injury outcome and help in functional recovery.

Overall, this new pharmaceutical delivery system reduced inflammation, enhanced neurogenesis, and improved cognitive function in TBI, suggesting clinical relevance in other oxidative stress-related CNS injuries. Hence, additional research is required to determine the most appropriate dosage and assess the long-term effectiveness and safety of this system in clinical trials for treating TBI. To the best of our knowledge, we have presented for the first time the promising potential of ROS-scavenging PDA-AMSN in the treatment of TBI. Overall, our work holds promise for potential TBI treatment and suggests applications for this system to address other crucial CNS injuries.

2.6 REFERENCES

(1) Maas, A. I. R.; Menon, D. K.; Adelson, P. D.; Andelic, N.; Bell, M. J.; Belli, A.; Bragge, P.; Brazinova, A.; Büki, A.; Chesnut, R. M. Traumatic Brain Injury: Integrated Approaches to Improve Prevention, Clinical Care, and Research. *Lancet Neurol.* **2017**, *16* (12), 987–1048.

(2) Maas, A. I. R.; Menon, D. K.; Manley, G. T.; Abrams, M.; Åkerlund, C.; Andelic, N.; Aries, M.; Bashford, T.; Bell, M. J.; Bodien, Y. G. Traumatic Brain Injury: Progress and Challenges in Prevention, Clinical Care, and Research. *Lancet Neurol.* **2022**.

(3) Ng, S. Y.; Lee, A. Y. W. Traumatic Brain Injuries: Pathophysiology and Potential Therapeutic Targets. *Front. Cell. Neurosci.* **2019**, *13*, 528.

(4) Colonna, M.; Butovsky, O. Microglia Function in the Central Nervous System during Health and Neurodegeneration. *Annu. Rev. Immunol.* **2017**, *35*, 441–468.

(5) Adak, A.; Das, G.; Khan, J.; Mukherjee, N.; Gupta, V.; Mallesh, R.; Ghosh, S. Extracellular Matrix (ECM)-Mimicking Neuroprotective Injectable Sulfo-Functionalized Peptide Hydrogel for Repairing Brain Injury. *ACS Biomater. Sci. Eng.* **2020**, *6* (4), 2287–2296.

(6) Xiong, Y.; Mahmood, A.; Chopp, M. Emerging Treatments for Traumatic Brain Injury. *Expert Opin. Emerg. Drugs* **2009**, *14* (1), 67–84.

(7) Chen, S.-J.; Chang, C.-M.; Tsai, S.-K.; Chang, Y.-L.; Chou, S.-J.; Huang, S.-S.; Tai, L.-K.; Chen, Y.-C.; Ku, H.-H.; Li, H.-Y. Functional Improvement of Focal Cerebral Ischemia Injury by Subdural Transplantation of Induced Pluripotent Stem Cells with Fibrin Glue. *Stem Cells Dev.* **2010**, *19* (11), 1757–1767.

(8) Wang, S.; Cheng, H.; Dai, G.; Wang, X.; Hua, R.; Liu, X.; Wang, P.; Chen, G.; Yue, W.; An, Y. Umbilical Cord Mesenchymal Stem Cell Transplantation Significantly Improves Neurological Function in Patients with Sequelae of Traumatic Brain Injury. *Brain Res.* **2013**, *1532*, 76–84.

(9) Giovannelli, L.; Bari, E.; Jommi, C.; Tartara, F.; Armocida, D.; Garbossa, D.; Cofano, F.; Torre, M. L.; Segale, L. Mesenchymal Stem Cell Secretome and Extracellular Vesicles for Neurodegenerative Diseases: Risk-Benefit Profile and next Steps for the Market Access. *Bioact. Mater.* **2023**, *29*, 16–35.

(10) Wennersten, A.; Meijer, X.; Holmin, S.; Wahlberg, L.; Mathiesen, T. Proliferation, Migration, and Differentiation of Human Neural Stem/Progenitor Cells after Transplantation into a Rat Model of Traumatic Brain Injury. *J. Neurosurg.* **2004**, *100* (1), 88–96.

(11) Blanco-Ocampo, D.; Cawen, F. A.; Alamo-Pindado, L. A.; Negro-Demontel, M. L.; Peluffo, H. Safe and Neuroprotective Vectors for Long-Term Traumatic Brain Injury Gene Therapy. *Gene Ther.* **2020**, *27* (1–2), 96–103.

(12) Terstappen, G. C.; Meyer, A. H.; Bell, R. D.; Zhang, W. Strategies for Delivering Therapeutics across the Blood–Brain Barrier. *Nat. Rev. Drug Discov.* **2021**, *20* (5), 362–383.

(13) Lu, Z.; Wang, J.; Qu, L.; Kan, G.; Zhang, T.; Shen, J.; Li, Y.; Yang, J.; Niu, Y.; Xiao, Z. Reactive Mesoporous Silica Nanoparticles Loaded with Limonene for Improving Physical and Mental Health of Mice at Simulated Microgravity Condition. *Bioact. Mater.* **2020**, *5* (4), 1127–1137.

(14) Chen, W.; Tsai, P.-H.; Hung, Y.; Chiou, S.-H.; Mou, C.-Y. Nonviral Cell Labeling and Differentiation Agent for Induced Pluripotent Stem Cells Based on Mesoporous Silica Nanoparticles. *ACS Nano* **2013**, *7* (10), 8423–8440.

(15) Cheng, C.-S.; Liu, T.-P.; Chien, F.-C.; Mou, C.-Y.; Wu, S.-H.; Chen, Y.-P. Codelivery of Plasmid and Curcumin with Mesoporous Silica Nanoparticles for Promoting Neurite Outgrowth. *ACS Appl. Mater. Interfaces* **2019**, *11* (17), 15322–15331.

(16) Lee, H.; Dellatore, S. M.; Miller, W. M.; Messersmith, P. B. Mussel-Inspired Surface Chemistry for Multifunctional Coatings. *Science (80-.).* **2007**, *318* (5849), 426–430.

(17) Wang, Z.; Yang, H.-C.; He, F.; Peng, S.; Li, Y.; Shao, L.; Darling, S. B. Mussel-Inspired Surface Engineering for Water-Remediation Materials. *Matter* **2019**, *1* (1), 115–155.

(18) Cheng, W.; Zeng, X.; Chen, H.; Li, Z.; Zeng, W.; Mei, L.; Zhao, Y. Versatile Polydopamine Platforms: Synthesis and Promising Applications for Surface Modification and Advanced Nanomedicine. *ACS Nano* **2019**, *13* (8), 8537–8565.

(19) Huang, C.; Zhang, L.; Guo, Q.; Zuo, Y.; Wang, N.; Wang, H.; Kong, D.; Zhu, D.; Zhang, L. Robust Nanovaccine Based on Polydopamine-coated Mesoporous Silica Nanoparticles for Effective Photothermal-immunotherapy against Melanoma. *Adv. Funct. Mater.* **2021**, *31* (18), 2010637.

(20) Jouroukhin, Y.; Ostritsky, R.; Assaf, Y.; Pelled, G.; Giladi, E.; Gozes, I. NAP (Davunetide) Modifies Disease Progression in a Mouse Model of Severe Neurodegeneration: Protection against Impairments in Axonal Transport. *Neurobiol. Dis.* **2013**, *56*, 79–94.

(21) Adak, A.; Das, G.; Barman, S.; Mohapatra, S.; Bhunia, D.; Jana, B.; Ghosh, S. Biodegradable Neuro-Compatible Peptide Hydrogel Promotes Neurite Outgrowth, Shows Significant Neuroprotection, and Delivers Anti-Alzheimer Drug. *ACS Appl. Mater. Interfaces* **2017**, *9* (6), 5067–5076.

(22) Luo, Y.; Fan, L.; Liu, C.; Wen, H.; Wang, S.; Guan, P.; Chen, D.; Ning, C.; Zhou, L.; Tan, G. An Injectable, Self-Healing, Electroconductive Extracellular Matrix-Based Hydrogel for Enhancing Tissue Repair after Traumatic Spinal Cord Injury. *Bioact. Mater.* **2022**, *7*, 98–111.

(23) Morihiro, K.; Ankenbruck, N.; Lukasak, B.; Deiters, A. Small Molecule Release and Activation through DNA Computing. *J. Am. Chem. Soc.* **2017**, *139* (39), 13909–13915.

(24) Xie, M.; Fussenegger, M. Designing Cell Function: Assembly of Synthetic Gene Circuits for Cell Biology Applications. *Nat. Rev. Mol. Cell Biol.* **2018**, *19* (8), 507–525.

(25) Saini, K.; Prabhuraj, R. S.; Bandyopadhyaya, R. Development of Mesoporous Silica Nanoparticles of Tunable Pore Diameter for Superior Gemcitabine Drug Delivery in Pancreatic Cancer Cells. *J. Nanosci. Nanotechnol.* **2020**, *20* (5), 3084–3096.

(26) Cheng, J.; Ding, Q.; Wang, J.; Deng, L.; Yang, L.; Tao, L.; Lei, H.; Lu, S. 5-Azacytidine Delivered by Mesoporous Silica Nanoparticles Regulates the Differentiation of P19 Cells into Cardiomyocytes. *Nanoscale* **2016**, *8* (4), 2011–2021. https://doi.org/10.1039/c5nr08560h.

(27) Lei, W.; Sun, C.; Jiang, T.; Gao, Y.; Yang, Y.; Zhao, Q.; Wang, S. Polydopamine-Coated Mesoporous Silica Nanoparticles for Multi-Responsive Drug Delivery and Combined Chemo-Photothermal Therapy. *Mater. Sci. Eng. C* **2019**, *105*, 110103.

(28) Mallesh, R.; khan, J.; Gharai, P. K.; Gupta, V.; Roy, R.; Ghosh, S. Controlling Amyloid Beta Peptide Aggregation and Toxicity by Protease-Stable Ligands. *ACS bio med Chem Au* **2023**, *3* (2), 158–173.

(29) Cheng, W.; Liang, C.; Xu, L.; Liu, G.; Gao, N.; Tao, W.; Luo, L.; Zuo, Y.; Wang, X.; Zhang, X. TPGS-functionalized Polydopamine-modified Mesoporous Silica as Drug Nanocarriers for Enhanced Lung Cancer Chemotherapy against Multidrug Resistance. *Small* **2017**, *13* (29), 1700623.

(30) Ramesh, M.; Balachandra, C.; Andhare, P.; Govindaraju, T. Rationally Designed Molecules Synergistically Modulate Multifaceted Aβ Toxicity, Microglial Activation, and Neuroinflammation. *ACS Chem. Neurosci.* **2022**, *13* (14), 2209–2221.

(31) Gharai, P. K.; Khan, J.; Mallesh, R.; Garg, S.; Saha, A.; Ghosh, S.; Ghosh, S. Vanillin Benzothiazole Derivative Reduces Cellular Reactive Oxygen Species and Detects Amyloid Fibrillar Aggregates in Alzheimer's Disease Brain. *ACS Chem. Neurosci.* **2023**, *14* (4), 773–786.

(32) Schneider, C. A.; Rasband, W. S.; Eliceiri, K. W. NIH Image to ImageJ: 25 Years of Image Analysis. *Nat. Methods* **2012**, *9* (7), 671–675.

(33) Li, J.; Zhang, J.; Chen, Y.; Kawazoe, N.; Chen, G. TEMPO-Conjugated Gold Nanoparticles for Reactive Oxygen Species Scavenging and Regulation of Stem Cell Differentiation. *ACS Appl. Mater. Interfaces* **2017**, *9* (41), 35683–35692.

(34) Roy, R.; Khan, J.; Pradhan, K.; Nayak, P.; Sarkar, A.; Nandi, S.; Ghosh, S.; Ram, H.; Ghosh, S. Short Peptoid Evolved from the Key Hydrophobic Stretch of Amyloid-B42 Peptide Serves as a Potent Therapeutic Lead of Alzheimer's Disease. *ACS Chem. Neurosci.* **2022**, *14* (2), 246–260.

(35) Zhao, X.; Fang, J.; Li, S.; Gaur, U.; Xing, X.; Wang, H.; Zheng, W. Artemisinin Attenuated Hydrogen Peroxide (H2O2)-Induced Oxidative Injury in SH-SY5Y and Hippocampal Neurons via the Activation of AMPK Pathway. *Int. J. Mol. Sci.* **2019**, *20* (11), 2680.

(36) Oliva, C. R.; Moellering, D. R.; Gillespie, G. Y.; Griguer, C. E. Acquisition of Chemoresistance in Gliomas Is Associated with Increased Mitochondrial Coupling and Decreased ROS Production. *PLoS One* **2011**, *6* (9), e24665.

(37) Satoh, T.; Enokido, Y.; Aoshima, H.; Uchiyama, Y.; Hatanaka, H. Changes in Mitochondrial Membrane Potential during Oxidative Stress-induced Apoptosis in PC12 Cells. *J. Neurosci. Res.* **1997**, *50* (3), 413–420.

(38) Gupta, V.; Mahata, T.; Roy, R.; Gharai, P. K.; Jana, A.; Garg, S.; Ghosh, S. Discovery of Imidazole-Based GSK-3 β Inhibitors for Transdifferentiation of Human Mesenchymal Stem Cells to Neurons: A Potential Single-Molecule Neurotherapeutic Foresight. *Front. Mol. Neurosci.* **2022**, *15*, 1002419.

(39) Khan, J.; Das, G.; Gupta, V.; Mohapatra, S.; Ghosh, S.; Ghosh, S. Neurosphere Development from Hippocampal and Cortical Embryonic Mixed Primary Neuron Culture: A Potential Platform for Screening Neurochemical Modulator. *ACS Chem. Neurosci.* **2018**, *9* (11), 2870–2878.

(40) Huang, X.; Ye, Y.; Zhang, J.; Zhang, X.; Ma, H.; Zhang, Y.; Fu, X.; Tang, J.; Jiang, N.; Han, Y. Reactive Oxygen Species Scavenging Functional Hydrogel Delivers Procyanidins for the Treatment of Traumatic Brain Injury in Mice. *ACS Appl. Mater. Interfaces* **2022**, *14* (29), 33756–33767.

(41) Yuan, J.; Li, L.; Yang, Q.; Ran, H.; Wang, J.; Hu, K.; Pu, W.; Huang, J.; Wen, L.; Zhou, L. Targeted Treatment of Ischemic Stroke by Bioactive Nanoparticle-Derived Reactive Oxygen Species Responsive and Inflammation-Resolving Nanotherapies. *ACS Nano* **2021**, *15* (10), 16076–16094.

(42) Mallesh, R.; Khan, J.; Gharai, P. K.; Ghosh, S.; Garg, S.; Arshi, M. U.; Ghosh, S. High-Affinity Fluorescent Probes for the Detection of Soluble and Insoluble Aβ Deposits in Alzheimer's Disease. *ACS Chem. Neurosci.* **2023**, *14* (8), 1459–1473.

(43) Chen, J.-H.; Ou, H.-P.; Lin, C.-Y.; Lin, F.-J.; Wu, C.-R.; Chang, S.-W.; Tsai, C.-W. Carnosic Acid Prevents 6-Hydroxydopamine-Induced Cell Death in SH-SY5Y Cells via Mediation of Glutathione Synthesis. *Chem. Res. Toxicol.* **2012**, *25* (9), 1893–1901.

(44) Slemmer, J. E.; Shacka, J. J.; Sweeney, M. I.; Weber, J. T. Antioxidants and Free Radical Scavengers for the Treatment of Stroke, Traumatic Brain Injury and Aging. *Curr. Med. Chem.* **2008**, *15* (4), 404–414.

(45) Hong, Y.; Yan, W.; Chen, S.; Sun, C.; Zhang, J. The Role of Nrf2 Signaling in the Regulation of Antioxidants and Detoxifying Enzymes after Traumatic Brain Injury in Rats and Mice. *Acta Pharmacol. Sin.* **2010**, *31* (11), 1421–1430.

(46) Martelli, A. M.; Zweyer, M.; Ochs, R. L.; Tazzari, P. L.; Tabellini, G.; Narducci, P.; Bortul, R. Nuclear Apoptotic Changes: An Overview. *J. Cell. Biochem.* **2001**, *82* (4), 634–646.

(47) Kann, O.; Kovács, R. Mitochondria and Neuronal Activity. *Am. J. Physiol. Physiol.* **2007**, *292* (2), C641–C657.

(48) Lifshitz, J.; Sullivan, P. G.; Hovda, D. A.; Wieloch, T.; McIntosh, T. K. Mitochondrial Damage and Dysfunction in Traumatic Brain Injury. *Mitochondrion* **2004**, *4* (5–6), 705–713.

(49) O'Brien, M. A.; Kirby, R. Apoptosis: A Review of Pro-apoptotic and Anti-apoptotic Pathways and Dysregulation in Disease. *J. Vet. Emerg. Crit. care* **2008**, *18* (6), 572–585.

(50) Morales-Garcia, J. A.; Luna-Medina, R.; Alonso-Gil, S.; Sanz-SanCristobal, M.; Palomo, V.; Gil, C.; Santos, A.; Martinez, A.; Perez-Castillo, A. Glycogen Synthase Kinase 3 Inhibition Promotes Adult Hippocampal Neurogenesis in Vitro and in Vivo. *ACS Chem. Neurosci.* **2012**, *3* (11), 963–971.

(51) Park, S. J.; Kim, S.; Kim, S. Y.; Jeon, N. L.; Song, J. M.; Won, C.; Min, D. H. Highly Efficient and Rapid Neural Differentiation of Mouse Embryonic Stem Cells Based on Retinoic Acid Encapsulated Porous Nanoparticle. *ACS Appl. Mater. Interfaces* **2017**, *9* (40), 34634–34640. https://doi.org/10.1021/acsami.7b09760.

(52) Salim, S. Oxidative Stress and the Central Nervous System. *J. Pharmacol. Exp. Ther.* **2017**, *360* (1), 201–205.

(53) Qian, F.; Han, Y.; Han, Z.; Zhang, D.; Zhang, L.; Zhao, G.; Li, S.; Jin, G.; Yu, R.; Liu, H. In Situ Implantable, Post-Trauma Microenvironment-Responsive, ROS Depletion Hydrogels for the Treatment of Traumatic Brain Injury. *Biomaterials* **2021**, *270*, 120675.

(54) Fischer, A. H.; Jacobson, K. A.; Rose, J.; Zeller, R. Hematoxylin and Eosin Staining of Tissue and Cell Sections. *Cold spring Harb. Protoc.* **2008**, *2008* (5), pdb-prot4986.

(55) Sulhan, S.; Lyon, K. A.; Shapiro, L. A.; Huang, J. H. Neuroinflammation and Blood–Brain Barrier Disruption Following Traumatic Brain Injury: Pathophysiology and Potential Therapeutic Targets. *J. Neurosci. Res.* **2020**, *98* (1), 19–28.

(56) Mu, X.; Wang, J.; Li, Y.; Xu, F.; Long, W.; Ouyang, L.; Liu, H.; Jing, Y.; Wang, J.; Dai, H. Redox Trimetallic Nanozyme with Neutral Environment Preference for Brain Injury. *ACS Nano* **2019**, *13* (2), 1870–1884.

(57) Chen, L.; Song, Q.; Chen, Y.; Meng, S.; Zheng, M.; Huang, J.; Zhang, Q.; Jiang, J.; Feng, J.; Chen, H. Tailored Reconstituted Lipoprotein for Site-Specific and Mitochondria-Targeted Cyclosporine a Delivery to Treat Traumatic Brain Injury. *ACS Nano* **2020**, *14* (6), 6636–6648.

(58) Binley, K. E.; Ng, W. S.; Tribble, J. R.; Song, B.; Morgan, J. E. Sholl Analysis: A Quantitative Comparison of Semi-Automated Methods. *J. Neurosci. Methods* **2014**, *225*, 65–70.

(59) Klein, M.; Lohr, C.; Droste, D. Age-Dependent Heterogeneity of Murine Olfactory Bulb Astrocytes. *Front. Aging Neurosci.* **2020**, *12*, 172.